MAGNETIC IMAGING OF TOPOLOGICAL ANTIFERROMAGNETS

by

PAUL SASS

A dissertation submitted to the

School of Graduate Studies

Rutgers, The State University of New Jersey

in partial fulfillment of the requirements

for the degree of

Doctor of Philosophy

Graduate Program in Physics and Astronomy

written under the direction of

Weida Wu

and approved by

_____

_____

_____

_____

_____

New Brunswick, New Jersey

October, 2020

ABSTRACT OF THE DISSERTATION

Magnetic Imaging of Topological Antiferromagnets

by PAUL SASS

Dissertation Director:

Weida Wu

Antiferromagnetic order in topological materials has recently become incredibly important in the quest for exotic phenomena such as high temperature quantum anomalous Hall effect, quantized magnetoelectric effect, chiral edge modes, and Weyl and Dirac semimetal states. However, there is a lack of understanding of the antiferromagnetic domains and domain walls in these materials. The control of these domain walls or spin textures is not only important for controlling these states, but also crucial for spintronic applications of antiferromagnets. Despite many efforts, it has been challenging to directly visualize antiferromagnetic domains or domain walls with nanoscale resolution, especially in magnetic field.

In this thesis, we show magnetic imaging of domain walls in several uniaxial antiferromagnets including the topological insulator $MnBi_2Te_4$ family and the Dirac semimetal $EuMnBi_2$, using cryogenic magnetic force microscopy (MFM). Our MFM results reveal higher magnetic susceptibility inside the domain walls than in domains. Domain walls in these antiferromagnets form randomly with strong thermal and magnetic field dependence.

Through this application, we also present microscopic evidence of the persistence of uniaxial A-type antiferromagnetic order to the surface layers of $MnBi_2Te_4$ single crystals using magnetic force microscopy. Our results reveal termination-dependent magnetic contrast across both surface step edges and domain walls, which can be screened by thin layers of soft magnetism. The robust surface A-type order is further corroborated by the observation of termination-dependent surface spin-flop transitions, which have been theoretically proposed decades ago and not observed in natural antiferromagnets until now.

The direct visualization of these domain walls and domain structures in magnetic field not only provides key ingredients for understanding the electronic properties of the antiferromagnetic topological insulator $MnBi_2Te_4$, but also opens both a new way of exploring intrinsic surface metamagnetic transitions in natural antiferromagnets and a new path toward control and manipulation of domain walls or spin textures in functional antiferromagnets.

Acknowledgments

I would first like to extend my deepest gratitude to my advisor, mentor and hero, Prof. Weida Wu. I have never known anyone before with more integrity than him. He has unwavering patience and support for his students and was always there for me no matter the time or his workload. He not only taught me to respect physics and nature, but to respect myself. To never give up or get discouraged, to be proud of my work, to try new approaches, to push the boundaries despite what the literature claims. These are things that will stick with me for the rest of my life.

I would also like to thank all of our collaborators for their incredible effort. The high quality crystals were provided and characterized by Jiaqiang Yan, Dimuthu Obeysekera and Junjie Yang. Jinwoong Kim and Prof. David Vanderbilt helped connect the experimental data to the theory with model simulations. Our MFM tips were coated and calibrated using equipment from Prof. Sang-Wook Cheong's and Prof. Seongshik Oh's lab with helpful guidance from Kai Du. I would also like to thank the Rutgers NSF DMREF team for the invaluable discussions. I would also like to thank the staff at Rutgers for helping with the lab and my graduate student life. Jerrell Spotwood for help keeping the lab stocked. The custodial staff for keeping the lab clean. Shirley Hinds for helping me keep my status as a student. Denise Rafferty and Valerie Cardinale for their endless patience helping me with my March Meeting reimbursements. The machine shop, Bill Schneider, Paul Pickard, Marc Lesko and Eric Paduch for their everlasting patience machine titanium parts for us. And Misha Kareev for helping us keep our microscopes filled with liquid Helium.

I would also like to acknowledge my group mates for their help and support. Wenbo Ge and Wenbo Wang who helped take MFM measurments. Wenhan Zhang, Yanan Geng,

Chen Chen, Zengle Huang, Ying-ting Chan, Jixia Dai, Ying Liu, Ying Sun, Liqin Yan, Shijie Fang, Maggie Xiao, Fernando Garcia, Daram Ramdin, George Ju, Grace Cai, James Chi, Alon Flor, Joy Sodon, Allison Hosler, Daniel Shulman and Ingrid Zimmermann for all of their help in the lab, discussions and support.

Finally, I would like to sincerely thank my friends and family for their love and support through the last six years. I certainly would not have been able to do it without them. Especially my parents, my sister, my wife and our dogs Yeti and Luna. Nothing gave me more joy than to go home and show my wife all the cool things I scanned that day. I am so happy my parents, grandparents, aunts and uncles all nurtured my love for nature and learning from a young age.

Dedication

To my dear wife,

our dogs,

and to my family,

for their endless love and support.

Table of Contents

List of Tables

List of Figures

Chapter 1

Background and Motivation

The universe is full of microscopic particles, zipping around according to their own set of laws. However, mix them together in the right way and nature will allow you to observe much more exotic *emergent* states of matter, such as, crystals, magnets, and superconductors. These states of matter can be classified by the specific symmetries with which they break: translational, reflection, rotational, time reversal or gauge symmetry, and can be topologically protected by these symmetries. Meaning that they are protected from adiabatic changes in trivial material parameters, like defects and shape.

Discovered in the early 80's, the quantum Hall effect (QHE) was the first observed topological phase of matter. Over the next 35 years, new exotic states evolved from the QHE, the quantum spin Hall and quantum anomalous Hall states. These systems feature similar topologically protected chiral/helical edge currents which are quantized and dissipationless, but require no external magnetic field. The applications of the quantum anomalous Hall effect (where only one chiral edge spin state is preferred) range from electronics with extremely low power consumption to metrology.

Recently, the quantum anomalous Hall effect (QAHE) has been observed and studied in Cr- and V-doped $(Bi,Sb)_2Te_3$, to high precision. However, extremely low temperature is required to observe this exotic effect due to complications from magnetic doping. Thus, antiferromagnetic topological insulators (AFMTI) were born, giving rise to similar exotic effects like QAHE and topological magnetoelectric effect, but requiring no magnetic doping. However, the magnetic domain states and exact magnetic configurations on the surfaces of

these AFM TIs is still unknown. Additionally, due to the nature of AFMs, there are few experimental techniques that have the sensitivity and resolution to probe their magnetic states. Through our cryogenic magnetic force microscopy technique however, we are able to image the domains and domain walls in uniaxial AFMs, giving us a glimpse into the magnetic secrets these AFM TIs hold.

First, the classical and quantum Hall effects will be introduced, followed by their impact on the field of topology in condensed matter physics and later, the discovery of TIs, topological semimetals, and finally, AFM TIs will be discussed.

1.1 The Classical Hall Effects

1.1.1 Hall Effect

When a conductor is subjected to a longitudinal current and perpendicular DC magnetic field, the charge carrying electrons are deflected to one side of the conductor, setting up a transverse potential difference across the conductor, as shown in Fig. 1.1.

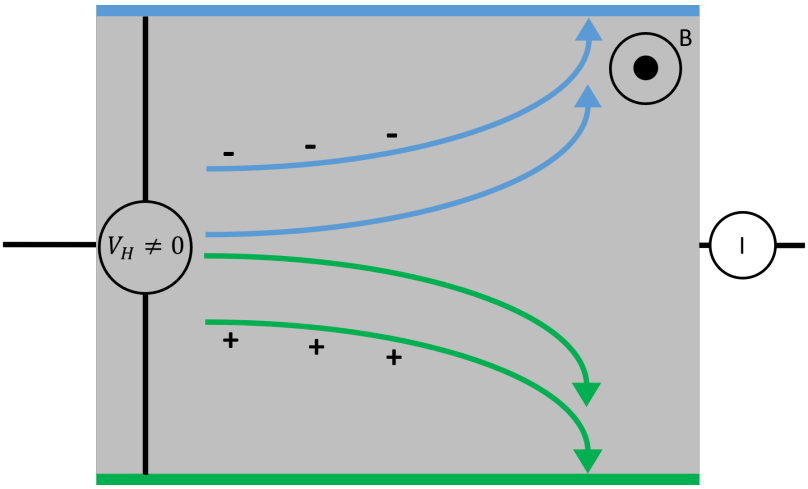

Figure 1.1: Depiction of the classical Hall effect. External magnetic field perpendicular to non-magnetic conductor deflects electrons (blue) to one side or to the other side if the carriers are holes (green). Equillibrium is met when there is a strong enough electric field to balance out the Lorentz force. This leads to a non-zero Hall voltage.

The transverse resistance, coined the Hall resistance, is this transverse potential difference divided by the applied current. It is proportional to the applied magnetic field divided by the carrier density multiplied by the carrier charge. This is the Hall effect, discovered by 24 year old American Edwin Hall (Fig. 1.2(a)) and his advisor Augustus Rowland (Fig. 1.2(b)) in 1879 at Johns Hopkins University.

Hall's inspiration came from Maxwell's book. It had said that electromagnetic forces act on the conductor and not on currents, thus if the conductor is held fixed, there would be no effect on the conductor[1]. Hall and Rowland believed the opposite and for various reasons, adopted the reasoning, "If the current of electricity in a fixed conductor is itself attracted by a magnet, the current should be drawn to one side of the wire, and therefore the resistance experienced should be increased"[2]. Unfortunately Maxwell had died a couple of months after Hall's publication. The editor of the second edition of Maxwell's book later in 1881 noted Hall's discovery.

Hall and Rowland's first experiment involved hooking up a silver triangular wire wound into a spiral, oriented perpendicular to magnetic poles, to a wheatstone bridge and galvanometer (could measure down to 1 $\mu\Omega$) and passed 0.3 T through the spiral. He observed nothing consistent and attributed resistance changes to stress effects[2].

Their next experiment involved passing current radially through a gold disk to observe an increase in resistance, due to the current becoming less radial and more spiral like. Nothing was observed however, and he attributed it to the fact that the conductor was too thick.

To test this idea they put gold leaf on glass, which would have a higher current density than the metal bar that they previously tried, and ran current through it with a galvanometer perpendicular to the current direction to test for a voltage difference. The needle deflected (not by magnetic induction) and was reversed when the magnetic field reversed and did not reverse when the meter was moved over the bar. More systematic experimentation

revealed that this voltage was proportional to the magnetic flux density times the applied current.

They also wanted to see if the width of the conductor had any affect and found that the flux density times the current density and width divided by the hall voltage was constant, which was later found to be the carrier density times the electron charge, giving new insight into the nature of metals and their interaction with electromagnetic fields.

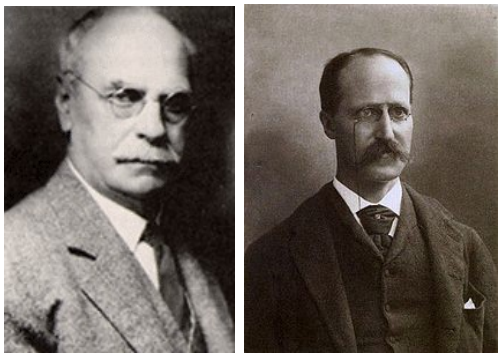

Figure 1.2: Edwin Hall (left) and his advisor Augustus Rowland responsible for the discovery of the Hall effect.

These findings contributed greatly to understanding electrical properties of metals. The Hall resistance gives information about the sign of charge carriers, carrier density, mobility, doping, and number of valence electrons per atom. The Hall effect is used today in magnetometers and sensors such as: speed sensors, ignition systems, smart phones, gps, and even thrusters. It is one of the greatest discoveries in solid state physics, lighting the way to the more exotic phenomena in quantum transport, such as its quantum successor, the quantum Hall effect. Before the quantum effect however, Hall made a surprising discovery that linked the Hall effect to intrinsic magnetism.

1.1.2 Anomalous Hall Effect

One year after the Hall effect, Hall discovered that the effect was ten times larger in ferromagnetic conductors like iron[3]. This was coined the anomalous Hall effect (AHE) or

extraordinary Hall effect as it used to be known and is depicted in Fig. 1.3.

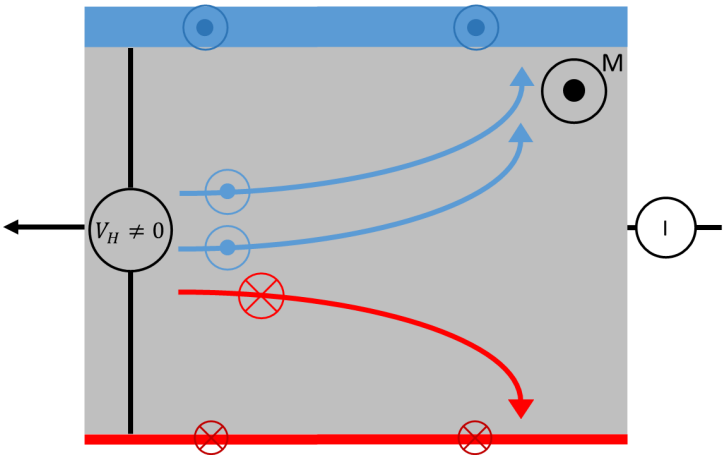

Figure 1.3: Anomalous Hall effect in ferromagnetic material. Blue spin-up electrons are deflected upward and red spin-down electrons are deflected downward. There is an asymmetry in the accumulation of electrons and spin due to the combined effect of spin splitting from SOC and majority-minority asymmetry from the magnetization coupling and thus a non-zero Hall voltage is set up.

Early experiments showed that the transverse resistivity (Hall resistivity) behaves differently in an applied field in ferromagnetic conductors than non-magnetic conductors. Non-magnetic conductors have a linear relation between Hall resistance and applied magnetic field, as depicted in Fig. 1.4(a). In magnetic conductors, a steep increase in the Hall resistivity is seen when the external field is weak, it then hits a saturation after the applied field is strong enough and continues linearly, as shown in Fig. 1.4(b).

Experimentation on Fe, Co, and Ni by Kundt in 1893 showed that this saturation value is roughly proportional to the magnetization[5]. Years later arguments set forth by Pugh and Lippert established that $\rho_{xy} = R_0\mu_o H_z + R_s\mu_o M_z$, where R_0 is the classical Hall coefficient, $\mu_0 H_z$ is the external magnetic field, R_s is a constant that depends on the material, which can be positive or negative, and M_z is the magnetization in the z direction[6]. Extrapolation of a ρ_{xy} vs. H_z curve shows that the saturation value is the magnetization, as shown in Fig. 1.4(b). Continuing to sweep the magnetic field shows similar behavior to a hysteresis loop in ferromagnetic materials, as shown in Fig. 1.4(c).

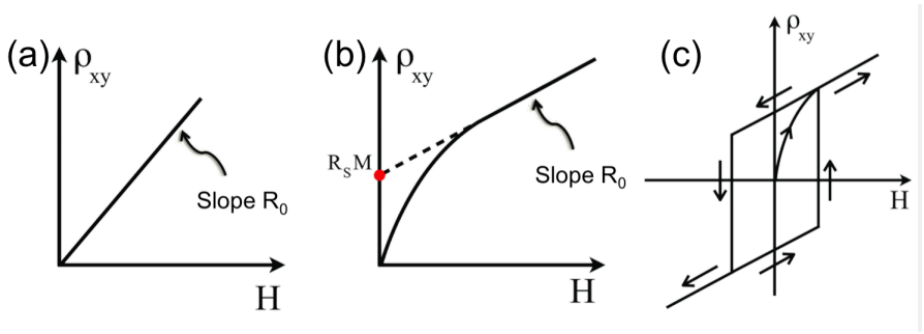

Figure 1.4: Typical behaviors of the Hall and anomalous Hall effects. The Hall resistivity ρ_{xy} is plotted versus external magnetic field H. (a) The Hall effect; (b) The anomalous Hall effect; and (c) The hysteresis loop measured from the anomalous Hall effect. Adapted from ref. [4].

Owing the asymmetry in spin accumulation to the difference in minority and majority spins from the magnetization, the origin of the AHE remained mysterious until 1954 when Karplus and Luttinger put forward a crucial theory that the R_s coefficient could be explained by spin-orbit coupling (SOC) of the electrons. They showed that when an external electric field, perpendicular to the magnetization, is applied to the solid, in this case Fe or Ni, the electrons acquired an additional, anomalous, velocity. This implies that there will be a current perpendicular to the electric field and to the net spin of the electrons. The current will be proportional to the magnetization and its coefficient will yield R_s[7]. They predicted that since the anomalous velocity depends on the band structure, the coefficient should not have any scattering, which agreed with previous experiments on Fe and Ni. This makes sense since the overall contribution of the anomalous velocity to the conductivity will then be the transverse σ_{xy}, which inverting this tensor yields $\rho_{xy} \approx \sigma_{xy}/\sigma_{xx}^2 \propto \rho^2$. As you will see later, the connection between the AHE and SOC will propel the Hall effect into its more exotic, quantum forms.

1.1.3 Spin Hall Effect

When thinking about the AHE, researchers naturally asked the question whether there could still be a Hall effect with no net magnetization or external magnetic field. The answer was a resounding yes, yet with subtle differences to the AHE. In the AHE, since there is an inherent magnetization, there is a carrier spin polarization. In the spin Hall effect (SHE), the material has no net magnetization, but still has inherent SOC. Therefore, there will still be spin accumulation in both directions, but there will be no asymmetry in the accumulation of charges, because there is no magnetization to break the symmetry between the spin up and spin down states and thus, no Hall voltage to measure, as depicted in Fig. 1.5.

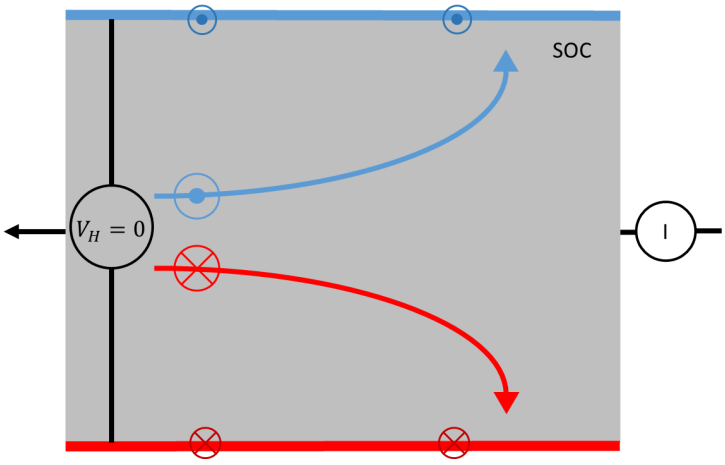

Figure 1.5: Depiction of spin Hall effect, where equal amount of blue spin-up electrons are deflected upward as red spin-down electrons are deflected downward due to spin orbit coupling. No Hall voltage is set up, but there is a spin polarization across the material.

Despite having no measurable Hall voltage, experimentalists have managed to observe the SHE using optical detection techniques. In 2004, Kato et al. spatially imaged the SHE for the first time in AlGaAs quantum wells using magneto-optical Kerr-rotation spectroscopy[8]. They observed opposite spin accumulations in the 2-D electron gas (2DEG),

as shown in Fig. 1.6. The next question is what happens when one applies a strong magnetic field to an electron system with reduced dimensionality. For that, let us go back in time a bit.

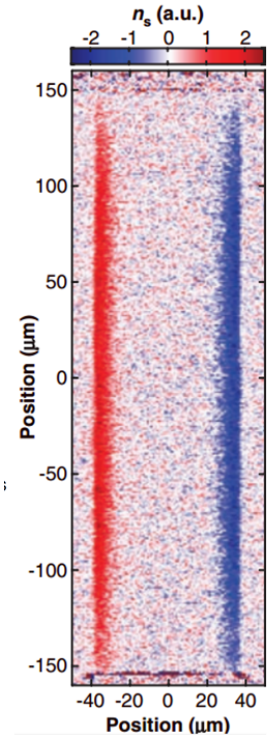

Figure 1.6: 2-D spatial profile of the spin accumulation near the edges of a AlGaAs/GaAs quantum well mapped out by static Kerr rotation. Two spin Hall peaks can be seen at each edge, the right is spin-down and the left is spin-up. Adapted from ref. [8].

1.2 A Quantum Leap to the Quantum Hall Effects

1.2.1 Quantum Hall Effect

In the early 1930s, much interest was generated in probing phenomena in the quantum regime of electron transport. There are many experiments which observe oscillations of different quantities with a changing applied magnetic field. The first, however, were the Shubnikov-de Haas[9] and de Haas-van Alphen[10] effects observed in 1930. Both effects were discovered in Bi at low temperatures and intense magnetic fields. The former observed

conductivity oscillate with increasing applied magnetic field, the latter, magnetic moment.

To explain these phenomena, Landau's work on the quantization of electron orbits in magnetic fields provided the first theoretical key[11]. Additionally, as a consequence, this understanding lead to the extraction of the shapes of the Fermi surfaces of these metals using these quantum oscillations[12].

With technological developments in solid state physics quickly emerging, especially after the transistor in 1947, semiconductors began to spark fundamental physical interest from their industrial application due to their reduced dimensionality and lack of defects. Making them the perfect platform to study quantum oscillations. A major stepping stone on the way to revealing the quantum Hall effect was an experiment in 1966 where Shubnikov-de Haas oscillations were observed in a Si metal-oxide-semiconductor field-effect transistor[13].

A little over a century after Hall's discovery, in 1980 at the Grenoble High Magnetic Field Laboratory, a discovery was made that would change condensed matter history. Klaus von Klitzing (later awarded the Nobel Prize for this discovery in 1985), Pepper, and Dorda found that when the charge carriers are confined to a 2D sheet, in this case the same Si transistor as above, the Hall resistance becomes quantized to $h/\nu e^2$ at specific values of applied magnetic field, where h is Planck's constant, e is the electron charge, and ν is an integer[14]. The magnetic field and temperature here however needs to be high and low enough, respectively, that the Landau level energies overcome the thermal energy.

What they saw in this experiment, was a not a smooth linear increase in the Hall resistance, but rather showed a series of plateaus, as depicted in Fig. 1.7. The longitudinal resistance was seen going to zero when the transverse resistance was plateaued, and peaked between the plateaus. It is understood that at these plateaus, the number of electrons is an integer multiple of the number of available eigenstates, this is the filling factor ν above. The places where the Hall resistivity is quantized, edge channels appear at the edges of the 2DEG, as shown in Fig. 1.8. This can be visualized classically as an electron skipping

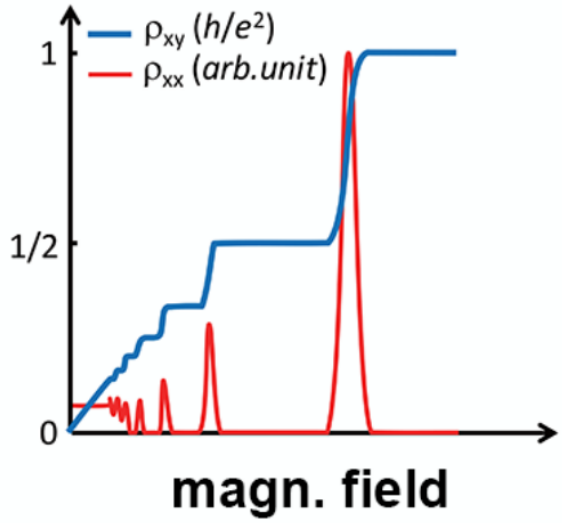

Figure 1.7: The quantum Hall effect occurs in a two-dimensional electron system under a large applied magnetic field. The transverse resistance ρ_{xy} takes on quantized values while the longitudinal resistance ρ_{xx} vanishes. Adapted from ref. [15].

orbits on the edges, however in realistic systems, this can be thought of as the bending of the landau levels due to the confining potential at the edge, and edge states appear where the levels cross the Fermi energy.

What is amazing is that this effect is immune to sample imperfections, field inhomogeneities, electron density differences and so on. Later on it was found that the Hall conductance was a topological invariant, and it is topology that gives such immunity. This topological protection is the reason for the high precision of the Hall resistance (10^{-10}) and it has been used as an industry standard since 1990, it is equal to $h/e^2 = 25812.807557(18)\Omega$, also known as the von Klitzing constant. The edge channels are also immune to scattering, since there are no other states for the electrons to scatter into, and thus are dissipationless. This has immense applicability to electronic devices that need to reduce heat dissipation. However, in the QHE, a high magnetic field on the order of 10 T needs to be applied to see these effects, so the question that is natural to ask is can one get a quantized version of the SHE, i.e. quantization with no external field? Before we arrive there, let us see why these

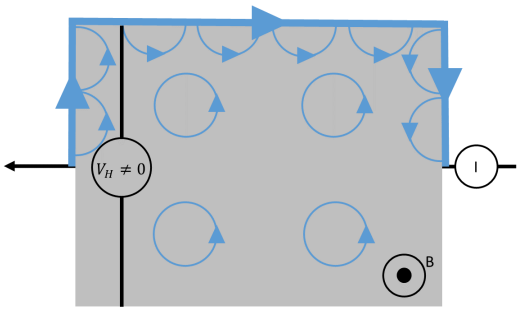

Figure 1.8: A two-dimensional electron gas in a strong perpendicular external magnetic field sends the electrons into cyclotron orbits and quantizes their energies into Landau levels. The topologically protected edge current can only propagate one way and can be thought of classically as the skipping orbits of the electrons, where ,quantum mechanically, is from the bent bands at the confining potential crossing the fermi level.

states are topologically protected and why the resistance comes in integer multiples.

1.2.2 Topological Protection: TKNN Invariant and Berry Curvature

To explain why the quantum Hall effect is so robust against any changes in shape or impurities in the material, Laughlin first proposed a topological argument based on gauge invariance[16]. Later on, Thouless, Kohmoto, Nightingale and den Nijs (TKNN) related the Hall conductance to a topological invariant in momentum space[17]. The topological invariant was then used to rewrite the Hall conductance in terms of the bulk states.

For an electron zipping through a periodic potential, like in a crystal or metal, its eigenfunctions can be written as the product of a plane wave and a periodic Bloch function, $u_{\mathbf{k}n}(r)$, which has the same periodicity as the potential. The eigenfunctions expressed as $\psi_{\mathbf{k}n}(r) = e^{i\mathbf{k}\cdot r}u_{\mathbf{k}n}(r)$, where n is the band index and $\mathbf{k}$ is the wave vector, satisfy the Schrodinger equation $H_{\mathbf{k}}(\mathbf{r})u_{\mathbf{k}n}(\mathbf{r}) = E_{\mathbf{k}n}u_{\mathbf{k}n}(\mathbf{r})$, where $H_{\mathbf{k}}(\mathbf{r}) = e^{-i\mathbf{k}\cdot r}H(\mathbf{r})e^{i\mathbf{k}\cdot r}$. Using the Kubo formula, the Hall conductivity of a 2DEG can be written in terms of the Bloch wave functions, shown by TKNN,

$$\nu = \frac{i}{2\pi}\sum \oint_{BZ} d^2\mathbf{k}\left(\frac{\partial u^*}{\partial \mathbf{k}_x}\frac{\partial u}{\partial \mathbf{k}_y} - \frac{\partial u^*}{\partial \mathbf{k}_y}\frac{\partial u}{\partial \mathbf{k}_x}\right) = \frac{h}{e^2}\sigma_{xy}, \tag{1.1}$$

where the sum is over the occupied electron bands and the integral is over the Brillouin zone, which is topologically equivalent to a torus. The above integral was shown to always be an integer by the Chern-Simons theorem.

Here, the integral is always an integer, so ν only depends on the Bloch wave functions. As long as there are no partially filled bands, ν will always be an integer[18]. To derive the TKNN invariant of the quantum Hall state one can apply the concept of Berry phase[19] to the Bloch bands. The Berry connection, Berry phase and Berry curvature written in terms of the Bloch functions can be defined as

$$\mathbf{A}_n(\mathbf{k}) = i \langle u_{n\mathbf{k}} \mid \nabla_{\mathbf{k}} \mid u_{n\mathbf{k}} \rangle \tag{1.2}$$

$$\phi_n = \oint_{BZ} \mathbf{A}_n(\mathbf{k}) \cdot d\mathbf{k} \tag{1.3}$$

$$\mathbf{\Omega}_n(\mathbf{k}) = \nabla \times \mathbf{A}_n(\mathbf{k}) \tag{1.4}$$

which can be thought to behave as a vector potential, Ahraronov-Bohm phase and effective magnetic field in momentum space, respectively. The Berry phase is gauge invariant over the loop in Eq. 1.1. Non-zero Berry curvature depends on the symmetries of the system. Two important symmetries are space-inversion (IS) and time-reversal symmetry (TRS), defined respectively,

$$\mathbf{\Omega}_n(\mathbf{k}) = \mathbf{\Omega}_n(\text{-}\mathbf{k}) \tag{1.5}$$

$$\mathbf{\Omega}_n(\mathbf{k}) = -\mathbf{\Omega}_n(\text{-}\mathbf{k}) \tag{1.6}$$

Only when one symmetry is broken, a non-zero Berry curvature arises. Equation 1.1 can be rewritten with the Berry curvature as

$$C = \frac{1}{2\pi} \int_{BZ} \mathbf{\Omega}_n d^2\mathbf{k} = 0, \pm 1, \pm 2, ... \tag{1.7}$$

The integral is a multiple of 2π when the Berry connection is singular and zero otherwise. A non-zero number indicates the existence chiral edge states in the system. This is the TKNN invariant[17] or the first Chern number[20] or $\mathbb{Z}$ invariance. Thus, the Hall conductance

is a measure of the integral of Berry curvature in momentum space and is topologically protected.

1.2.3 Quantum Spin Hall Effect

A large motivation for the study of the quantum spin Hall effect (QSHE) is the application to spintronic devices (devices in which spin carries information, not charge) and the study of topologically nontrivial states of matter. They are expected to be capable of, combining information processing with storage with faster speeds and higher densities, having extremely low power dissipation and be able to perform reversible quantum computations[21]. The QSHE is great for this because the effect allows for direct electric manipulation of spin without a magnetic field, and the resulting spin current can flow without dissipation. In addition to device application, the QSHE is of fundamental interest because it is another topologically nontrivial state of matter aside from the QHE (where Hall conductance is quantized and topologically protected).

To study this topological state a few interesting materials were proposed to exhibit the QSHE such as, doped semiconductors, graphene, and strained semiconductors[22, 23]. A quite interesting material proposal, and relevant to this review, was made explaining that QSHE could be seen in specific types of band insulators such as zero-gap and narrow-gap semiconductors, now coined topological insulators (TI)[24].

TIs are insulators that are insulating in their bulk, but are conducting on their surface. These metallic surface states are helical and obey a Dirac-type linear energy-momentum dispersion relation that is protected by TRS[25]. Upon a time-reversal operation the electron wave vector k and the spin will flip sign. The helical surface states of a TI are invariant under such operation since the opposite spin channels are locked to the opposite momenta. The QSH insulator state is invariant under time reversal and has a charge excitation gap in the 2D bulk, but has topologically protected gapless edge states that lie inside the bulk insulating gap as depicted in Fig. 1.9(b). Since both TRS and IS are preserved, the invariant

is rewritten as,

$$\mathbb{Z}_2 = \frac{1}{2\pi}\left(\oint_{Half\ BZ} \mathbf{A}_n(\mathbf{k}) \cdot d\mathbf{k} - \int_{Half\ BZ} \mathbf{\Omega}_n d^2\mathbf{k}\right) = 0\ or\ 1(mod\ 2) \tag{1.8}$$

called the $\mathbb{Z}_2$ invariant[26].

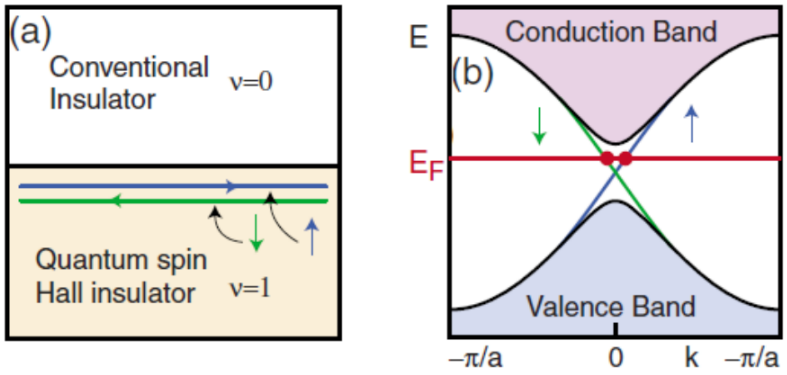

Figure 1.9: Edge states in the quantum spin Hall insulator (QSHI). (a) The interface between a QSHI and an ordinary insulator. (b) The edge state dispersion in the graphene model in which up and down spins propagate in opposite directions. Adapted from ref. [27].

A sufficient condition for these edge states is band inversion. Spin-orbit coupling lifts the degeneracy of the spin states, splitting the conducting symmetric bonding and valence asymmetric antibonding states, allowing a portion of the conduction band to become anti-symmetric and part of the valence band symmetric, such that at the interface, the bands must be continuous and thus, edge states appear, as shown in Fig. 1.9(b). At the boundary, the bands cross and the Fermi energy intersects the bands if it is in the SOC opened gap. This crossing contributes to backscattering-immune conducting edge states which have opposite spin-polarization and counter-propagate at the edges, as shown in Fig. 1.9(a) and Fig. 1.10.

While the initial proposal of the QSH state in graphene[22] provided an interesting theoretical toy model, it was soon shown to be unrealistic since the spin-orbit gap in this system is extremely small, i.e. QSHE occurring below ∼10 mK[28]. In 2006, Bernevig, Hughes and Zhang[29] initiated the search for the QSH state in semiconductors with an "inverted"

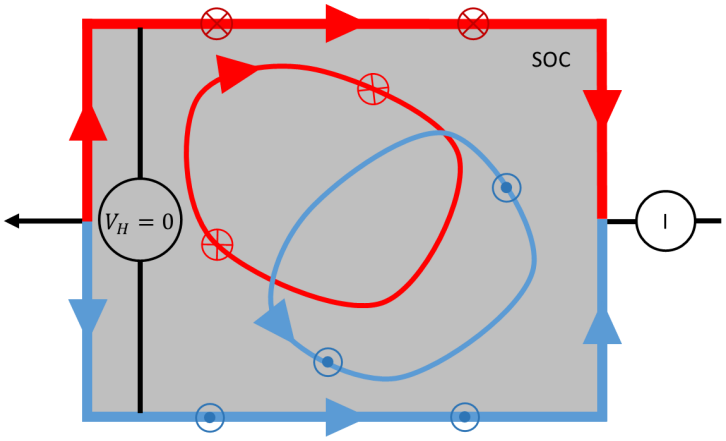

Figure 1.10: Quantum spin Hall effect showing equal, but counter propagating blue spin-up and red spin-down edge currents due to SOC. The current loops in the center do not contribute to the edge currents. Since there is nothing to break the symmetry between the spins there is no Hall voltage set up, but there is a spin polarization across the material.

electronic gap, and predicted a quantum phase transition in HgTe/CdTe quantum wells (QW) as a function of the thickness of the QW. The QW system should be a QSH insulator when the thickness of the HgTe layer is thicker than a certain critical value and show a single pair of helical edge states.

In 2007, experimental observation by Markus Koenig et al., revealed in HgTe/CdTe QWs at 30 mK the presence of these edge channels with no applied magnetic field[30]. They found that these edge channels appeared in the QWs with thickness greater than 6.5 nm, as shown in Fig. 1.11(a). Figure 1.11b shows the energy spectra for each thickness regime, with the edge states shown in red and blue. Since there was no external magnetic field to bias the charge carrier flow, no transverse voltage appeared. Instead they measured the longitudinal conductance and saw that above the critical thickness the conductance was quantized to $2e^2/h$ ($\nu = 2$), as shown in Fig. 1.11(c), indicating the formation of two edge channels comprised of oppositely flowing currents, one with spin up and one with spin down electrons, imposed by strong SOC in the HgTe layer.

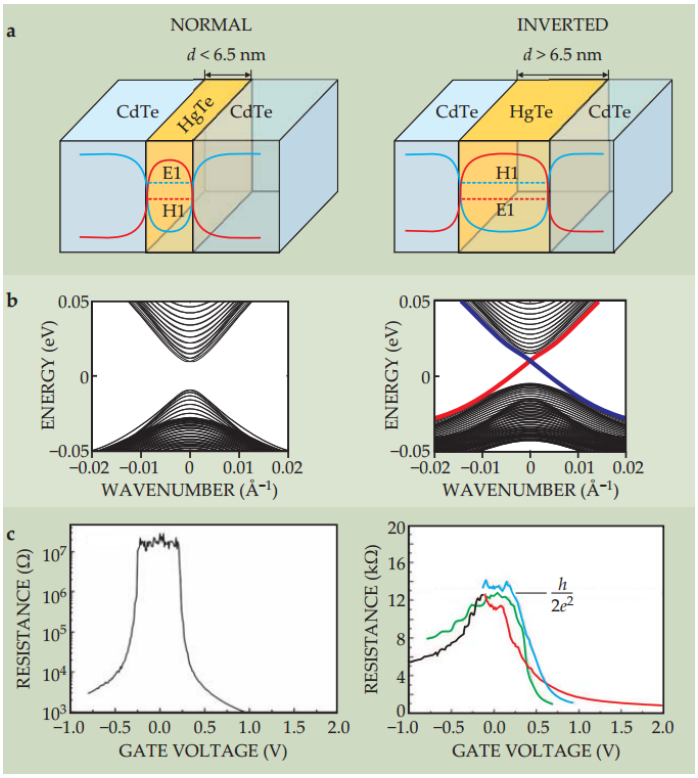

Figure 1.11: HgTe QW 2D TIs. (a) Potential energy of electrons in conduction band (blue) and holes in valence band (red). For thickness d_c ~6.5 nm, the lowest energy conduction subband E1, is higher than the highest valence band, H1. For d > d_c, those electron and hole bands are inverted. (b) Surface states appear above the critical thickness (red and blue lines) (c) Experimentally measured resistance of thin and thick QWs, plotted against the gate voltage. The thin QW has a nearly infinite resistance within the gap, whereas the thick QW has a quantized resistance plateau at R = $h/2e^2$ ($\nu = 2$), due to the perfectly conducting edge states. Red and blue are much much thicker QWs, proof that only the edges are conducting. Adapted from ref. [30].

The edge states in the HgTe/CdTe interface are 1D even though the TI is 2D, as illustrated in Fig. 1.12(a), where their dispersion is similar to that of massless relativistic fermions. Generalizing this to a 3D TI gives 2D edge states, as shown in Fig. 1.12(b), with dispersion similar to a Dirac cone, as illustrated in Fig. 1.13(b).

$Bi_{1-x}Sb_x$ alloy was predicted by Liang Fu and Kane to be a 3D TI[32]. Later investigation by Zahid Hasan, using angle-resolved photoemission spectroscopy (ARPES), using photons to eject electrons and measuring the ejected angle and energy to get information

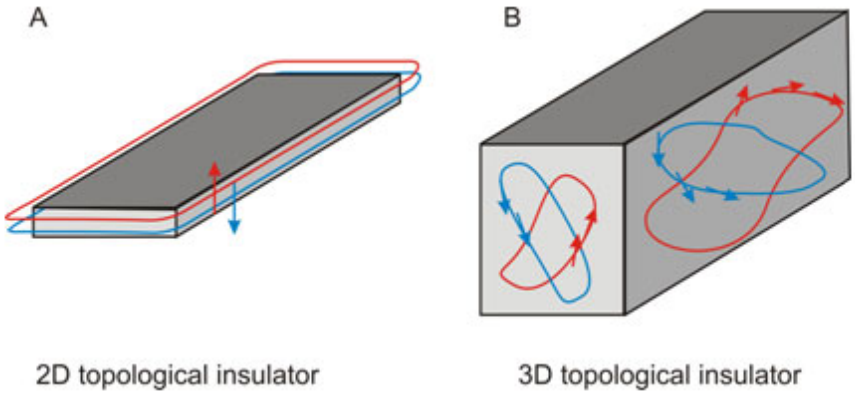

Figure 1.12: (A) Schematic of the 1D edge states in a 2D TI. The red and blue curves represent the edge current with opposite spin character. (B) Schematic of the 2D surface states in a 3D TI. Adapted from ref. [31].

about the material's dispersion relation, confirmed the existence of edge states[33]. However, the surface band structure of this material turned out to be too complex and difficult to control.

Soon after in 2009, Zhang et al.[35] predicted that Bi_2Te_3, Bi_2Se_3 and Sb_2Te_3, with structures like that shown in Fig. 1.13(a), are 3D TIs which were shortly confirmed experimentally. A single Dirac-cone surface state, for the first time, in Bi_2Se_3 was observed by Xia et al.[36] and later for Bi_2Te_3 by Hsieh et al.[37] and Chen et al.[34] independently. Different from the HgTe QWs, the Bi_2Te_3 surface states lie at the interface between the inverted bulk bands and the surrounding non-inverted insulating "vacuum" bands, so the band crossing occurs because of the mismatch of reversed bands between the sample surface and the vacuum. Similar to the QWs, the band inversion is driven by strong SOC in the Bi_2Te_3. First principle calculation showed a Dirac cone at the surface, with electron spin lying in the plane of the surface and perpendicular to the momentum, as shown in Fig. 1.13(b). The ARPES measurements by Zhi-xun Shen's group confirmed this, as shown in Fig. 1.13(c), the Dirac cone is seen meeting at the bulk valence band.

It is natural to ask if there is a way now to break the symmetry of the QSHE in these

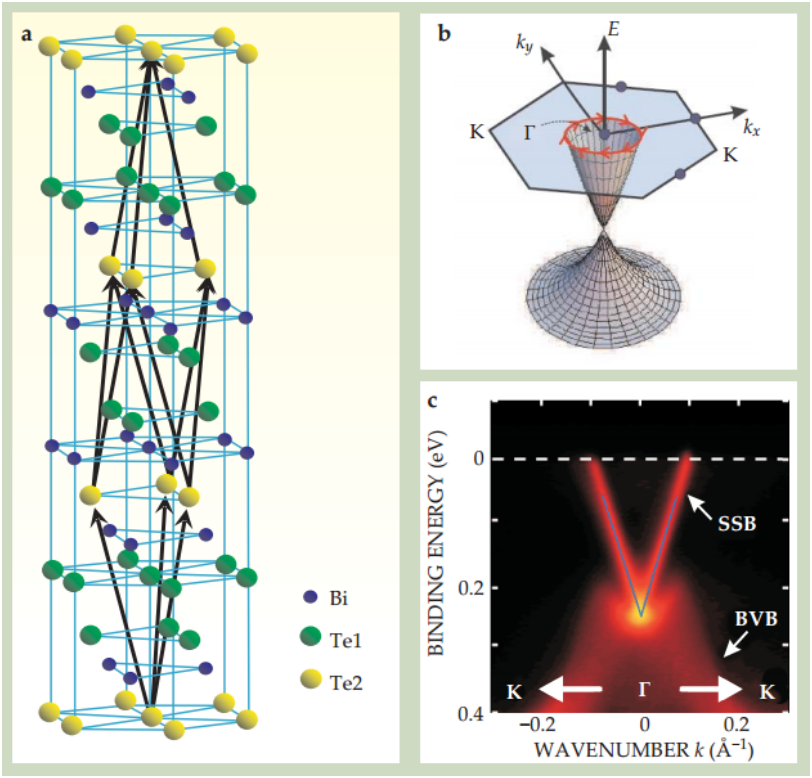

Figure 1.13: In 3D TIs, the linearly dispersing edge states become surface states described by a so-called Dirac cone. (a) The crystal structure of the 3D TI Bi_2Te_3 consists of stacked quasi-2D layers of Te-Bi-Te-Bi-Te. The arrows indicate the lattice basis vectors. (b) Spin dependent ARPES of the related compound Bi_2Se_3 reveals that the spins (red) of the surface states lie in the surface plane and are perpendicular to the momentum. (c) This ARPES plot of energy versus wavenumber in Bi_2Te_3 shows the linearly dispersing surface-state band (SSB) above the bulk valence band (BVB). The dashed white line indicates the Fermi level. The blue lines meet at the tip of the Dirac cone. Adapted from ref. [34].

TIs to obtain a single edge state as opposed to both. This question forms the basis for the exotic QAHE which I will introduce in the next section.

1.2.4 Quantum Anomalous Hall Effect

Now that we have the Hall effects all laid out, how can we get a quantized version of the AHE? In essence, the QSHE is made up of two quantum anomalous Hall effects (QAHE), i.e. there are two counter-propagating edge states of opposite spin due to the band inversion of both spin channels. How can we then suppress one spin channel to expose the QAHE?

Ferromagnetic (FM) order in TIs has been found to suppress one of the spin channels[38]. This system, consisting of a single spin channel, houses many interesting phenomena and applications. For example, the QAHE, topological magnetoelectric effect[39], as well as image magnetic monopoles[40]. In addition to relevance to fundamental physics research, there are also a number of technological applications that are hoped to result from this exotic effect. The quantization of the Hall resistance could be used as a simple resistance standard where no large magnetic field is needed and the dissipationless edge channels could be used to reduce power dissipation in electronics or as a spin-filter in spintronics.

An explanation for the suppression of one of the edge channels can be understood in terms of SOC and magnetic exchange coupling. In the last section we learned that SOC is responsible for the band inversion in the TI. Each band is spin degenerate with spin-up and spin-down bands. The addition of local magnetism through exchange coupling lifts the degeneracy of these bands. If the material is magnetized in the spin-up direction, for example, the spin-up bands will shift to lower energy, and the spin-down bands will shift up in energy. If the exchange coupling is large enough, the spin-up bands will cross each other and invert a second time, after the SOC inversion, forcing the spin-up state to become insulating again, while the spin-down state remains topologically insulating[41]. Thus, the spin-up channel is suppressed by TRS breaking and we are left with the QAHE, as depicted in Fig. 1.14.

When the Fermi level is tuned into this energy gap, the Hall resistance will become quantized and the longitudinal resistance will reduce to zero as in the QH case. However, similar to the AHE, the transverse resistance will trace out a hysteresis loop with an applied magnetic field and the longitudinal resistance will peak at the locations where the transverse resistance does not plateau, as depicted in Fig. 1.15.

This leads to some criteria for QAHE systems. First, the material must be 2D, second it must be insulating in the bulk, third, the bands must be topologically non-trivial, mostly

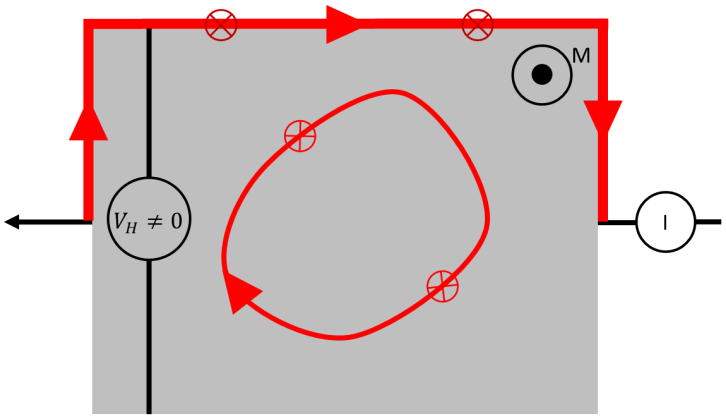

Figure 1.14: Schematic showing QAHE chiral edge state composed of spin-down electrons (in plane spin direction) with magnetization of the ferromagnetic material out-of-plane. There is only one chiral edge state since magnetic exchange has inverted the spin-up states a second time deleting the spin-up edge state. By this asymmetry there is a non-zero Hall voltage.

due to strong SOC, and fourth, TRS must be broken by magnetic order, most simply, FM long-range order.

Early proposals for 2D QAHE systems involved magnetic doping of HgTe/CdTe[29, 30] and InAs/GaSb[42] QWs. For example, Mn^{2+} would replace Hg^{2+}, allowing exchange coupling, and it was shown that this system should exhibit the QAHE as long as the Mn magnetization was strong enough[41]. As shown in Fig. 1.16, the exchange coupling opens a gap between the symmetric spin states, but reduces the gap between the antisymmetric states, crossing them and inverting them again (after SOC inversion), allowing only the symmetric spin states to remain edge states.

However, this required an external magnetic field, since this material is actually paramagnetic and behaves as a spin-glass at low temperatures[43]. This is not ideal because an external magnetic field will induce the QHE through landau quantization in addition to QAHE states.

Other proposals include thin film FM Weyl semimetals (essentially a 3D version of

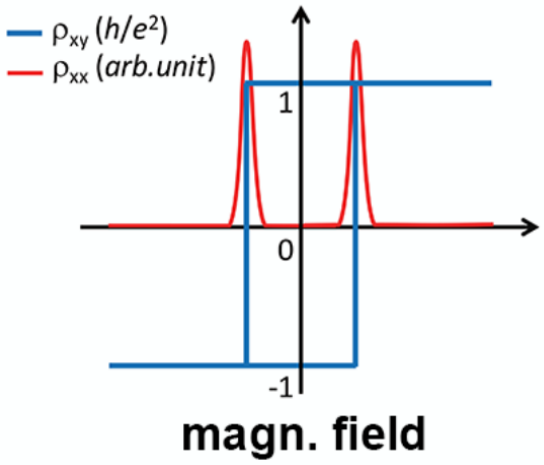

Figure 1.15: The QAHE has quantum Hall features with zero applied field. The transverse resistance is precisely quantized at h/e^2, where h is Planck's constant and e the elementary charge, and the longitudinal resistance vanishes at zero field. Adapted from ref. [15].

graphene where TRS is broken by FM) such as $HgCr_2Se_4$[44], or graphene grown on top of a magnetic material[45], doping graphene with transition-metal atoms[46], or by creating honeycomb lattices of transition-metal oxides with perovskite structures[47], also placing heavy metals on magnetic insulators[48], or strained epitaxial films with interface band inversion such as EuO/GdN[49] or EuO/CdO[50], or sandwiching a TI in between FM insulators[51], or FM insulators grown on TIs like EuS/Bi_2Se_3[52], allowing the magnetic proximity to open a gap for surface states at the TI boundary, as depicted in Fig. 1.17(b).

However, these proposals have complications such as the magnetic exchange gap being too small for laboratory temperatures or, in the case of the FM insulator sandwich, the interface is susceptible to imperfection, among other explanations, due to the FM insulator growth.

It has also been shown, however, that magnetic doping in TIs exhibit FM behavior[54]. The only successful proposal so far has been to induce exchange splitting in TIs by magnetic ion doping to make a FM semiconductor, as depicted in Fig. 1.17(a)[38, 55–57]. This has been realized experimentally in 2013 by Cui-Zu Chang et al. in $(BiSb)_2Te_3$ doped with

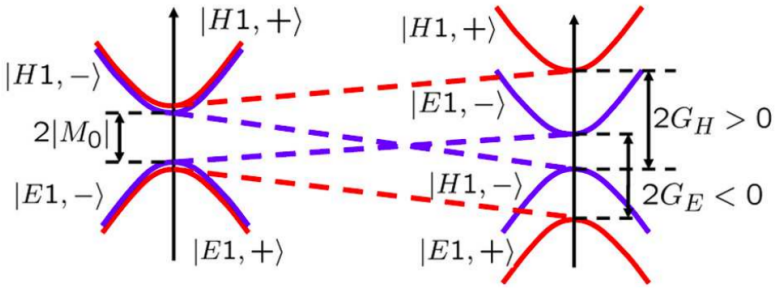

Figure 1.16: Evolution of band structure and edge states upon increasing the spin splitting. Due to exchange coupling, if the magnetization is < 0, the spin-up states separate in energy and the spin-down states come closer together to invert their bands. The additional band inversion cancels the initial SOC band inversion and leaves the spin-up states as surface states. Adapted from ref. [41].

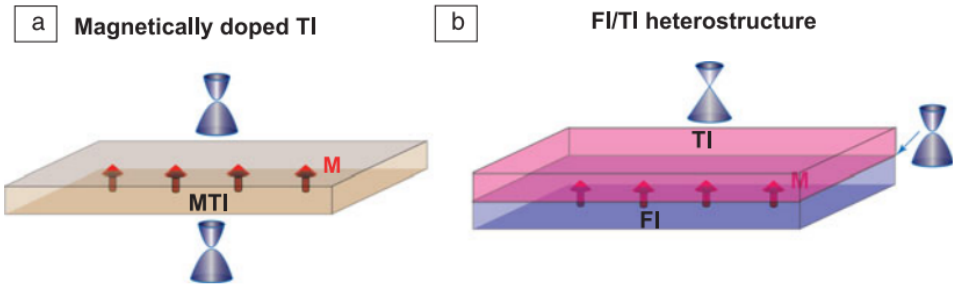

Figure 1.17: Structures of (a) magnetically doped TI films and (b) a ferromagnetic insulator (FI)/TI heterostructure. Adapted from ref. [53].

magnetic Cr ions[55] and later studied by other groups[15, 56, 58–61]. Recently, even higher precision and temperature has been attained with V doping[57, 62], due to increased FM ordering. The QAHE in these magnetically doped thin films are limited to extremely low temperature becuase of the inherent disorder, although the disorder effects can be partially alleviated by material engineering[63–65].

Not only is a more precise QAHE useful in metrology, for things like a simple resistance standard and for measuring fundamental constants, like the fine structure constant, in the laboratory, but it would also be useful in dissipationless electronics for low power consumption. It is now just a question of how to raise the temperature required to enter

the QAHE regime, which no study has, so far, been able to increase above ∼300 mK due to the small magnetic exchange gap, even though SOC and FM order can be realized at room temperature.

1.2.5 Topological Dirac and Weyl Semimetals

If a crystal respects both TRS and IS and band inversion occurs, we saw earlier that sufficient SOC opens up a gap between the inverted valence and conduction bands. However, if the crystal has some other crystalline symmetries, such as rotational symmetry, SOC may open a band gap at all momenta where the bulk conduction and valence bands touch except at special momenta along the symmetry axis, as depicted in Fig. 1.18.

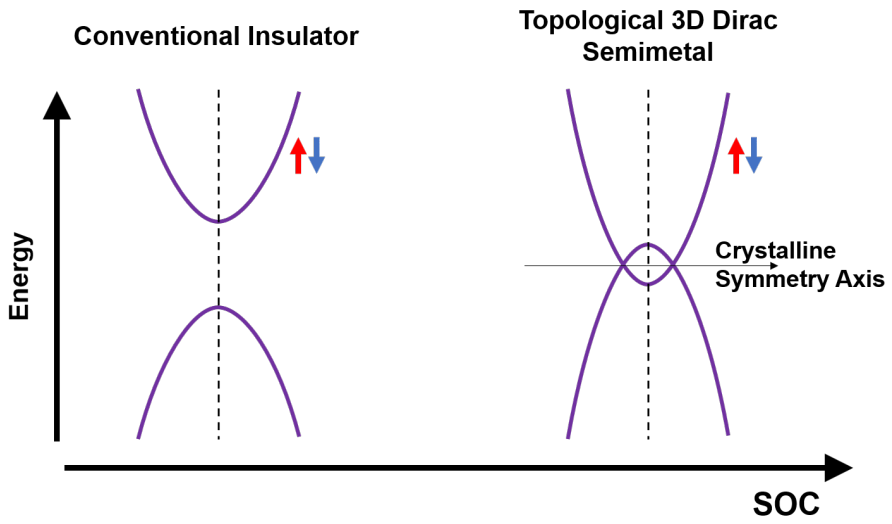

Figure 1.18: Schematic of conventional band insulator and topological Dirac semimetal bands. Bands inverted by SOC may have specific points in momentum space that are protected by certain symmetries besides TRS and IS. The energy dispersion around these points in linear, 3D massless Dirac fermions emerge.

At these special momenta, the protected degeneracy of the bands results in the emergence of 3D massless Dirac fermions, since locally the energy dispersion is linear along all three momentum directions. They are akin to the 3D analog of graphene. These materials are no longer insulators, but semimetals, hence 3D Dirac semimetals. This is because the

conduction and valence bands have a finite overlap. It should be noted that even though there are points where the band gap closes, there are still 2D momentum planes with a full inverted band gap (2D quantum Hall planes), thus topological classification still exists. Theoretically the Dirac semimetal state was predicted in 2012[66] and recently discovered experimentally in Na_3Bi and Cd_3As_2[67–70].

If now we have a band inverted crystal that respects TRS, but not IS, or vice versa, and sufficient SOC, there will be an even number of non-degenerate inverted bands with gapless closings, as depicted in Fig. 1.19.

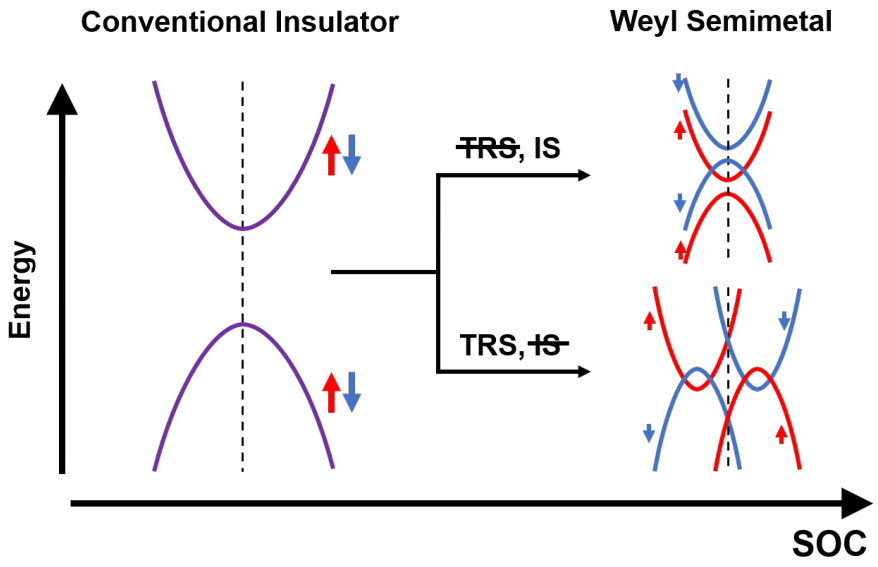

Figure 1.19: Schematic of conventional band insulator and topological Weyl semimetal bands. Bands inverted by SOC, where either TRS or IS is broken, become non-degenerate and form an even number of gapless closings where Weyl fermions emerge.

At these closings emerge Weyl fermions[71, 72]. Each Weyl node represents a monopole/antimonopole of Berry flux and carries its own chirality, giving them their topological protection[72]. Thus Weyl nodes generically occur in 3D magnetic or noncentrosymmetric materials with the strong SOC. What makes TWS appealing is the exotic electronic properties, such as the open surface Fermi arc[73, 74] and the chiral anomaly in transport measurements[75, 76]. The first type of Weyl fermion was predicted and observed in TaAs

family of compounds in 2015[77–80].

1.3 Antiferromagnetic Topological Insulators

This chapter will be primarily focused on AFM TIs, although there are quite a few theoretical and experimental topological AFMs around today which deserve mention. For example, the AFM Dirac semimetals $SrMnBi_2$, which features enhanced mobility similar to graphene[81, 82], and $EuMnBi_2$, which features the QHE due to quasi-two-dimensional Dirac fermions in the Bi sublattices where the effect of the field is mediated by the Eu sublattices[83] (see chapter 3 for our magnetic imaging results on $EuMnBi_2$). Topological Weyl semimetal states have also been realized in the paramagnetic and AFM phases of GdPtBi[84, 85]. The quasi-two-dimensional Kagomé Weyl semimetal $Co_3Sn_2S_2$ may also feature a hidden AFM order that could be contributing to its magnetic Weyl state. A real-space order parameter can also take the place of a momentum-space order parameter in non-collinear or non-coplanar AFMs giving rise to the topological Hall effect[86]. Here, the fictitious magnetic field that acts on the Bloch electrons comes from the chirality of the spin-texture rather than SOC. Recent examples of this effect were recently observed in the non-collinear AFMs Mn_3Sn and Mn_3Ge[87–89]. These spin-textures can also form topologically protected objects called AFM skyrmions, which can also give rise to topological Hall or spin Hall effects[90–93].

As we have seen, there are many interesting quantum phenomena in TIs and semimetals. However, topological effects that require intrinsic broken TRS require some kind of magnetic order[51], for example the QAHE, outlined in the previous sections. As this endeavor has proven to be fruitful, building the bridge to other exotic effects like chiral Majorana modes and topological magnetoelectric effect[51, 94, 95], that bridge however, needs another reinforcement. Since the QAH materials up to now require magnetic dopants to attain their QAH states, there is much inhomogeneity in the electronic structure and magnetic

properties, not to mention the quality is sensitive to details of the growth process[61, 96, 97]. These issues are mainly responsible for the extremely low temperatures required for the quantum effects, even though the magnetic ordering and exchange gap temperatures are much higher. Ideally then, such a system would be both stoichiometrically magnetic and topological, rather than relying on complicated magnetic doping.

1.3.1 Antiferromagnetic Topological Insulator Building Blocks

The simplest way to realize the AFM TI state is to take a strong TI (odd number of Dirac cones in its surface spectrum) and add an antiferromagnetic order (staggered magnetization) which also doubles its unit cell. In this way it breaks both primitive lattice symmetry $T_{1/2}$ and TRS Θ, but preserves the combination $S = \Theta T_{1/2}$. It can be shown for a 3D band structure, S leads to a non-trivial $\mathbb{Z}_2$ invariant[98].

Just as the QSH insulator can be thought of as a stack of QH layers with opposite spin and opposite Chern numbers[22, 99], one can also think of the AFM TI as a similar stack, but with each layer offset from one another, as shown in Fig. 1.20.

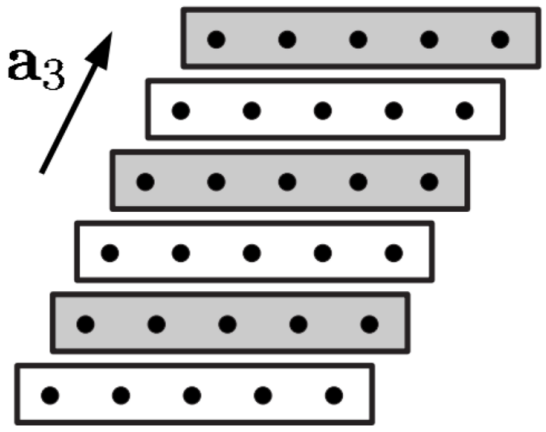

Figure 1.20: Schematic of stack of staggered Chern insulators with alternating Chern number, representing an antiferromagnetic topological insulator. Adapted from ref. [98].

The Hall conductance in the bulk averages to zero, since the conductance of each layer

is cancelled by each opposite layer. The top and bottom surfaces however have no magnetic neighbors on one side to cancel them out and have their surface states gapped out, due to TRS broken by magnetic exchange, forming chiral edge states on the edge of the layers each having a conductivity of $\pm e^2/2h$, depending on the magnetization direction. If the number of layers is odd, then the top and bottom layers have the same magnetization and the same Zeeman field directions and thus, conductivities of equal sign, both $+e^2/2h$ or both $-e^2/2h$, giving a total slab conductivity of $\pm e^2/h$, an integer multiple of $\pm e^2/h$ as it should always be[17]. If the number of layers is even, then the top and bottom layers have opposite magnetization and opposite Zeeman field directions and opposite sign conductivities, giving a total slab conductivity of zero with vanishing chiral edge states[39]. Note, the side surfaces are gapless since the moment is in plane, S symmetry is preserved, but if the stack is thin enough, the side surface states become gapped[100, 101]. Depending on whether the stack has an even or odd amount of layers can have a profound impact on the quantum state.

1.3.2 Quest for High Temperature Quantum Anomalous Hall Effect

When the number of layers in the stack is odd, the total Chern number of the stack is $C = 1/2 + 1/2 = 1$ or $C = -1/2 - 1/2 = -1$, depending on the magnetization. This state gives rise to the QAHE, since there is no external magnetic field required to break TRS. This state has been realized recently in exfoliated flakes of the AFM TI, $MnBi_2Te_4$, a material that will be discussed in detail later in chapters 3 and 4[102]. Deng et al. saw quantization of the Hall resistance at zero-applied magnetic field within 3% of h/e^2 and very close to quantized at $\sim$ 2.5 T in a five septuple (SL) layer sample at 1.4 K, as shown in Fig. 1.21a. It should be noted that this high-field QAH is adiabatically connected to the zero-field QAH state, so they are topologically the same, and the state at high-field is not from Landau levels[102]. Although the quality of quantization drops quickly at zero-field with higher temperature, depicted in Fig. 1.21b, the quantization was within 3% of h/e^2 under a field of 7.6 T up to a temperature of 6.5 K! Even higher temperatures have been

realized under high-field. J. Ge et al. found near quantization at -15 T in a 7 SL sample up to 45 K, as shown in Fig. 1.21c, in addition to the appearence of a higher Chern number of two (two chiral edge states) in a 10 SL sample[103]. Now, when the number of layers is even, another exotic quantum phase emerges, the axion insulator state.

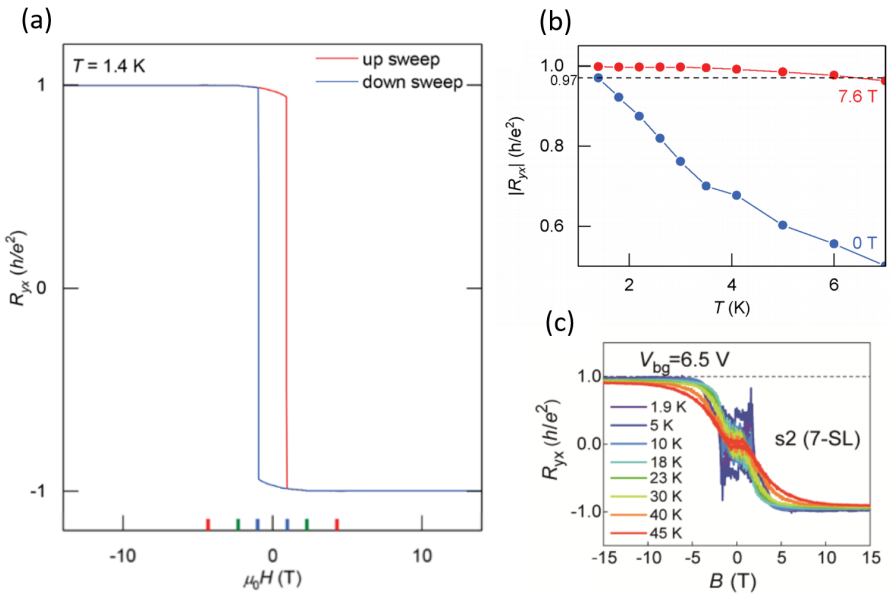

Figure 1.21: (a) Quantum anomalous Hall effect in a five-layer $MnBi_2Te_4$ flake. Magnetic-field-dependent R_{yx} acquired at 1.4 K. Up and down sweeps of the magnetic field are shown in red and blue, respectively. R_{yx} reaches $0.97h/e^2$ at $\mu_0 H = 0T$ showing evidence of zero-field QAH effect. External magnetic field polarizes the ferromagnetic SLs individually, and further improves the QAH quantization; R_{yx} quantizes to $0.998h/e^2$ under magnetic fields above $\mu_0 H \sim 2.5T$. Adapted from ref. [102]. (b) Anti-symmetrized $|R_{yx}|$ as a function of temperature obtained under external magnetic fields of $\mu_0 H = 7.6T$ (red) and $\mu_0 H = 0T$ (blue). The QAH quantization temperature (defined as the temperature below which $|R_{yx}|$ within 3% of the resistance quantum) reaches T = 6.5 K under $\mu_0 H = 7.6T$[102]. (c) High-temperature QHE without Landau Levels in 7-SL $MnBi_2Te_4$ device. The nearly quantized Hall resistance plateau can stay at the temperature up to 45 K (Hall resistance plateau of $0.904h/e^2$). Adapted from ref. [103].

1.3.3 Axion Insulator

In a 3D TI in the axion insulator state, there exists a quantized magnetoelectric coupling in the electromagnetic Lagrangian[39, 51, 104]:

$$\Delta\mathcal{L}_{EM} = \frac{\theta e^2}{2\pi h}\mathbf{E}\cdot\mathbf{B},\ \theta = \pi. \tag{1.9}$$

This implies that when an electric field is applied, a circulating surface current is induced, giving rise to a magnetization, or when a magnetic field is applied, an electric polarization is induced. In an ordinary insulator, θ is 0, but in topological insulators with TRS or IS, θ is π.

In a AFM TI with S symmetry, the space-averaged θ is either 0 or π, since θ is odd under S. In the $\theta = \pi$ case, the surfaces can either be metallic or gapped, and in the latter there must be a half-integer QHE. As we saw earlier, broken TRS on the surface of an AFM TI leads to gapped surface states. If the magnetization of the top and bottom surfaces are opposite, as in the even layer stack, the stack will have zero Hall conductivity, because of the cancelling Hall conductivities, leading to insulating behavior and giving rise to the axion insulator state.

This axion insulator phase characterized by zero Hall resistance and large longitudinal resistance has recently been realized in 6 SL $MnBi_2Te_4$ and interestingly a phase transition to the Chern insulator phase, characterized by a quantized Hall resistance and zero longitudinal resistance can be induced with moderate external magnetic field[105]. Fig. 1.22 shows the axion insulating state at zero field and the Chern insulating state at -9 T.

1.3.4 Chiral Boundary Modes at Step Edges and Domain Walls

Imagine now there are extra layers on top of the stack forming step edges. Since each extra layer has opposite magnetization and opposite Chern number. This is similar to the situation where a chiral boundary mode with conductance e^2/h will form between two quantum Hall domains whose conductance differs by one. Here, there will be a chiral

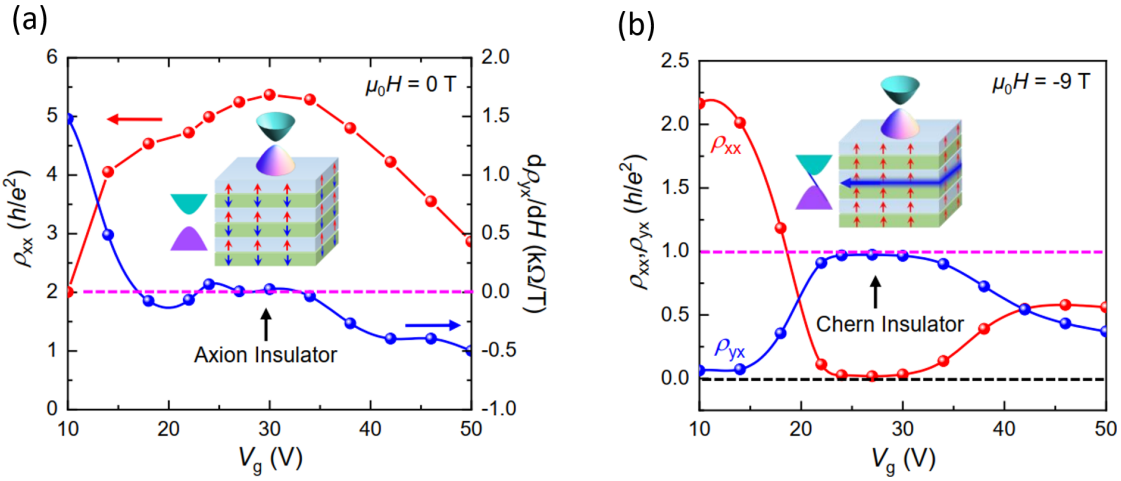

Figure 1.22: Gate dependent transport properties and magnetic-field-driven axion insulator to Chern insulator transition. Adapted from ref. [105]. (a) Gate-voltage dependence of ρ_{xx} and the slope of ρ_{yx} vs. $\mu_0 H$ measured at T = 1.6 K around zero magnetic field. The axion insulator state with AFM order and gapped electronic structures is illustrated in the inset. The slopes of ρ_{yx} are obtained by linear fitting between ±2 T. (b) The evolution of ρ_{xx} and ρ_{yx} as a function gate-voltage at T = 1.6 K and $\mu_0 H$ = -9 T. The inset displays the schematic FM order and electronic structure of the Chern insulator state with a chiral edge state across the band gap.

boundary mode that forms on the step edge[98, 106], as shown in Fig. 1.23a. This edge mode could be probed by scanning tunneling microscopy or similar.

A similar situation can be imagined at the intersection between two AFM domains, e.g. two stacks side by side with the same number of layers, but opposite alternating magnetization. At this intersection, the spin would have to rotate in-plane between the domains, in order to connect the two domains, i.e. form a domain wall. When the magnetization is parallel to the surface, TRS is no longer broken there and the surface gap will close, as depicted in Fig. 1.23b, although the chiral mode may shift in momentum[98, 107].

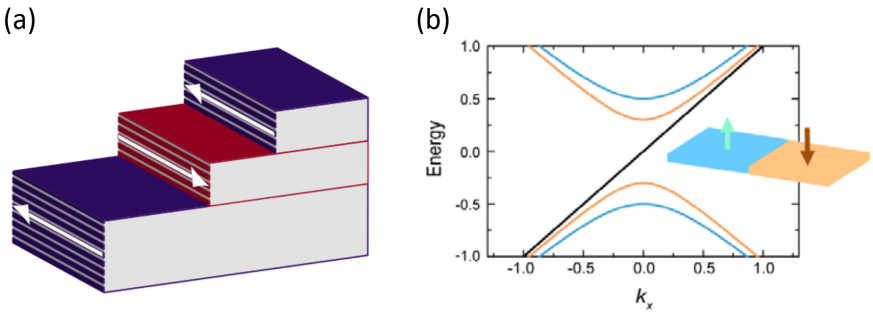

Figure 1.23: (a) Chiral edge states on step edges. The red and blue regions represent ferromagnetic layers magnetized in opposite directions. There is a gapless chiral quantum wire at each step edge with chirality indicated by the arrow at the edge. Adapted from ref. [98]. (b) Energy spectrum with a single chiral mode at the surface of $MnBi_2Te_4/(Bi_2Te_3)_n$ with a magnetic domain wall. Adapted from ref. [107].

1.4 Perspective

As we have seen, the AFM states in these systems play a huge role in the formation of topological phases. It is imperative to understand both the spin and AFM domain configurations in order to understand how the magnetism in these systems connects to the topological orders. Despite the huge amount of research in this class of materials, there is very little known about the AFM domain formation. The device sizes in these previous studies are also quite small $\sim 10\mu m$. If the AFM domains in these systems are smaller than the device sizes, there will be multiple domains with opposite signs, cancelling out the topological magnetoelectric response or QAHE[108]. Thus, it is imperative to visualize how large the AFM domains are in these systems, how they interact with each other and how they depend on magnetic field and temperature. Additionally, the nanoscale imaging of these AFM domain walls and step edges could open up exploration of the chiral boundary modes residing on them.

Chapter 2

Experimental Methods

In this chapter, we first present the technique that we use to study and characterize domain formation in magnetic materials, a scanning probe microscopy technique called magnetic force microscopy (MFM) and in-situ electrical transport. The principle behind MFM will be discussed. Next, a sophisticated homemade variable-temperature MFM setup to simultaneously measure MFM and in-situ transport will be discussed. Followed by examples of some of the artifacts that can show up in MFM images.

2.1 Introduction to Magnetic Force Microscopy

Understanding magnetic order in condensed matter is one of, if not the most, important areas of research in modern condensed matter physics. By introducing magnetism into certain systems, some exotic phenomena can be achieved. For example, the possible coupling of ferromagnetic order and ferroelectric order may lead to giant magnetoelectric effect[109, 110]. Introducing ferromagnetism in topological insulators can lead to many fascinating quantum phenomena, such as QAHE[55], and topological magnetoelectric effect[111]. In these exotic magnetic systems, where magnetic domains form on scales below the resolution of the measurement device, their net magnetization is averaged out, which is unlikely to be detected by larger measurement devices like a superconducting quantum interference device (SQUID). On the other hand, visualizing the magnetism at the nanoscale is very useful in understanding the properties of mesoscopic magnetic objects, such as skyrmions, magnetic domains and domain walls, and magnetic quantum dots.

Up to now, many magnetic imaging techniques enable the real-space characterization of magnetism at the nanoscale. For example, MFM[112], scanning SQUID techniques[113] and nitrogen-vacancy (NV) magnetometry[114] directly measure the magnetic field or field gradient. Other optical techniques for magnetic imaging are also very popular, such as magneto-optical Kerr effect (MOKE) microscopy[115] and scanning transmission X-ray microscopy (STXM)[116]. Among them, MFM, which is a relatively traditional technique, is still widely used in the field of condensed matter physics and material sciences. Although it may not have the same high-sensitivity as scanning SQUID and spatial resolution as NV magnetometry, MFM can be used in a wider range of temperature and magnetic fields. This enables the study of a wide variety of magnetic materials. Compared to those optical techniques, MFM usually has a better spatial resolution. In addition, it is a table-top microscope, which can be realized in most labs without the need of synchrotron based light sources. Moreover, the optical method, by utilizing Kerr effect to probe magnetism, is an indirect magnetometry, which effectively measures the AC AHE at finite frequency.

The MFM, built on the basis of atomic force microscopy (afm), belongs to the scanning probe techniques[117]. afm was invented by Binnig *et al.* in 1986[118], shortly after the invention of scanning tunneling microscopy (STM)[119], which is a powerful technique to image individual atoms. Although traditionally afm does not have the atomic resolution, it is less sensitive to surface contamination and mechanical vibrations, therefore can be used at ambient conditions. The basic principle of afm is to detect the atomic force, which typically consists of long-range attractive van der Waals, electric or magnetic forces and short-range repulsive forces from Coulomb repulsion or Pauli exclusion, as shown in Fig. 2.1. Different operation modes are utilized for different purposes. For topographic imaging, a contact mode or tapping mode are often used. In the contact mode, the afm tip, on the end of a cantilever, is pressed on the sample surface. The repulsive atomic force causes the bending of the cantilever. Such small deflection can be accurately detected by various methods, *e.g.*, the laser-based position sensors, piezoresistive cantilevers,

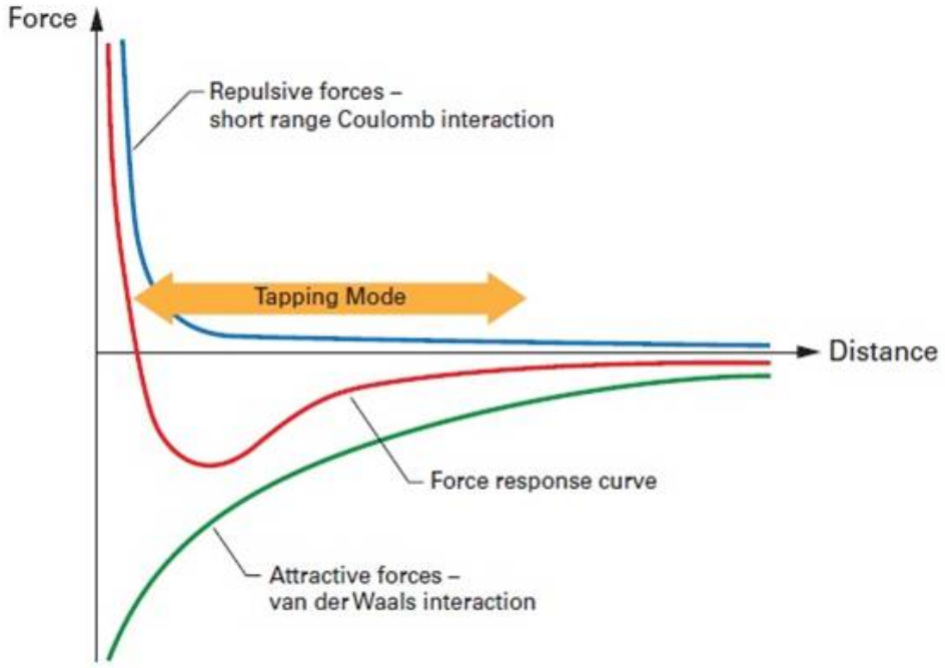

Figure 2.1: The force response curve (red) is a sum of long distance attractive van der Waals force (green) and short range repulsive force (blue).

and interferometric sensors. During the scanning process, the feedback electronics try to keep the deflection constant by controlling the z position of the cantilever. The mapping of z manifests the topography of the surface. The drawback of contact mode is the contact force exerted is relatively high. This usually causes the damage of a soft sample surface and the reduced lifetime of the afm tips. To circumvent this problem, a tapping mode (or intermittent-contact mode) is used for topographic imaging. The afm tip is driven at its resonance frequency. The amplitude of the oscillation is used as the feedback parameter in this case. This mode is more commonly used for topographic imaging, due to less damage to both the samples and afm tips. A standard afm setup can have high lateral resolution $\sim$10 nm and high vertical resolution $\sim$1 nm. If the tip is lifted above the surface $\sim$100 nm, the short-range atomic force is negligible and the long-range interactions, such as magnetic and electrostatic forces, dominate. MFM imaging operates in this so-called non-contact mode.

Figure 2.2 shows a schematic MFM setup. A standard procedure of MFM imaging is the interleave mode: it first scans the topography in tapping mode, then the tip is lifted to maintain constant height from the surface in non-contact mode. This interleave mode minimizes the topographic contamination in the MFM images, which is widely used in ambient conditions. However, scanning the topography sometimes alters the magnetic domain structures, if the sample is magnetically soft and tip moment is large. For instance, magnetic thin films usually have relatively lower magnetic moments per unit area, which requires a large moment tip to probe. If the thin films have a coercive field H_C smaller than the stray field near the magnetic tip, the topographic scanning can modify the domain patterns, leading to some artifacts in the MFM images. Thus, interleave mode is not preferable. In thin film samples, the surface is usually quite flat, with a roughness $\sim$ 1 nm. Thus, interleaved topographic imaging is not necessary. However, the tilt of the sample surface should still be determined. The typical scanning procedure for magnetic sample can be described by two steps: first, scan the topography of the sample surface in another area,

away from the area for MFM scanning; next, lift the tip up and move the tip to the desired area. During MFM imaging, the tip always follows the slope of the surface to maintain a constant lift height.

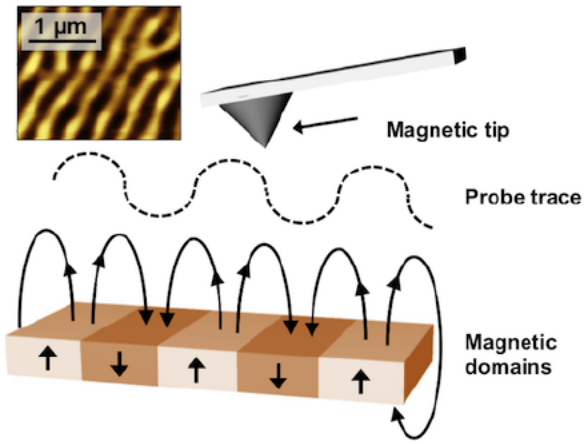

Figure 2.2: Schematic of standard MFM probe showing magnetic tip above surface of ferromagnetic domains. Example probe signal (dotted line) and stray fields (solid lines) are shown. Inset shows example of MFM scan of Co stripe domains.

The interaction between the sample and magnetically coated afm tip can be approximated by a dipole-dipole interaction[120]. The interaction energy U can be expressed as the dot product of the moment of either dipole into the field from the other dipole:

$$U = -\mathbf{m} \cdot \mathbf{B} \tag{2.1}$$

where $\mathbf{m}$ is the magnetic moment of the tip and $\mathbf{B}$ is the magnetic stray field from the sample. Since the magnetic moment of the tip usually points to z direction, the equation can be rewritten as $U = -m_z \cdot B_z$. The interaction between the sample and the tip is the gradient of the interaction energy:

$$F = -\nabla U = m_z \frac{\partial}{\partial z} B_z \hat{z} \tag{2.2}$$

This force acting on the tip has a z dependence. Such force gradient effectively changes the spring constant of the cantilever, leading to a resonance frequency shift. Consider the

cantilever as a spring with a spring constant k_0. The total force F_t acting on the cantilever includes both restoring force and magnetic force:

$$F_t = -k_0 \cdot z + F = -k_0 \cdot z + F_0 + F_z^{'} \cdot z + \frac{1}{2} F_z^{''} \cdot z^2 + ... \tag{2.3}$$

Take into account the 1st order term of F, the magnetic force gradient effectively changes the spring constant of the cantilever: $k{=}k_0{-}F_z^{'}$. The resonance frequency of the cantilever can be expressed as:

$$f = \frac{1}{2\pi}\sqrt{\frac{k}{m}} = \frac{1}{2\pi}\sqrt{\frac{k_0 - F_z^{'}}{m}} = f_0(1 - \frac{F_z^{'}}{k_0})^{\frac{1}{2}} \approx f_0 - f_0 \frac{1}{2k_0} F_z^{'} \tag{2.4}$$

So the resonance frequency shift Δf caused by the magnetic force gradient can be expressed as:

$$\frac{\Delta f}{f_0} = -\frac{F_z^{'}}{2k_0} = -\frac{m_z}{2k_0}\frac{\partial^2 B_z}{\partial z^2} \tag{2.5}$$

The MFM measures the resonance frequency shift Δf of the cantilever, which is proportional to the second derivative of the stray magnetic field in z direction. The up and down magnetic domains lead to opposite MFM signals, *i.e.* attractive (repulsive) force decreases (increases) resonance frequency.

2.2 Experimental Setup

Figure 2.3 shows a schematic picture of the home-built cryogenic MFM system. This instrument is able to perform magnetic imaging in a wide temperature (2 K – 300 K) with *in-situ* high magnetic field (8 T) and high voltage (1 kV) The scanning probe has a compact design, a circular cylinder with an 8-inch height and a 1-inch base radius, and is suitable for liquid helium experiments. The apparatus is interfaced with a Nanonis SPM controller (SPECS) and Phase Locked Loop (SPECS). The deflection of the cantilever, with nominal resonance frequency of $f_0 \approx 42$ kHz and spring constant $k \approx 3$ N/m, is sensed by the piezoresistive

method, *i.e.*, the stress-induced resistivity change of piezo-resistive material integrated on the cantilever[121, 122]. The cantilever resistance is precisely balanced by a Wheatstone

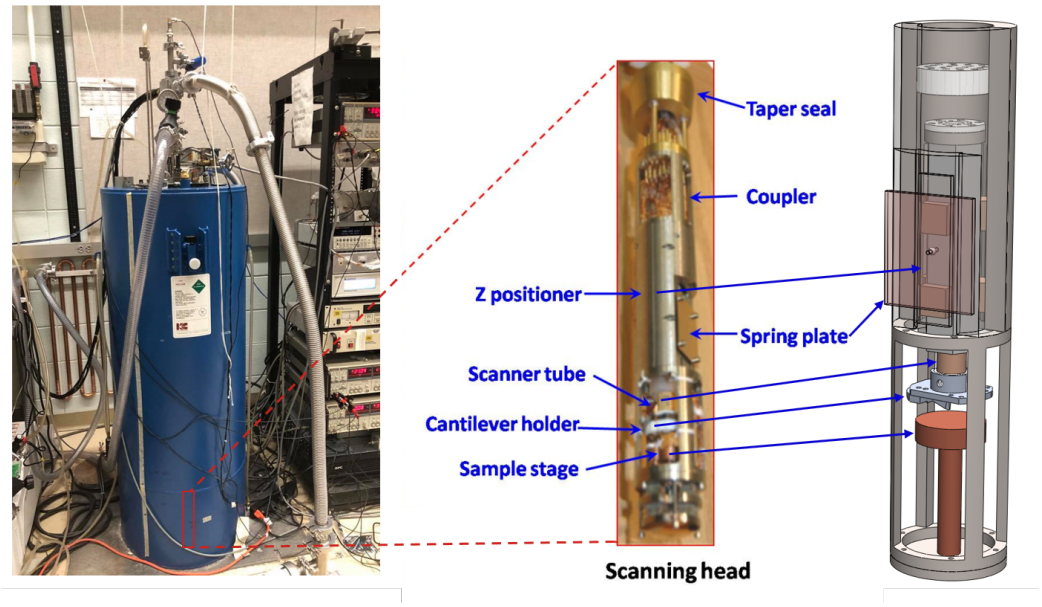

Figure 2.3: Schematic of home-built cryogenic MFM setup. Litrogen/He dewar (left), MFM scanning head (middle) and MFM head drawing (right).

bridge, shown in Fig. 2.4. The resistance difference between the cantilever and reference is amplified by 2000 times via a differential amplifier. This signal is then fed to the Nanonis controller as the deflection signal. The magnetic tips are prepared by coating the bare tips with nominally 150 nm Co film using electron-beam evaporation, which is capped with 2 nm Cr to prevent oxidation. The magnetic tip is usually magnetized by a strong magnet at ambient condition before MFM measurements. MFM images are taken in a constant height mode with the scanning plane nominally ∼50-100 nm above the sample surface.

In an itinerant ferromagnet, the transport properties may correlate with the magnetism, examples include magnetoresistance, AHE, and topological Hall effect. In order to study the interplay between the transport properties and the magnetism, it is imperative to combine MFM and *in-situ* transport measurements. Fig. 2.5 shows an optical image of gold leads attached to a $MnSb_2Te_4$ single crystal by silver epoxy in a Hall configuration ready for MFM and *in-situ* transport measurements. The Hall resistance and longitudinal resistance are measured by standard lock-in techniques with an alternating current of 100-2000 μA

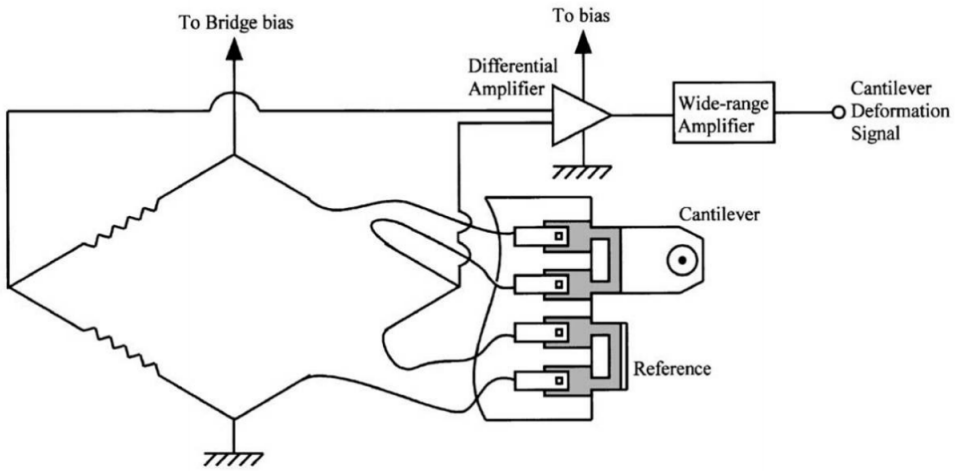

Figure 2.4: Schematic of the self-sensing piezo-resistive cantilever circuit. The cantilever deflection is monitored by the change of the resistance, which is precisely measured by the Wheatstone bridge. Adapted from ref. [121].

modulated at 314 Hz. A DC voltage is also applied to the sample in order to nullify the electrostatic interaction between the tip and sample.

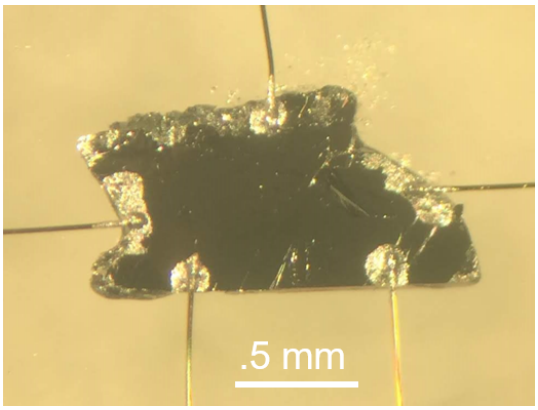

Figure 2.5: Optical image of $MnSb_2Te_4$ single crystal with gold wires attached by silver epoxy for in-situ Hall transport.

Scanning artifacts can show up in the MFM images. Fig. 2.6 shows an example of scanning artifacts that often shows up in the MFM images. Figs. 2.6(a,b) show a "shadowing" effect that can come from the feedback parameters (proportional and integral) for

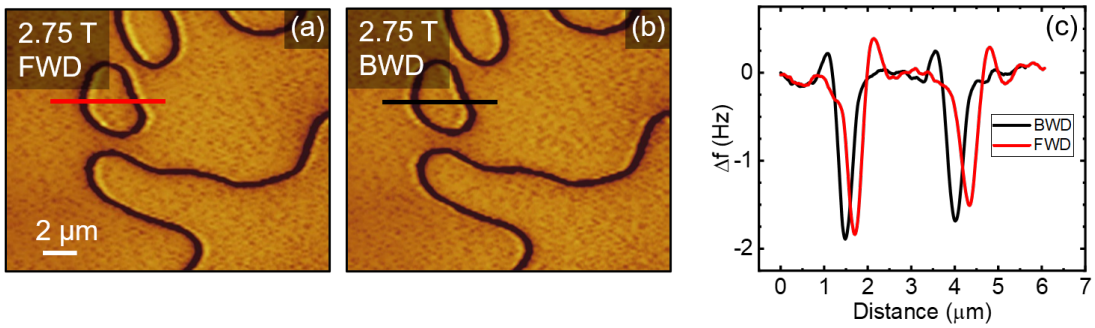

Figure 2.6: (a,b) MFM images with forward (FWD) and backward (BWD) scanning directions, respectively. (c) Line profiles of red and black lines in (a) and (b). The "shadowing" seen in the MFM images is symmetric between forward and backward scanning directions, and thus is not an intrinsic effect. The color scale for the MFM images is 2 Hz.

the resonance frequency not being fast enough to react to the scanning speed. The effect will generally show up as an overshoot on the far side of the signal in the direction of the scan, as shown in Fig. 2.6(c).

More substantial artifacts can also show up like ghosting bands, shown in Figs. 2.7. More experimentation is required to figure out the origin, but a solution is to keep the sample stage lower towards the bottom of the MFM head to allow the top of the Z positioner to be further away from the cluster of wires at the top of the MFM head.

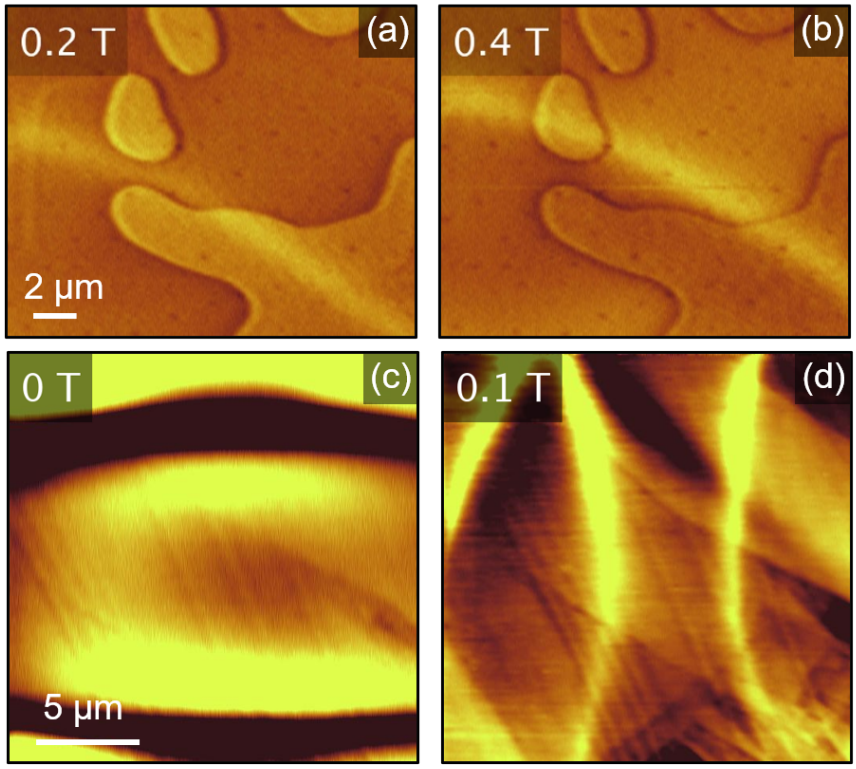

Figure 2.7: (a-d) MFM images with examples of field-dependent ghosting bands of unknown origin. The color scale for the MFM images is 0.3 (a,b) and 2 (c,d) Hz.

Chapter 3

Magnetic Imaging of Antiferromagnetic Domain Walls

Because of compensated magnetic moments, AFM order produces no stray field, possesses fast dynamics, and is insensitive to magnetic perturbation[123]. Thus, AFMs have been used as a pinning layer in spin-valve devices[123, 124]. Furthermore, the robustness and non-invasiveness of AFMs make them appealing for replacing the ferromagnetic active components in spintronic devices[123–125]. In addition, recent progress in topological materials suggest that many AFMs may host interesting topological states[86]. For example, it has been proposed that an axion insulator state with topological magnetoelectric response could be realized in an AFM TI phase[98, 106]. The AFM TI state adiabatically connects to a stack of quantum Hall insulators with alternating Chern numbers[126], thus it also provides a promising route to realizing a QAHE in stoichiometric materials. The prior observation of the QAH effect in magnetically doped TI thin films is limited to extremely low temperature because of inherent disorders[55–57, 60, 61, 63], though the disorder effect can be partially alleviated by material engineering[63–65]. The $MnBi_2Te_4$ family was predicted to be a promising candidate of AFM TI that may host QAH and axion insulator states in thin films with odd and even SLs, respectively[127–129]. Recent transport measurements on exfoliated thin flakes provide compelling evidence for these predictions[102, 105]. Although there has been a surge of research efforts in this class of materials, there is no report on the domain structure in these materials. Multiple domains with opposite signs would cancel each other, resulting in vanishing topological magnetoelectric response or QAH effect[108]. Therefore, it is imperative to visualize and control AFM domains or domain

walls (DWs) in these AFMs with topologically non-trivial band structure to explore topological phenomena[86, 123, 130]. The nanoscale imaging of AFM DWs would allow exploration of the chiral electronic states residing on edges or DWs[106, 108].

3.1 State of the Art Antiferromagnetic Domain Imaging

While imaging techniques of magnetic domains on the surfaces of ferromagnetic materials with, for example, magneto-optical Kerr effect microscopy and MFM have been available for a number of decades, AFM domain imaging is a relatively new development. Imaging AFM domains and domain walls has proven difficult because, as AFMs are made up of magnetic components, i.e. magnetic ions, one would think a magnetic probe would prove well, but the magnetic components set themselves up to zero-out magnetization, leaving magnetic probes untouched. Most AFM imaging techniques rely on secondary effects induced by the AFM order, e.g. optical birefringence due to magnetostrictive or piezomagnetic effects, non-linear optical response due to broken inversion symmetry, or local electron spin polarization induced by AFM order.

Examples of AFM imaging techniques[131] include optical methods (both linear and non-linear) like second harmonic generation (SHG) which is sensitive to domain contrast and which works particularly well on magnets with broken inversion symmetry, for example, Cr_2O_3[132], shown in Fig. 3.1a.

There are also scanning probe methods that are sensitive to domain and DW contrast, for example spin-polarized scanning tunneling microscopy (SP-STM)[133], shown in Fig. 3.1b, MFM[137] and magnetoelectric force microscopy (MeMFM)[110], shown in Fig. 3.1d. Synchrotron X-ray techniques are also important in imaging AFM domains and DWs. These include X-ray magnetic linear dichroism with photo-emission electron microscopy (XMLD-PEEM)[134, 135] shown in Fig. 3.1c, micro-X-ray diffraction[136] shown in Fig. 3.1e, and a new and unique technique using coherent soft X-rays to visualize antiphase AFM domains

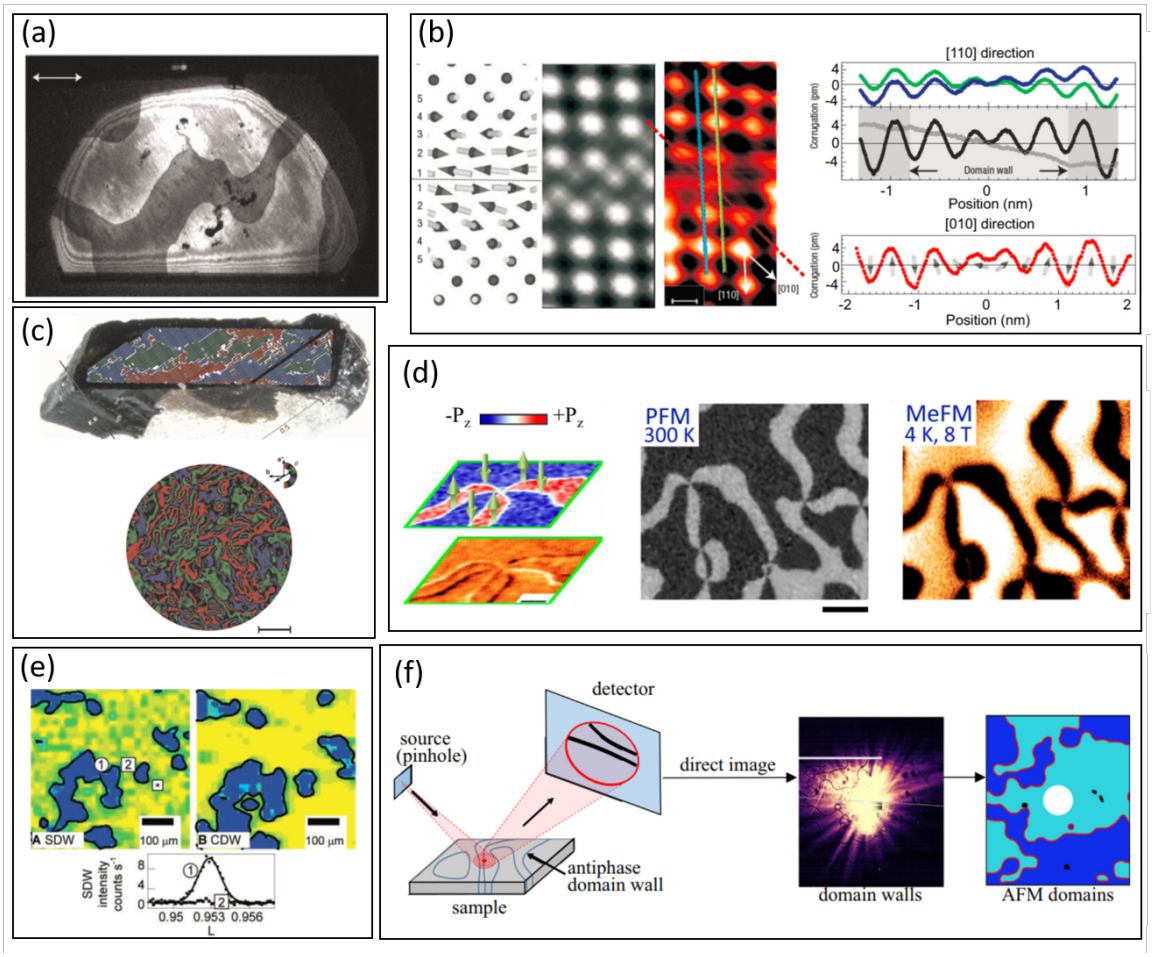

Figure 3.1: (a) Spatially resolved second-harmonic-generation image of the AFM 180° domain pattern in a z-oriented Cr_2O_3 sample. Adapted from ref. [132]. Scale bar: 1 mm. (b) Theoretical spin structure, and simulated and experimental SP-STM image of antiphase domain walls in the out-of-plane antiferromagnetic Fe monolayer on W(001). Adapted from ref. [133]. Scale bar: 300 pm. (c) Topography of the magnetic k-domains in rhombohedral $BiFeO_3$ single crystal (top) and vector map of the $\alpha - Fe_2O_3$ AFM domain configuration (bottom) from XMLD-PEEM. Red, blue and green colors represent scattering from each of the 120° domains. Scale bar: 2 μm. Adapted from refs. [134, 135]. (d) Room temperature peizo force microscopy (PFM) (top-left) and low-temperature MFM (bottom-left) images of the (001) surface of a hexagonal-$ErMnO_3$ single crystal. Scale bar: 1 μm. Adapted from ref. [110]. Room-temperature PFM image (left) and low-temperature MeMFM image (right). Scale bar: 3 μm. (e) X-ray microdiffraction images of AFM domains in Cr at T = 130 K. Adapted from ref. [136]. (f) X-ray Bragg diffraction phase contrast microscopy based on the detection of domain boundaries in the image of a magnetic Bragg peak (left). Due to the destructive interference, the boundaries are imaged on the detector as dark lines. 180° AFM domain boundaries (dark wavy lines) observed in the wings of the (001) magnetic peak in a collinear antiferromagnet $Fe_2Mo_3O_8$ (middle), and the corresponding antiphase AFM domain pattern (right).

called X-ray Bragg diffraction phase contrast microscopy (XBPM)[138], shown in Fig. 3.1f.

The advantages for MFM over other techniques (except SP-STM) however are that while maintaining similar spatial and magnetic resolution, external parameters such as magnetic field and temperature can be modified, in addition to in-situ transport. This allows AFM domain evolution across both field, e.g. spin-flop or spin-flip, and temperature, e.g. Néel, Curie, reorientation, transitions to be mapped and studied. Which opens up a whole new avenue of AFM domain exploration in many exciting materials.

3.2 Magnetic Susceptibility Contrast Imaging in Natural Uniaxial Antiferromagnets Using Magnetic Force Microscopy

In this chapter, we show direct visualization of AFM DWs in single crystals of $MnBi_{2-x}Sb_xTe_4$ (where, $x = 0,\ 0.63,\ 2$) and $EuMnBi_2$ using cryogenic MFM with *in-situ* transport. The rhombohedral crystal structure of $MnBi_{2-x}Sb_xTe_4$ can be viewed as inserting one Mn-Te layer into the quintuple layers of Te-Bi(Sb)-Te-Bi(Sb)-Te in $Bi(Sb)_2Te_3$, as shown in Fig. 3.2(a)[139].

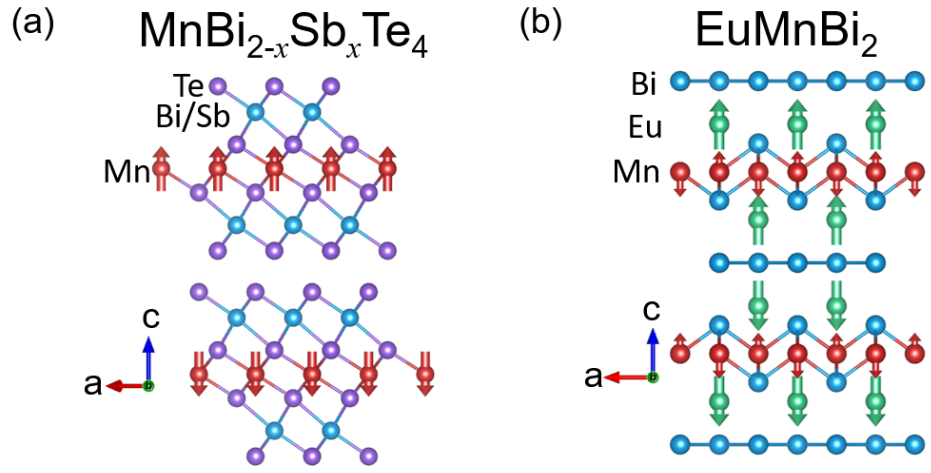

Figure 3.2: (a,b) A schematic illustration of crystal structure and magnetic order of $MnBi_{2-x}Sb_xTe_4$ and $EuMnBi_2$, respectively.

Platelike single crystals of $MnBi_{2-x}Sb_xTe_4$ were grown out of a Bi(Sb)-Te flux and have been well characterized by measuring the magnetic and transport properties[139, 140]. All three compositions order magnetically below T_N = 19-24 K with ferromagnetic Mn-Te layers coupled antiferromagnetically. Mn^{2+} ions adopt a high-spin S = 5/2 and order into an A-type AFM structure with ferromagnetic layers coupled antiferromagnetically along the c axis. An ordered moment of 4.04(13) μ_B/Mn at 10 K was found to align along the c axis by neutron diffraction[139]. $MnBi_{2-x}Sb_xTe_4$ is thus a unique natural heterostructure of magnetic layers intergrowing with layers of a topological insulator. It is worth mentioning that $MnBi_{2-x}Sb_xTe_4$ inherits van der Waals bonding between the quintuple layers in Bi_2Te_3. The space group is $R\bar{3}m$[139].

$MnBi_{2-x}Sb_xTe_4$ with x = 0.63 was investigated in this work because it stays close to the transition from n-type to p-type conducting behavior. The transport data and H-T phase diagrams derived from resistance anomalies are shown in Figs. 3.3-3.6 below. At 2 K, $MnSb_2Te_4$ shows a spin flip transition at ∼0.3 T with a magnetic field applied along the crystallographic c-axis. In contrast, $MnBi_2Te_4$ ($MnBi_{1.37}Sb_{0.63}Te_4$) shows a spin-flop transition at H_{SF} = 3.5 T (3.0 T) followed by moment saturation at H_S = 7.8 T (6.8 T).

$EuMnBi_2$ is a Dirac semimetal that consists of conducting layers of Bi square nets hosting quasi-2D Dirac fermions and insulating magnetic layers consisting of Mn-Bi and Eu[83] with S = 7/2 for Eu^{2+}. The space group is I4/mmm. The Eu moments order ferromagnetically in the ab plane and align along the c axis, where the Bi square nets intervenes between the Eu layers with magnetic moments up and down, as shown in Fig. 3.2(b). $EuMnBi_2$ single crystals were grown using Bi self-flux method using high purity Eu, Mn and Bi in 1:1:9 ratio placed in alumina crucibles in an Argon filled glove box and sealed in evacuated quartz tubes heated at 1000 °C for 10 hours, followed by cooling to 400 °C at 2 °C/hour. The excess Bi flux was removed by centrifuging to obtain plate like single crystals.

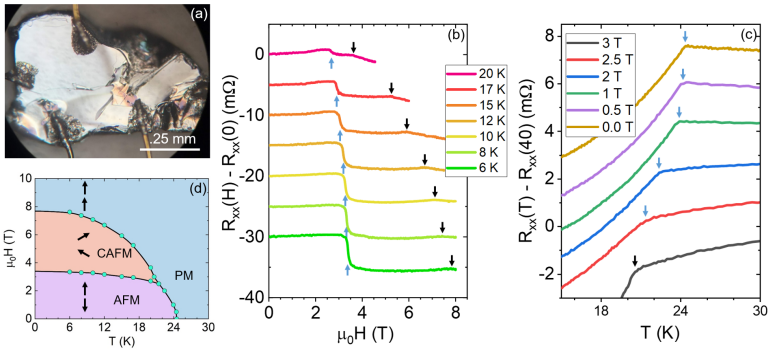

Figure 3.3: (a) Optical image of $MnBi_2 2Te_4$ single crystal with Au leads for Hall transport. (b,c) Longitudinal resistance versus applied field and temperature used to complete the H-T phase diagram (d). The small blue (black) arrows indicate AFM to PM (paramagnetic) or AFM to CAFM (canted AFM) (CAFM to PM) transition. The current used for transport was 4 mA at 314 Hz.

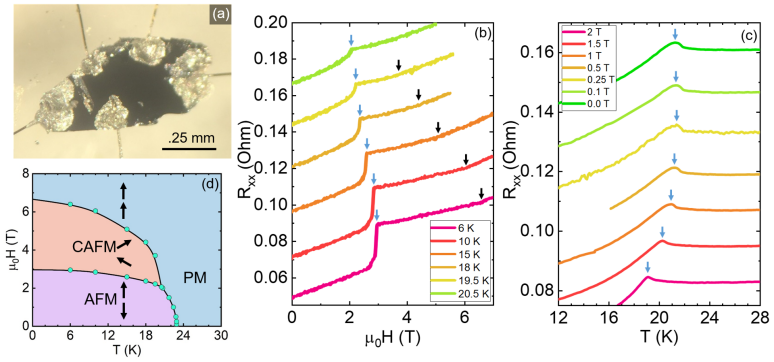

Figure 3.4: (a) Optical image of $MnBi_{1.37}Sb_{0.63}Te_4$ single crystal. (b,c) Longitudinal resistance versus applied field and temperature used to complete the H-T phase diagram (d). The small blue (black) arrows indicate AFM to PM or AFM to CAFM (CAFM to PM) transition. The current used for transport was 200 μA.

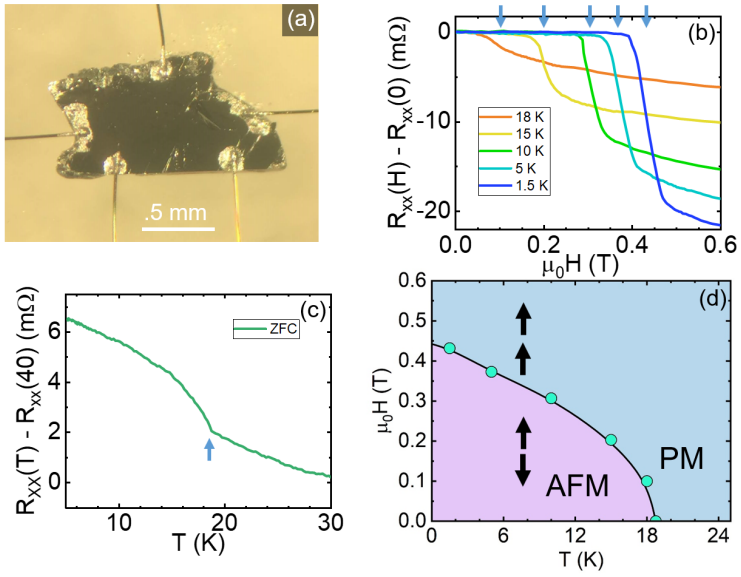

Figure 3.5: (a) Optical image of $MnSb_2Te_4$ single crystal with Au wires for in-situ transport measurements. (b,c) Longitudinal resistance versus applied field and temperature used to complete the H-T phase diagram (d). The blue arrows indicate AFM transition. The current used for transport measurement was 100 μA.

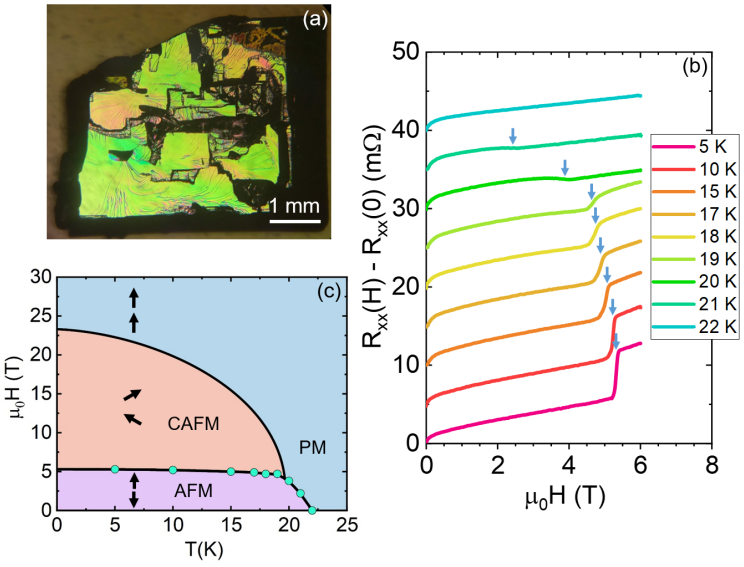

Figure 3.6: (a) Optical image of as-grown $EuMnBi_2$ single crystal (transport leads not shown). (b) Longitudinal resistance versus applied field and temperature used to complete the H-T phase diagram (d). The small blue arrows indicate AFM to CAFM or AFM to PM transition. The current used for transport was 100 μA.

All four compounds are AFM with uniaxial A-type AFM order, *i.e.*, alternating ferromagnetic Mn order in SLs in $MnBi_{2-x}Sb_xTe_4$[139] (Fig. 3.2(a)), or double alternating (up-up-down-down) ferromagnetic Eu order[83] (Fig. 3.2(b)), although the former is also a possible configuration in $EuMnBi_2$. Our MFM images reveal that DWs of A-type AFM order emerge below the Néel ordering temperature (T_N ∼19-24 K) in all four topological AFMs. Field dependence of DW signals suggest that the magnetic contrast of DWs comes from the enhanced susceptibility or net magnetization inside DWs. This is caused by the winding of the AFM order parameter across a DW, resulting in a spin-flop or spin-flip state inside the DW[133]. This contrast mechanism might be generalized to imaging DWs in other AFMs with uniaxial anisotropy. The domain configuration is randomized after a thermal cycle to $T > T_N$ or a field cycle to the saturated state, indicating random nucleation and weak pinning.

For an A-type AFM with uniaxial anisotropy, there are only two possible domain states, up-down-up-down (↑↓↑↓) and down-up-down-up (↓↑↓↑)[140], or in the case of $EuMnBi_2$, up-up-down-down (↑↑↓↓) and down-down-up (↓↓↑↑). They are related to each other by either TRS or a fractional lattice translation, so they are antiphase domains and the AFM DWs separating them are antiphase boundaries. Therefore, there will not be any vertex point connected to three or more DWs. Indeed, this is what we observed in all four AFMs. As shown in Fig. 3.7, curvilinear features with dark contrast emerge only below T_N. These features are either continuous or forming loops without any vertex point or preferred orientation, which is consistent with there being only two antiphase domain states in these systems. Thus, we conclude that these curvilinear features are antiphase AFM DWs. The observation of DWs in these two uniaxial AFMs with very different crystal structure and magnetic couplings suggest that magnetic imaging of AFM DWs can be generalized to other functional uniaxial AFMs.

The AFM DWs in $EuMnBi_2$ show dark contrast at low temperature and finite field, indicating that they carry finite magnetic moments parallel to the MFM tip moment. For

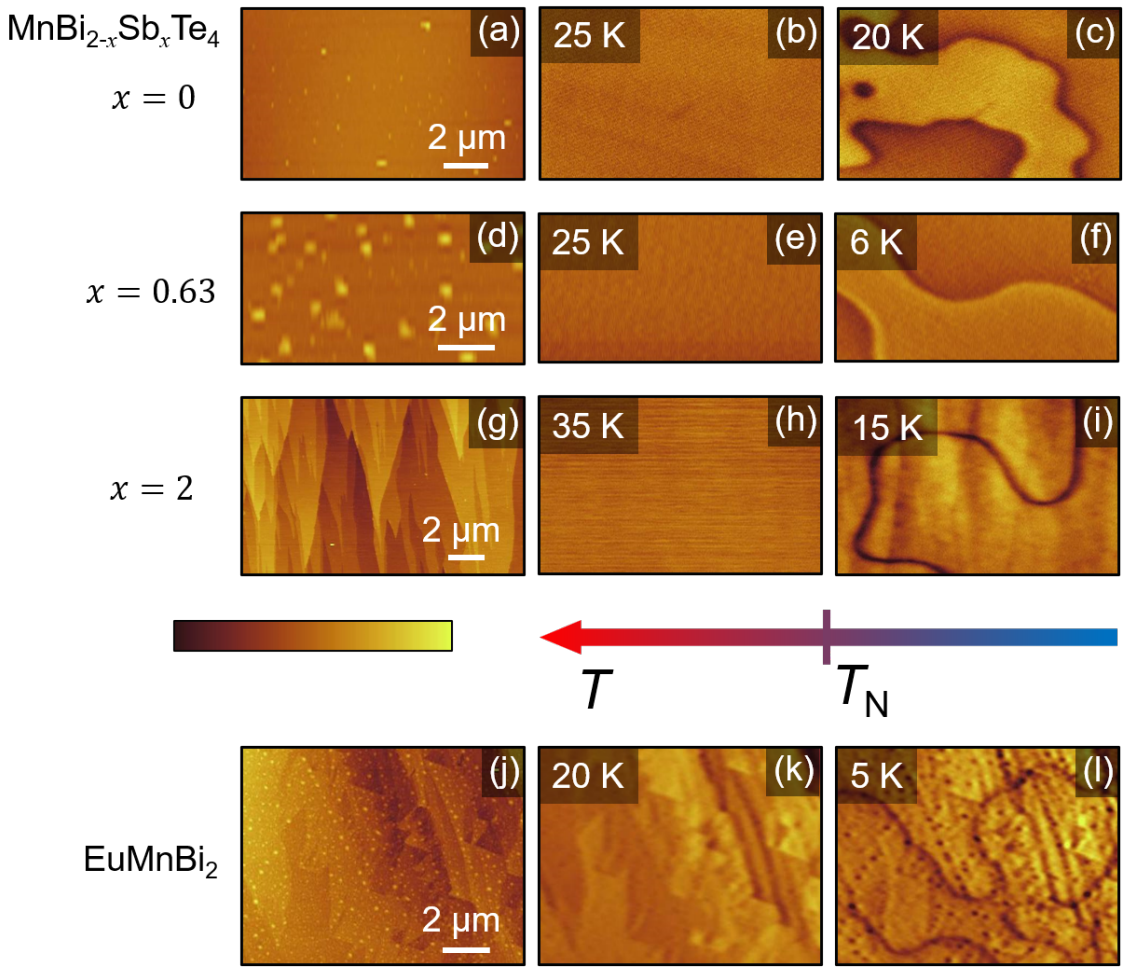

Figure 3.7: (a,d,g,j) Topographic images of $MnBi_{2-x}Sb_xTe_4$ singe crystals ($x = 0,\ 0.63,\ 2$) and $EuMnBi_2$. The color scales are: 25, 50, 15 and 40 nm, respectively. (b,e,h,k) MFM images taken above T_N. No domain walls (DW) are visible. (c,f,i,l) MFM images taken below the Néel ordering temperatures (T_N). The color scales are: 0.15, 0.3, 0.2 and 1.0 Hz, respectively. $T_N = 24$, 23, 19 K and 22 K for $x = 0$, 0.63, 2, and $EuMnBi_2$, respectively.

$MnBi_{1.37}Sb_{0.63}Te_4$ and $MnBi_2Te_4$, additional weak domain contrast between two AFM domain states was observed at low field likely due to imperfect compensation of alternating ferromagnetic layers near the surface (see chapter 4 for more detail). Such domain contrast was reported previously in synthetic AFMs (effectively A-type order)[141, 142]. Weaker domain contrast was also observed in $MnSb_2Te_4$ at low temperature, shown in Fig. 3.8, presumably due to a much smaller saturation moment (∼1.5 μ_B/Mn) of $MnSb_2Te_4$ than that of $MnBi_2Te_4$ and $MnBi_{1.37}Sb_{0.63}Te_4$ (∼3.2-3.5 μ_B/Mn)[139].

Figure 3.8: Topography and MFM images at 15 K and 6 K of $MnSb_2Te_4$, respectively. The 6 K MFM image shows clear domain contrast in addition to DW signal. The color scale for the topography and MFM images are 15 nm and 0.2 Hz.

No domain contrast was observed in $EuMnBi_2$ at any field, possibly due to the rougher surface morphology. The domain contrast in all three compounds gradually diminishes with increasing magnetic field, possibly due to surface relaxation of antiferromagnetism which will be discussed in detail in chapter 5.

The metamagnetic transition is of the spin-flip type (H_{SF} ∼0.3 T) in $MnSb_2Te_4$, suggesting the interlayer AFM exchange coupling is much weaker than anisotropy energy[139], which is similar to that in synthetic AFMs widely used in spintronics[124, 125, 143], indicating possibly similar DW structure. However, such DWs with net moment have not been reported in natural A-type AFMs[144]. We note that AFM DWs with net moment have been visualized in the multiferroic domain boundaries of Z_6 vortex domains in hexagonal manganites, where Mn spins form 120° spin order[145] and AFM DWs are pinned to the structural antiphase-ferroelectric DWs because of cross-coupling[146].

In contrast to $MnSb_2Te_4$, the metamagnetic transition (H_{SF} ~3-3.5 T) of $MnBi_{1.37}Sb_{0.63}Te_4$ and $MnBi_2Te_4$ is a spin-flop one, *i.e.* from the A-type AFM state to the canted AFM (CAFM) state[139]. This suggests a significantly stronger interlayer AFM exchange coupling [139]. The spin-flop transition is followed by a saturation transition (H_S~7-8 T) from the CAFM state to the forced ferromagnetic state (*i.e.* paramagnetic state in zero field)[83, 139]. Therefore, it is of fundamental interest to explore the evolution of antiphase AFM DWs in these systems in high magnetic field. As shown in Fig. 3.9(a-g), the DW contrast of $MnBi_{1.37}Sb_{0.63}Te_4$ is substantially enhanced in finite magnetic fields.

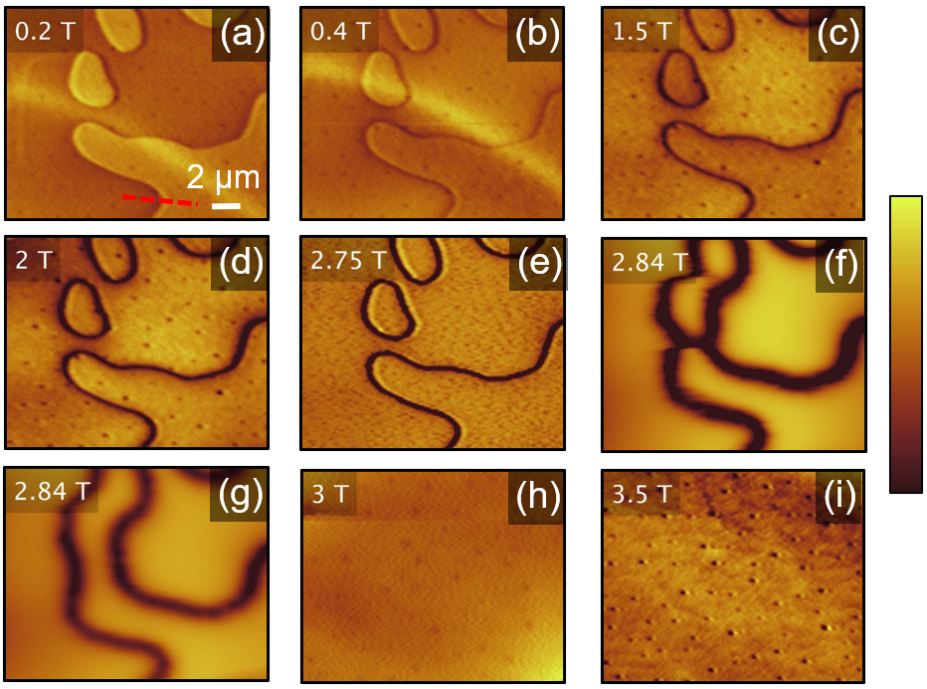

Figure 3.9: (a-i) MFM images taken at 6 K after 0.5 T FC on the same location of $MnBi_{1.37}Sb_{0.63}Te_4$ with increasing magnetic fields (labeled on upper left corner). Panel (f) and (g) show the coalescence of AFM domains. (i) MFM image (3.5 T) of the canted AFM state. The color scales are 0.3 (a-d), 2 (e-g) and 0.3 Hz (h, i).

Note, the "shadowing" effect seen in Fig. 3.9(e) is due to insufficient feedback of the tip so there is a little bit of overshoot (See chapter 2). Because the AFM order must rotate away from its easy axis inside the DW, the spins of the antiphase DWs in $MnBi_{1.37}Sb_{0.63}Te_4$ are

likely in the CAFM state as illustrated in cartoon in Fig. 3.10(a). Thus, the line profile of the DW from Fig. 3.9(c) appears attractive at the DW, because the magnetic susceptibility of the DW (χ_{CA}) is larger than that of domains (χ_{AA}). Line profiles of the DW along the red dotted line in Fig. 3.9(a) are shown in Fig. 3.10(b). The line profiles at low-field appear more dipole-like, whereas the lines profiles at higher field appear more monopole like[141, 144]. This is due to the DW canting from in-plane to out-of-plane. The induced canted moments of DWs in high magnetic field can be visualized by MFM, *i.e.*, susceptibility contrast mechanism[147].

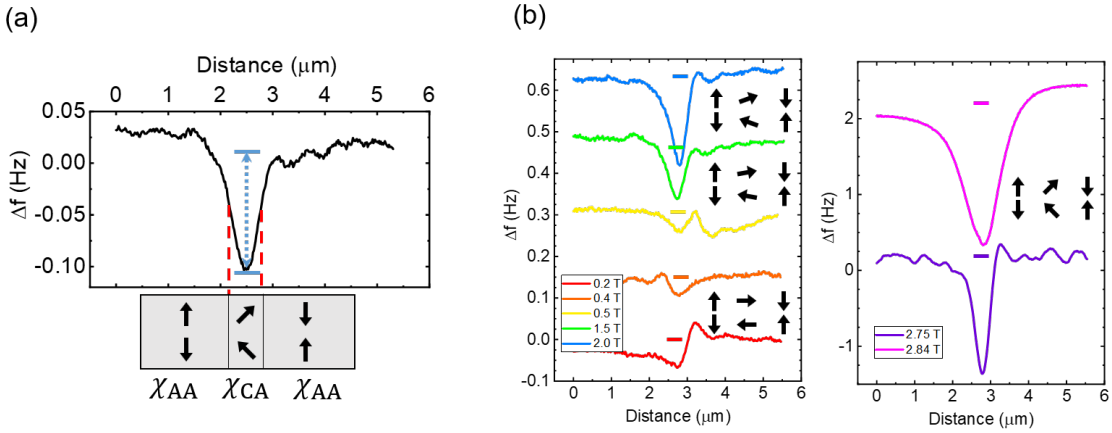

Figure 3.10: (a) Line profile of DW from Fig. 3.9(c) (1.5 T) and schematic of spin structure of DW. The DW contrast (indicated by blue dash arrow) comes from the susceptibility difference between domains (χ_{AA}) and DW (χ_{CA}). (b) Line profiles of the DW along the red dotted line in Fig. 3.9(a) at different magnetic fields showing a significant enhancement of DW contrast. The short colored-lines in the middle of the DWs indicate the baseline of the DW contrast. The baseline at low field (< 1.5 T) is midway between peak and trough, since the domain contrast skews the baseline level. The DW moments (black arrows) are displayed to show how they evolve with applied field, leading to a stronger DW moment.

Indeed, the DW contrast of $MnBi_{1.37}Sb_{0.63}Te_4$ increases linearly with increasing magnetic field below 2 T, then rises sharply right before the spin-flop transition as shown in Figs. 3.11(a) and 3.11(c). The blue curve in 3.11(a) is the DW contrast extracted using histograms of the MFM images (an example is shown in 3.11(b)). The curve matches well to the DW contrast extracted using line profiles, suggesting that the DW contrast is uniform

and not to dependent on where the line profile is taken from.

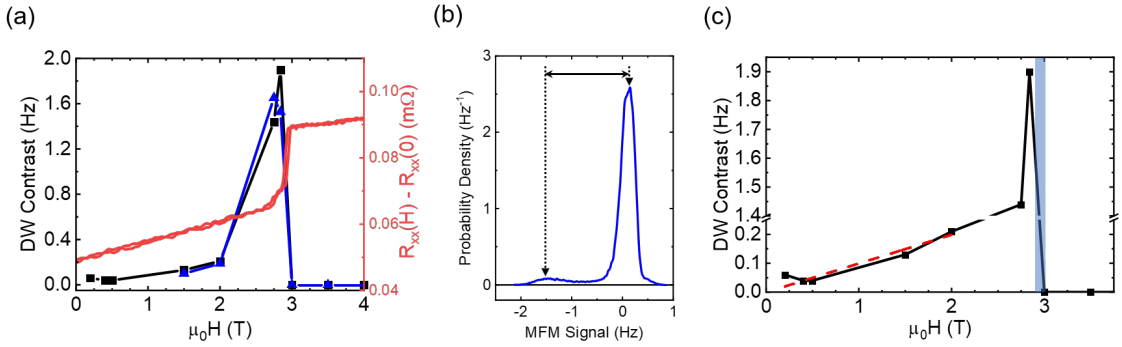

Figure 3.11: (a) H-dependence of DW contrast (black) and longitudinal resistance (red) of $MnBi_{1.37}Sb_{0.63}Te_4$ at 6 K. The blue curve is the DW contrast extracted using a histogram of the MFM image (an example is shown in (b)). It matches well to the DW contrast extracted using line profiles, suggesting that the DW contrast is uniform. (c) H-dependence of DW contrast in (a) with scale enhanced and linear fit to low-field data (red dashed-line. It is approximately linear for $H < 2$ T, suggesting a susceptibility mechanism.

More detailed cartoons of the DW spin-texture at high-fields are shown in Fig. 3.12. The black spin configuration (0.0 T) has a DW in the spin-flop state, leading to a line profile that is more skewed. The blue and red spin configurations (2.0 and 2.7 T) however, have a DW with a net out-of-plane moment.

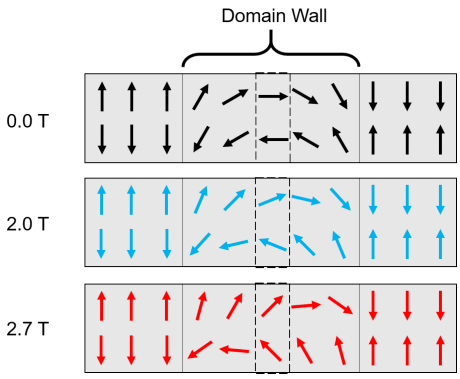

Figure 3.12: Spin configurations of domains and domain walls for the first three line profiles in Fig. 3.13(u).

This is due to the out-of-plane applied field staggering the parallel and anti-parallel

moments, i.e. the anti-parallel moments are more easily rotated than the parallel moments. This leads to a stronger net moment in the DW and thus a stronger DW contrast and could also explain why the DW appears wider at higher field. Such wall structure has been visualized by SP-STM[133].

The same DW behavior is also observed in $MnBi_2Te_4$, shown in Fig. 3.13. The DW contrast increases approximately linearly with field up to 2 T, then rises quickly above 2 T up to the spin-flop transition (∼2.87 T), then plummets down sharply at the transition. Above the spin-flop transition, the DW contrast decreases slowly in the CAFM state until the saturation transition at ∼4.7 T, then disappears in the saturation state. This behavior above the spin-flop transition, is discussed in more detail in the last section.

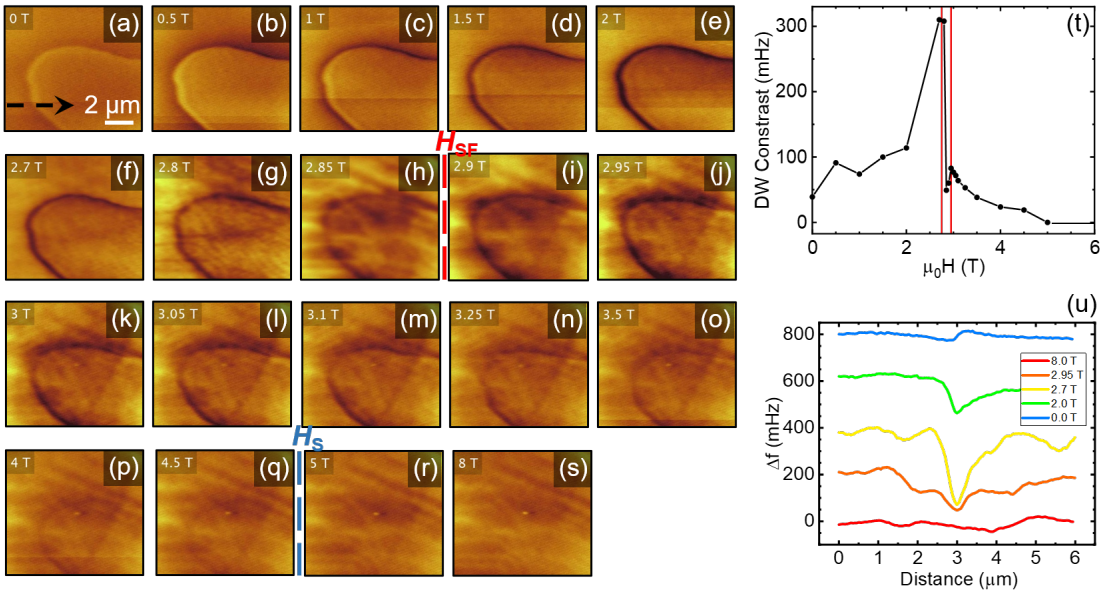

Figure 3.13: (a-s) Complete H-dependence of MFM images at 18 K on $MnBi_2Te_4$ single crystal. The line profile (black dotted arrow) is used for DW contrast analysis. (t) H-dependence of DW contrast (black) (18 K) vs applied field on $MnBi_2Te_4$ single crystal. (u) Line profiles of the domain wall along the black dotted line in (a) at different magnetic fields showing a significant enhancement of domain wall contrast. The color scales for the MFM images are 0.3 (a-e), 1 (f-h), 0.5 (i) and 0.3 Hz (j-s).

A similar increase in DW contrast was observed in the spin-flip system $MnSb_2Te_4$,

shown in Fig. 3.14. The observed DWs get weaker and fuzzier above 0.2 T, probably due to interaction with the stray field of the MFM tip. The DWs become unrecognizable as the magnetic field approaches the spin-flip transition (∼0.35 T), as shown in Figs. 3.14(h,i). No DWs are observed above the spin-flip transition at 0.4 T. This is in contrast to $MnBi_2Te_4$ and $MnBi_{1.37}Sb_{0.63}Te_4$. The contrast of the DWs, shown in Fig. 3.14(k) increases up to 0.2 T, then decreases and becomes unmeasurable above 0.3 T. The onset of the spin-flip transition is ∼0.35 T, which completes at ∼0.4 T.

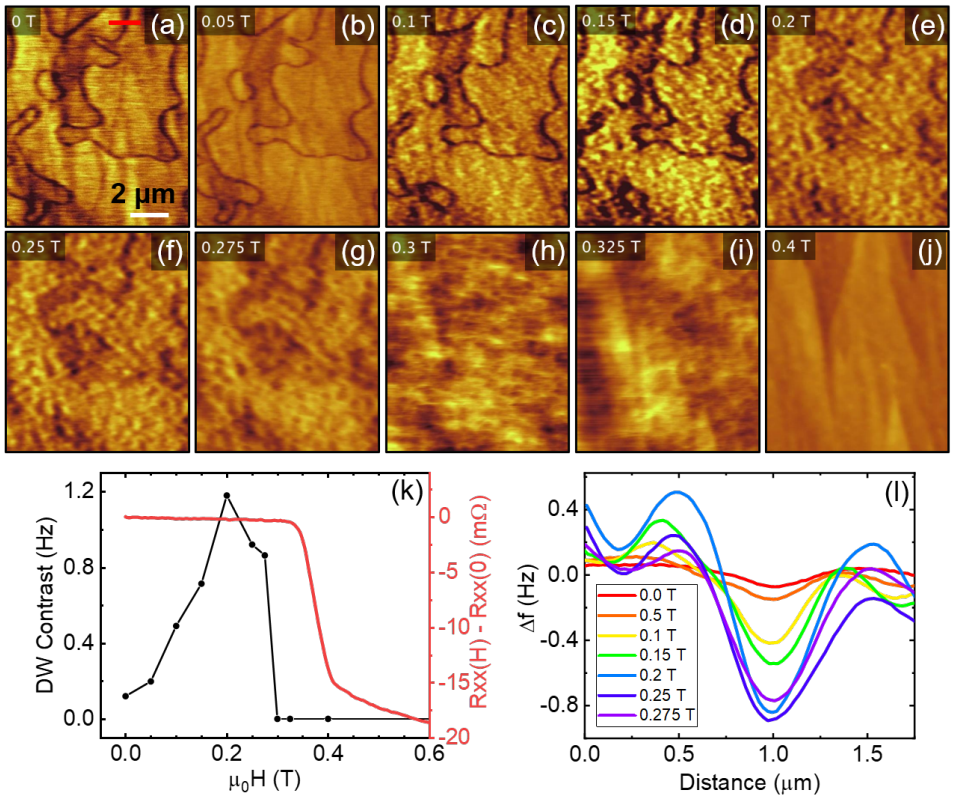

Figure 3.14: (a-j) Complete H-dependence MFM images of $MnSb_2Te_4$ at 5 K. DW contrast was measured on red line shown in (a). (k) H-dependence of DW contrast (black) and longitudinal resistance (red) on $MnSb_2Te_4$ single crystal. The color scales for the MFM images are 0.2 (a), 1 (b-d) and 3 Hz (e-j). (l) Line profiles of the domain wall along the red line in (a) at different magnetic fields showing a significant enhancement of domain wall contrast.

The Dirac semimetal $EuMnBi_2$ also showed similar increasing DW contrast behavior, shown in Figs. 3.15 and 3.16. Fig. 3.15 shows MFM images taken on the same location as

Fig. 3.7(l) with increasing magnetic field showing increasing contrast of a curvilinear DW. The highest DW contrast is right before the spin-flop transition around 5.2 T, above which there is no DW contrast in view.

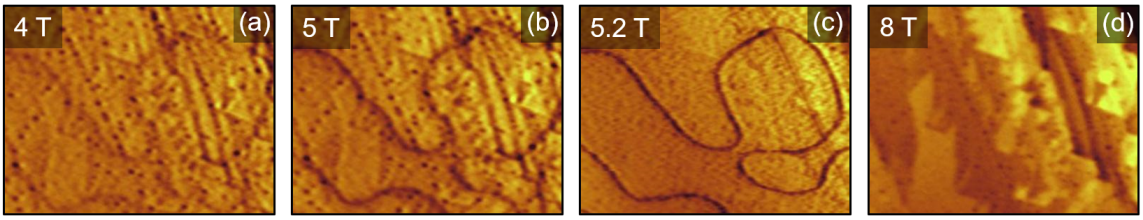

Figure 3.15: (a-d) MFM images taken with increasing magnetic field (labelled in the upper right corner) on as-grown $EuMnBi_2$ single crystal showing increasing contrast of curvilinear DW. The color scales for the MFM images are 1, 1, 4, 2 Hz, respectively.

Similarly, Fig. 3.16 shows MFM images taken after 50 mT FC on the same location with increasing magnetic fields, starting at zero-field, showing increasing contrast of curvilinear DWs. The H-dependence of DW contrast extracted from red dotted line in Fig. 3.16(g) is plotted in Fig. 3.16(i). The DW contrast increases up to the spin-flop transition, then disappears. Line profiles of the DW are shown in Fig. 3.16(j) at different magnetic fields. A similar linear increase at low-field is observed followed by a significant enhancement of DW contrast.

These results confirm that it is possible to visualize AFM DWs in high magnetic field using the susceptibility contrast between the A-type AFM (χ_{AA}) and the CAFM (χ_{CA}) states[139]. Note that the DW contrast in $MnSb_2Te_4$ is also enhanced in finite magnetic field, indicating substantial contribution from susceptibility mechanism. Therefore this mechanism extends to both spin-flop and spin-flip type systems.

The observed DW width in the $MnBi_2Te_4$ family is ~300-500 nm, which is much larger than the estimated values ($\lesssim$ 10 nm) from exchange and anisotropy energy[139]. Here we use the formula for ferromagnetic DW width $\delta = \pi a\sqrt{\frac{A}{K}}$ to estimate the width of A-type AFM DW widths. Here A is the exchange stiffness energy constant, K is the anisotropy

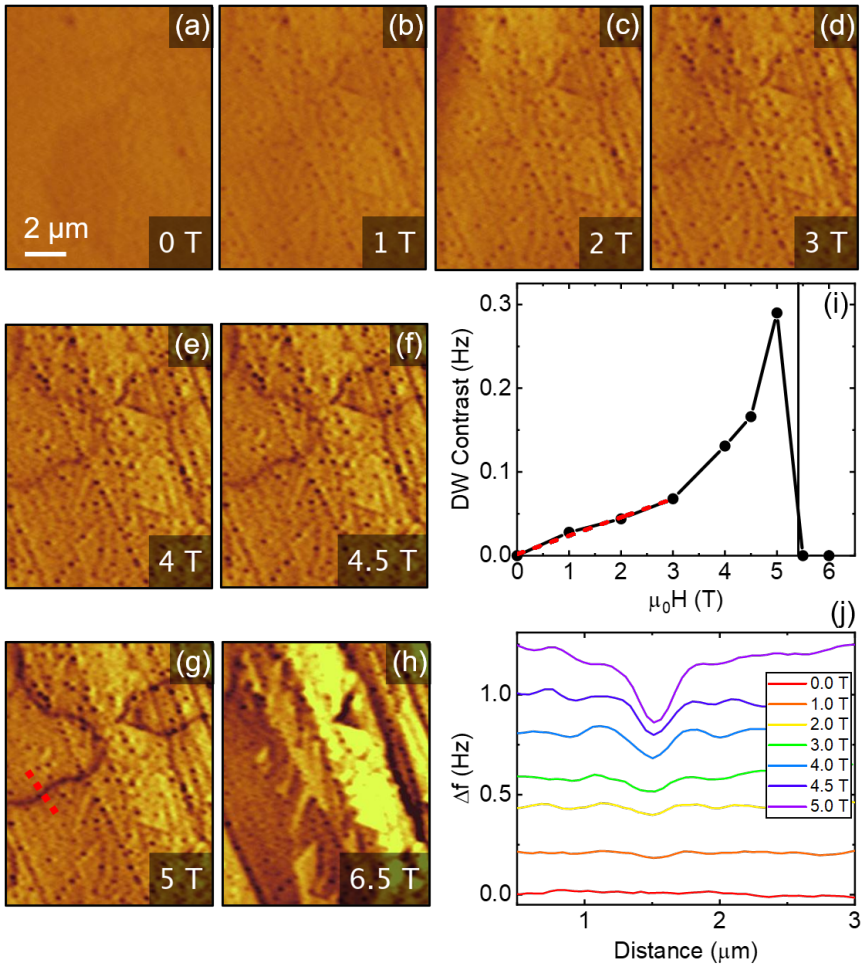

Figure 3.16: (a-h) MFM images taken after 50 mT FC on the same location with increasing magnetic fields (labelled in the lower right corner) showing increasing contrast of curvilinear DWs. (i) H-dependence of DW contrast on $EuMnBi_2$ single crystal extracted from red dotted line in (g). The DW contrast increases up to the spin-flop transition, labeled by black vertical line, then disappears above the transition. (l) Line profiles of the domain wall along the red dotted line in (g) at different magnetic fields showing a significant enhancement of domain wall contrast. The color scale for the MFM images 1 Hz.

energy, and a is the lattice constant ($\approx$ 0.43 nm). A can be estimated from the ordering temperature T_N, $A \approx k_B T_N$. K can be estimated from the Zeeman energy at the spin-flop (spin-flip) transition, $K \approx M_{SF} H_{SF}/2$, because it is approximately the energy gain to overcome the anisotropy energy. Here M_{SF} is the magnetization value just above the spin-flop or spin-flip transition, and H_{SF} is the spin-flop or spin-flip transition field. The estimated domain wall widths are listed in Table 3.1.

Crystal	T_N	H_{SF}	M_{SF}	δ
$MnBi_2Te_4$	24 K	3.6 T	1.5 μ_B/Mn	5 nm
$MnBi_{1.37}Sb_{0.63}Te_4$	23 K	3.0 T	1.3 μ_B/Mn	6 nm
$MnSb_2Te_4$	19 K	0.4 T	1.5 μ_B/Mn	13 nm
$EuMnBi_2$	22 K	5.4 T	1.5 μ_B/Eu	4 nm

Table 3.1: The estimated DW widths of 4 – 13 nm are much different than the measured DW widths of ∼500 nm. This is probably due to a combination of the diameter of the tip (100 – 200 nm) and the tip-sample distance ∼50 – 100 nm. Therefore, the widths of the DWs are likely resolution limited.

The DW width could be broadened in high magnetic field because of Zeeman energy gain. The sharp rise of DW contrast near the spin-flop transition indicates an increase of DW width, *i.e.,* the volume of CAFM state (Fig. 3.9(f)). The observed width could be further broadened by other factors such as bending of DWs underneath the surface, the effective size of MFM tip, and the effective lift height. The DWs in $MnBi_{1.37}Sb_{0.63}Te_4$ disappear above the spin-flop transition (Fig. 3.9(i)), suggesting a single domain state within the field of view. In the CAFM state, one expects three additional orientation variants (besides the two antiphase variants) due to trigonal crystallographic symmetry. CAFM domains in Cr_2O_3 have been visualized by non-linear optics[148]. Thus, one would expect similar multi-domain state in the CAFM states of $MnBi_{1.37}Sb_{0.63}Te_4$. The observed single (large) domain state indicates very few nucleation sites for CAFM domain states in $MnBi_{1.37}Sb_{0.63}Te_4$.

3.3 Cooling Field Dependence, Domain Renucleation, Annihilation and Creep

Because DW energy is proportional to the geometric mean of exchange and anisotropic energies, the larger anisotropy of $MnBi_{1.37}Sb_{0.63}Te_4$ and $MnBi_2Te_4$ suggests an enhanced DW energy, thus favoring lower DW density. On the other hand, the Zeeman energy gain in high magnetic field lowers the DW energy, thus favoring higher DW density. Although AFM domains are insensitive to magnetic field because of cancellation of magnetization, DWs with significant net moment or higher magnetic susceptibility would be energetically more favorable in high magnetic field. Indeed, this simple scenario is confirmed by our MFM results. As shown in Fig. 3.17, higher DW density was observed after field cooling through T_N values in all three $MnBi_{2-x}Sb_xTe_4$ samples, consistent with the simple energetics consideration.

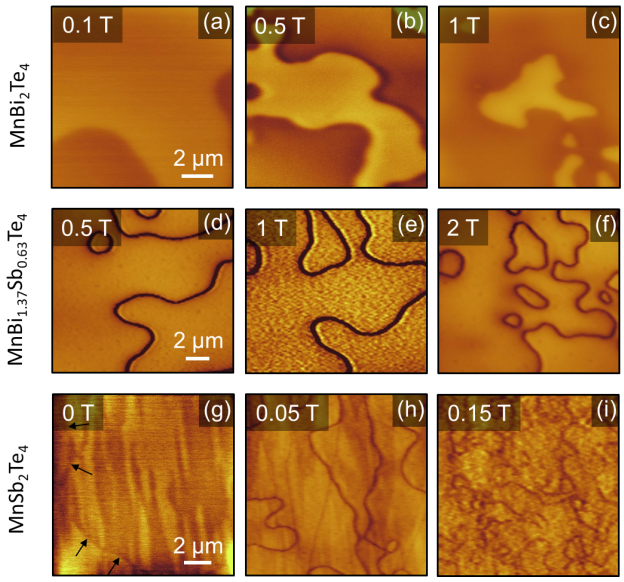

Figure 3.17: (a-c) MFM images at 5 K of $MnBi_2Te_4$ after 0.1, 0.5 and 1.0 T field cooling. (d-f) MFM images at 6 K of $MnBi_{1.37}Sb_{0.63}Te_4$ after 0.5, 1.0 and 2.0 T field cooling. (g-i) MFM images at 5 K of $MnSb_2Te_4$ after 0, 0.05 and 0.15 T field cooling. The arrows in panel (g) indicate the location of a DW. Cooling through T_N with higher field induces more AFM DWs. The color scales are 0.5, 1.8 Hz for (a-c) and (d-f), respectively, and 0.2, 1, and 3 Hz for (g-i).

Interestingly, a new multi-domain state (size ~10 μm) with DWs reemerges in the CAFM state (Fig. 3.18(c,g)) after reducing magnetic field from 8 T. Here, the two variants of AFM domains are labelled by **a** and **b**. Further reducing magnetic field through the spin-flop transition to zero-field causes creep (indicated by solid red arrows) and annihilation (indicated by dotted red arrows) of DWs. At 0 T, the two DWs partially annihilate with each other, resulting in a different AFM domain pattern. The DW annihilation confirms that there are only two variants of AFM states above the spin-flop transition within the field of view.

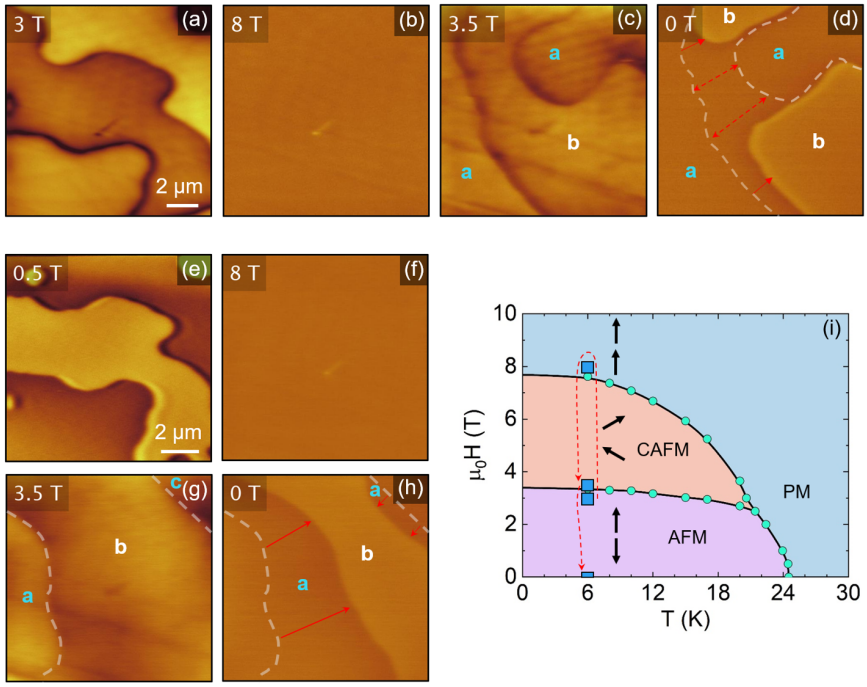

Figure 3.18: (a-d) and (e-h) Separate field cyclings on $MnBi_2Te_4$. (a,e) AFM domain pattern on the upward ramping. (b,f) Saturation state at 8 T. (c,g) At 3.5 T, on downward ramping, a different AFM domain pattern nucleates upon reentry into CAFM state. Two different AFM phases are labelled *a* and *b*. (d, h) At 0 T, DWs creep and partially annihilate across H_{SF}. The white dashed lines in (k) denote the DW locations at 3.5 T. The red dotted arrows indicate the partial annihilation of DWs, and the solid red arrows indicate the creep of DWs. (i) *H*-*T* phase diagram. The blue squares and red dotted arrows show the field values and order of MFM images. The color scale for the MFM images is 1 Hz (a-d) and 0.5 Hz (e-h).

Creep and annihilation were also observed in $MnSb_2Te_4$ and $MnBi_{2-x}Sb_xTe_4$, as shown

in Figs. 3.19 and 3.20. Fig. 3.19 shows MFM images of a field cycle at 5 K taken at the same location after a 0.15 T field-cooling. The cyan circles in Figs. 3.19(a,b) indicate creeps of DWs after applying 0.1 T. In $MnBi_{1.37}Sb_{0.63}Te_4$, the domain configuration is stable until 2.75 T. At 2.84 T, the DWs interact strongly with MFM tip stray field so that some domains merged (with DW annihilation), as shown in Fig. 3.20(b). The strong interaction also results in broadened and fuzzy DWs.

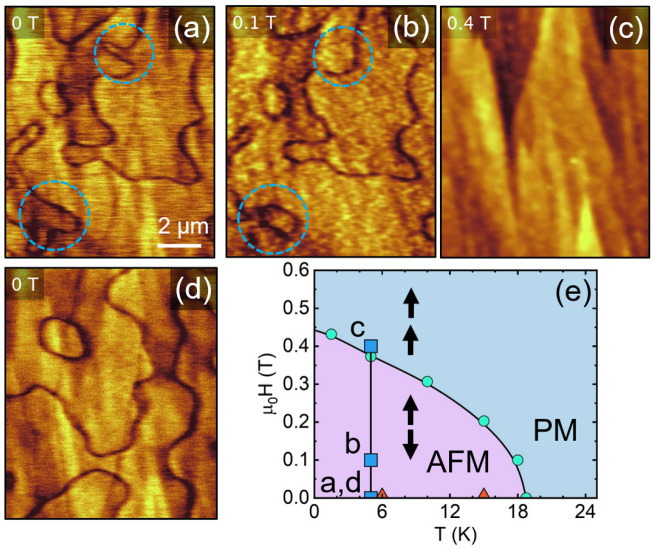

Figure 3.19: (a-d) MFM images of field cycle (5 K) taken at the same location after 0.15 T FC of $MnSb_2Te_4$. The color scale is 1 and 0.3 Hz for (b,c) and (a,d). Cyan circles indicate creeps of DWs after applying 0.1 T. (e) Magnetic phase diagram showing the spin-flip transition from the A-type AFM state to saturation state indicated by black arrows. Blue squares show the fields at which the images (a-d) are taken.

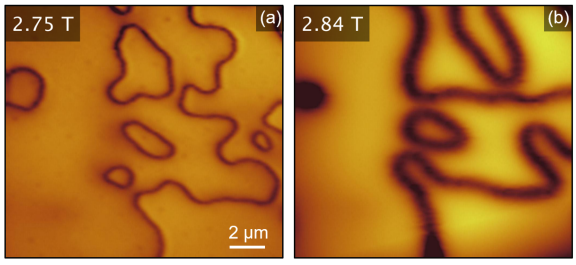

Figure 3.20: (a,b) MFM images at 6 K after 2 T field cooling of $MnBi_{1.37}Sb_{0.63}Te_4$ showing domain coalescence. The color scale for the MFM images is 1.8 Hz.

3.4 Survival of AFM Domain Walls Above Spin-flop Transition in $MnBi_2Te_4$

In contrast to those in $MnSb_2Te_4$ and $MnBi_{1.37}Sb_{0.63}Te_4$, the DWs in $MnBi_2Te_4$ survive above the spin-flop transition (H_{SF}), then disappear above the saturation transition (H_S). Fig. 3.21(a-h) show representative MFM images taken with upward ramping of magnetic field at 18 K (H_{SF} ~2.87 T and H_S ~4.7 T).

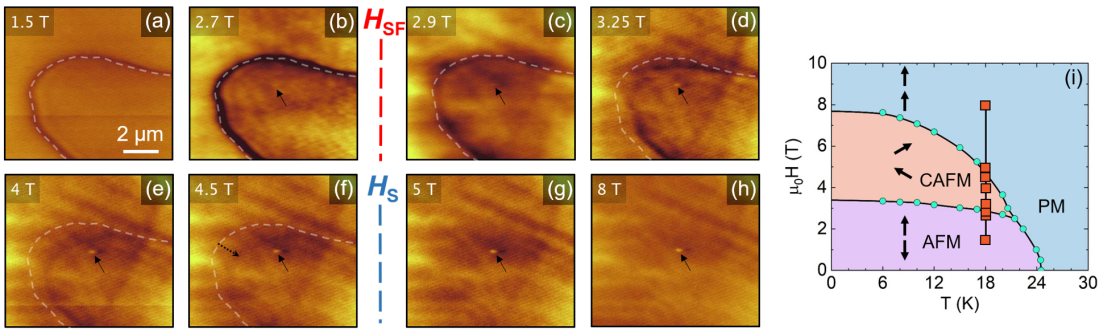

Figure 3.21: (a-h) MFM images from Fig. 3.13 illustrating a robust AFM DW. The color scales are 0.5 and 0.2 Hz for (a-c) and (d-h), respectively. The H values are labelled with orange squares in the H-T phase diagram in panel (**l**). The H_{SF} and H_S represent the spin-flop and saturation transitions, respectively. A white dotted line outlines the DW observed at 1.5 T. The small solid black arrows note a topographic feature used for alignment. (l) H-T phase diagram.

The DW creeps a bit with increasing magnetic field, again indicating very weak pinning. The persistence of antiphase DWs across the spin-flop transition indicates a coherent rotation of all spins, including those in DWs. The coherent rotation of spins is probably induced by a small in-plane magnetic field component due to a slight sample tilt ($\sim 5°$), which breaks the three-fold in-plane symmetry. Yet, the persistence of DWs in the CAFM state is perplexing because there is no obvious symmetry or other constraint to enforce coherent spin rotation inside the DWs. Such behavior might be explained if the exact spin structure of the DWs and its evolution across the spin-flop transition is resolved, *e.g.,* by sp-STM[110], which is beyond the scope of this work. No DW is observed above the saturation transition, consistent with the saturation state where all spins are aligned with magnetic

field (Fig. 3.21(h)).

3.5 Conclusion

Our results demonstrate that DWs of A-type AFM order in $MnSb_2Te_4$, $MnBi_{1.37}Sb_{0.63}Te_4$, and $MnBi_2Te_4$ can be visualized by cryogenic MFM utilizing the susceptibility (magnetization) difference between DWs and domains[147]. This susceptibility contrast mechanism is different from the ferromagnetic core mechanism established in synthetic AFMs[144]. For DWs to be in the flop state, the only requirement is uniaxial anisotropy, which is quite general and is satisfied in many functional AFMs[123]. Recent advances in spintronics and 2D materials reveal exciting properties in uniaxial AFMs, *e.g.* spin Seebeck effect in MnF_2 heterostructures[149], giant tunneling magnetoresistance using CrI_3 flakes[150, 151], and quantum transport in the Dirac semimetal $EuMnBi_2$ and related compounds[83]. The visualization and manipulation of DWs in these materials will help to understand the fundamental mechanisms of these fascinating phenomena and their potential applications. Similarly, imaging and control of DWs in AFM TIs such as $MnBi_{2-x}Sb_xTe_4$ will facilitate the exploration of chiral edge states at the DWs[106], and the realization of a single domain state, which is necessary for an unambiguous observation of the axion insulator and QAH states[102, 105, 108]. The weakly pinned DWs observed in the $MnBi_2Te_4$ family might be manipulated by electric current via spin-transfer-torque[143, 152], which could lead to low power logic or memory devices[123, 124].

Chapter 4

Robust A-Type Order on the Surface of the Antiferromagnetic Topological Insulator $MnBi_2Te_4$

Recent progress in topological quantum materials suggest that AFMs may host interesting topological states[86]. For example, it has been proposed that an axion insulator state with topological magnetoelectric response could be realized in an AFM TI phase[98, 106], where the Z_2 topological states are protected by a combination of TRS and primitive-lattice translation. The AFM TI state adiabatically connects to a stack of quantum Hall insulators with alternating Chern numbers[126] thus providing a promising route to realizing the QAHE in a stoichiometric material. The prior observation of the QAH effect in magnetically doped TI thin films is limited to extremely low temperature because of the inherent disorder[55, 56, 60–62], though the disorder effects can be partially alleviated by material engineering[63–65].

The $MnBi_2Te_4$ family was predicted and confirmed to be an AFM TI that may host QAH and axion-insulator states in thin films with odd and even numbers of SLs (SLs) respectively[127–129, 139, 140]. Recent transport measurements on exfoliated thin flakes provide compelling evidence for these predictions[102, 105], suggesting gapped topological surface states. Additionally, previous neutron diffraction measurements confirmed an A-type AFM spin configuration with the magnetization along the c axis [140], which supports a massive surface Dirac cone if the bulk magnetic configuration remains at the surface.

On the other hand, recent high-resolution angle-resolved photoemission spectroscopy (ARPES) studies reveal gapless (or small-gap) surface states below the AFM ordering

temperature, suggesting a surface relaxation of the A-type order and/or the formation of nanometer-sized magnetic domains[153–156]. The AFM domain structure of $MnBi_2Te_4$ was revealed by imaging of DWs using MFM[137] (see chapter 3). The observed domain size is on the order of 10 μm, excluding the speculated nanometer-size domain scenario[155]. Several possible surface magnetic states were considered in order to rectify the observation of the gapless surface states, as shown in Fig. 4.1.

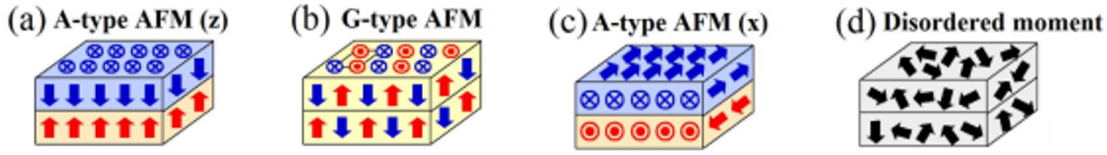

Figure 4.1: Cartoons of possible prototypical surface magnetic configurations of $MnBi_2Te_4$. (a) A-type AFM with the magnetic moments along the z axis, (b) G-type AFM, (c) A-type AFM with the magnetic moments along the x axis, and (d) disordered magnetic moments. Adapted from [154].

Thus, it is crucial to reveal the nature of surface magnetism of $MnBi_2Te_4$ in order to resolve the dichotomy between the observation of QAH transport and gapless topological surface states[102, 105, 153–156]. In this chapter, we report the observation of alternating termination-dependent magnetic signals on the surface of $MnBi_2Te_4$ single crystals using cryogenic MFM, which provides direct evidence of the persistence of uniaxial A-type AFM order all the way to the surface. Combined with the recent ARPES observations of gapless surface states, our results suggest a possible scenario of a tiny magnetic mass gap due to weak coupling between the topological electronic states and the magnetic order.

In the previous chapter we showed that in $MnBi_2Te_4$ there are only two possible domain states, $\uparrow\downarrow\uparrow\downarrow$ and $\downarrow\uparrow\downarrow\uparrow$, separated by an AFM DW. Also, that the typical domain size is $\sim$10 μm, so the tiny contribution of chiral edge states at DWs is insufficient to explain the gapless topological surface states[155]. However, it is unclear whether the A-type order persists up to the surface layer, because MFM contrast could come from sub-surface stray

fields that penetrate the surface non-magnetic layer[145]. It has been speculated that the observed gapless surface states might be explained by surface relaxation or reorientation of the A-type order[153–155]. To address these issues, we carried out MFM studies on as-grown surface of $MnBi_2Te_4$ single crystals with multiple SL steps and thin layers of surface impurity phase[157]. Prior studies suggest that the as-grown surface of $MnBi_2Te_4$ is decorated with small amounts of impurity-phase $Bi_{2-x}Mn_xTe_3$, which is a soft ferromagnet with a small coercive field (<0.04 T)[140, 158]. These magnetically soft thin layers provide an excellent opportunity to probe the screening effects of the speculated relaxed surface magnetic order with enhanced magnetic susceptibility[154].

4.1 Domain Contrast in A-type Uniaxial Antiferromagnets

In addition to the appearance of DWcontrast. Weak domain contrast between two AFM domain states was also observed at zero and finite field on a cleaved surface of $MnBi_2Te_4$, as shown in Fig. 4.2(d) and also on as-grown surfaces, shown in Fig. 4.3. This is due to an imperfect compensation of alternating ferromagnetic layers near the surface interacting with the MFM tip. Such domain contrast was reported previously in synthetic AFMs (effectively A-type order)[141, 142].

The domain contrast grows stronger at low temperature below T_N, as shown in Fig. 4.2(e), indicating that domain contrast grows with ferromagnetic layer moment size. Parallel (antiparallel) moment of the surface layer dictates the dark (bright) domain contrast, since it is closest to the MFM tip, as illustrated in Fig. 4.2(f). With this information, we can discern the AFM phase of the domains, assuming an A-type arrangement all the way up to the surface. However, it is difficult to prove that the surface is indeed A-type without observing individual layer contrast. This is where the observation of SL step edges on the surface comes in handy.

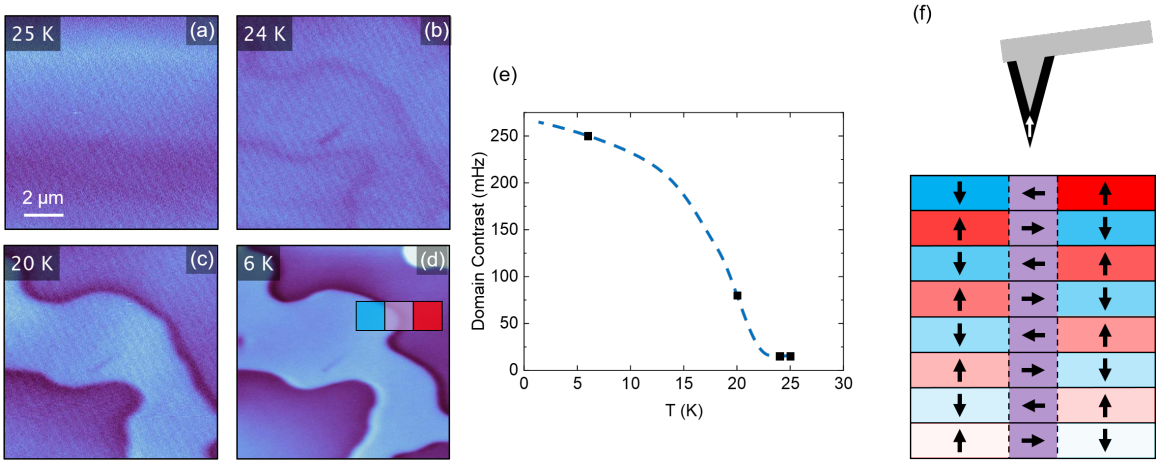

Figure 4.2: (a-c) MFM images taken at zero field with decreasing temperature (25, 24 and 20 K) on cleaved surface of $MnBi_2Te_4$. (d) MFM image of the same location taken at 5 K in 0.5 T. (e) Temperature dependence of domain contrast. The blue dotted-line is a guide to eye. (f) Cartoon of MFM tip with upward pointed moment above two AFM domains separated by DW (purple). The strength of the red and blue colors represent the strength of repulsion (blue) or attraction (red) to the tip. The ferromagnetic layers closest to the tip interact stronger and lead to bright or dark contrast, shown in colored squares in (d). The color scale for the MFM images is 0.15 Hz for (a-c), and 0.5 Hz for (d).

4.2 Septuple-Layer Step-Edge and Domain Contrast in $MnBi_2Te_4$

Figure 4.3(a) shows a typical surface morphology of $MnBi_2Te_4$ as-grown surface. There are two step edges in this location, and the observed step height (∼1.3 nm) agrees with that of a single SL. Figs. 4.3(b,c) show the MFM images taken at the same location. Note that one AFM DW cuts across the SL steps. Clearly, the magnetic contrast reverses over the DW on one terrace (green arrow) and across SLs of one single domain (red arrow) as shown in Fig. 4.3(b) and illustrated by line profiles in Figs. 4.3(d,e). Here, bright contrast indicates a repulsive interaction, i.e., surface magnetization antiparallel to the MFM tip moment, which is fixed by a small out-of-plane magnetic field[145]. The domain contrast reverses over the DW with a slight dip due to the higher susceptibility of the DW[137]. This observation is consistent with opposite surface magnetization states of different antiphase domains (Fig. 4.3(d)) or SL steps (Fig. 4.3(e)). The slight asymmetry in the line profiles

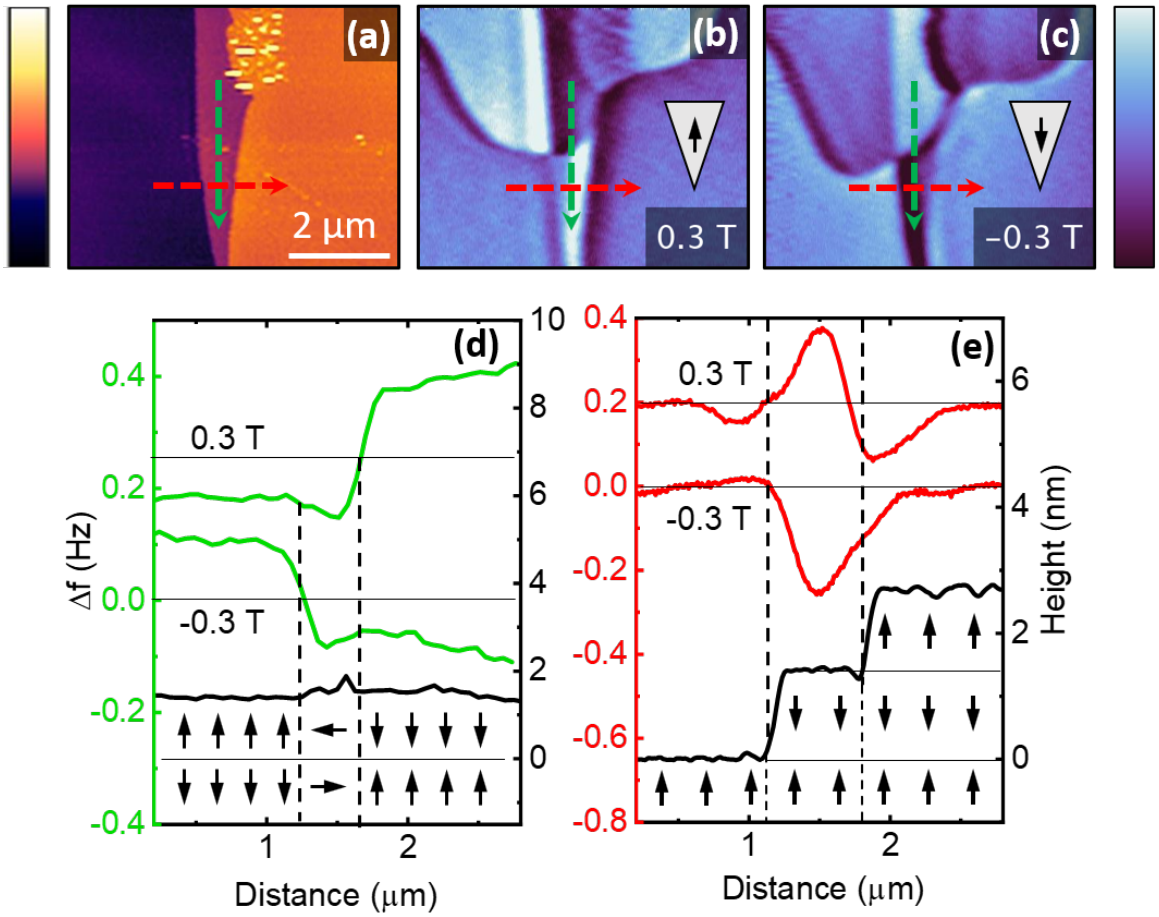

Figure 4.3: (a) Topographic image (5 K) of one and two SL (SL) steps on an as-grown $MnBi_2Te_4$ single crystal. (b,c) MFM images taken at 0.3 and -0.3 T, respectively, after field cooling at 0.6 T, at the same location as in (a). A single curvilinear domain was observed cutting through the SL step. Additionally, contrast was observed across SL steps. The domain and SL step contrast was reversed when the tip moment was flipped (dark is attractive and bright is repulsive). (d,e) Line profiles of the topography (black) and MFM (green and red) data. The frequency shift in (d) was measured across the DW over flat topography, while in (e) it was taken across the SLs. The color scale for the topographic (MFM) image(s) is 6 nm (0.3 Hz).

in Fig. 4.3(e) is due to the difference between forward and backward scanning. Figure 4.4 shows the forward and backward scanning directions giving a similar shadowing effect to that discussed in chapter 2.

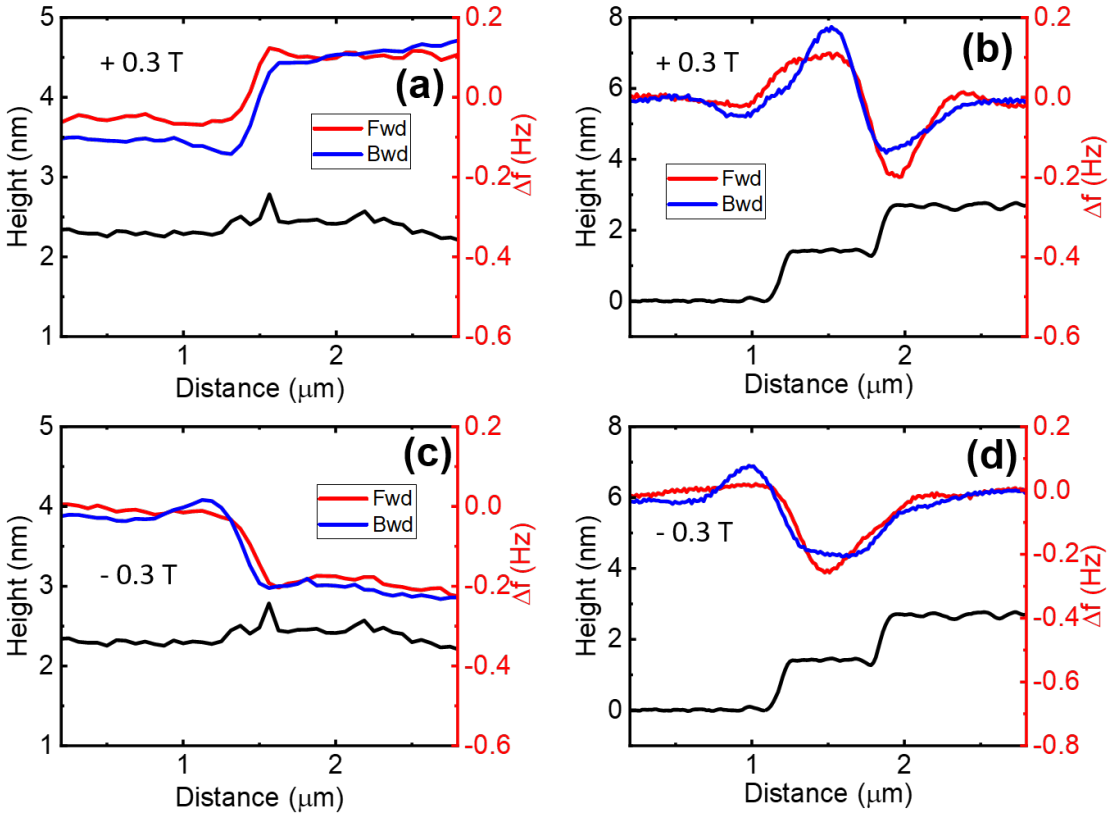

Figure 4.4: (a, b) Line profiles of topographic and MFM images from Fig. 4.3 showing both forward and backward scanning directions at +0.3 T. (c, d) Line profiles in the same location at -0.3 T. The forward and backward lines in (b) and (d) are different. The signal dips more on the right (left) side for the forward (backward) lines. This is due to the feedback of tip reacting to the abrupt change. The forward and backward lines in (a) and (c) do not differ very much.

The magnetic contrast originates from imperfect cancellation of magnetic stray field from the alternating ferromagnetic layers[141, 144]. To confirm this, we reverse the MFM tip moment using a negative magnetic field (-0.3 T). The magnetic contrast indeed reverses as shown in Fig. 4.3(c), which unambiguously demonstrates that the alternating MFM signal is from the alternating surface magnetization. Note that there is a small island of

impurity phase ($Mn_xBi_{2-x}Te_3$) with a rougher surface sitting on the upper SL step edge (Fig. 4.3(a)). It appears to screen the AFM domain contrast, as shown in Fig. 4.3(b,c). To understand the screening effect of the impurity phase, we increase the scan size to sample more impurity phases.

4.3 Screening of Magnetic Contrast by $Bi_{2-x}Mn_xTe_3$ Impurity Phase on Surface of $MnBi_2Te_4$

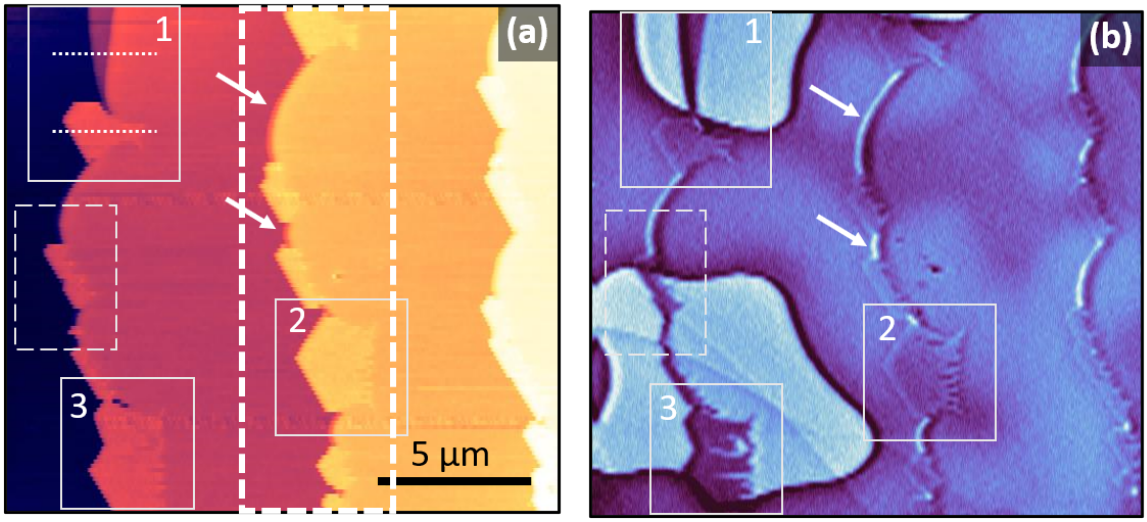

Figure 4.5: (a,b) Topographic and MFM images of as-grown $MnBi_2Te_4$ surface taken after 0.425 T field cooling and measured in 1 T field at 5 K. Magnetic contrast of domains (~10 μm) and terraces is visible. DW contrast is not suppressed by the impurity phase, as shown in the small dotted-box in (b). The color scales for the topographic and MFM images are 7 nm (0.2 Hz), respectively.

Figure 4.5(a) shows the topography of a large area with seven SL steps in the field of view (~18x13 μm^2). Most steps are paired to form curvy narrow terraces decorated with many plate-like impurity islands with partial hexagon shapes. The height of these islands (~3 nm) agrees with that of three quintuple layers (QLs) of Bi_2Te_3, which is slightly larger than that of two SLs (~2.7 nm) as shown in Fig. 4.6(a). Fig. 4.5(b) shows the MFM

image (measured at 1 T) at this location after 0.425 T field cooling. There are two bubble-like AFM domains with curvilinear DWs. Alternating magnetic contrast was observed on uncovered SL terraces across step edges or AFM DWs. However, this contrast is suppressed if the surface is covered by the impurity phases, suggesting a very effective screening of the magnetic stray field, as depicted in 4.6(b).

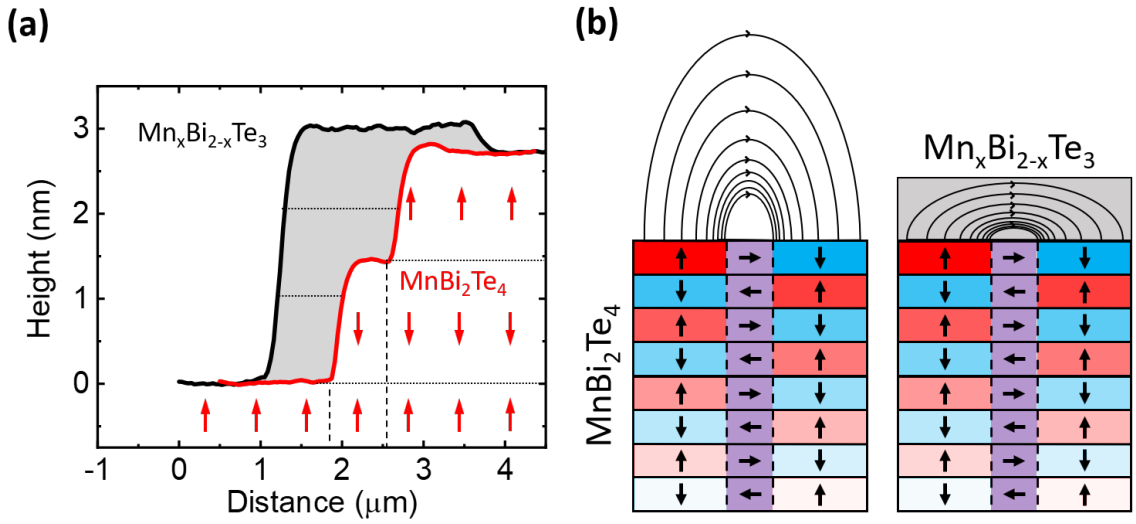

Figure 4.6: (a) Topographic line profiles (white dotted lines in Fig. 4.5(a)) of SLs and impurity phase QLs with schematic of spin configuration. The gray area illustrates a soft magnetic phase that screens the stray fields of the SL edges underneath. (b) Cartoon illustration of the screening effect of the impurity phase ($Bi_{2-x}Mn_xTe_3$). The magnetic flux lines are effectively trapped inside the impurity phase because of higher permeability.

To illustrate the details, enlargement images of a few selected areas (boxes labelled 1, 2 and 3 in Figs. 4.5(a,b)) are shown in Figs. 4.7(a-h). Arrows (dashed lines) marked the exposed (covered) narrow terraces in these images. As shown in box 3, the domain contrast can even be "blocked" by a fractional QL of the impurity phase, and clear domain contrast is visible in the holes of the impurity phase. The step edges of two SLs are easily seen above and below the $Bi_{2-x}Mn_xTe_3$ impurity phase in Figs. 4.7(a,d), indicated by white arrows. However, it is not clear from the topography if there are multiple step edges on the impurity. A differential map of the topography, shown in Figs. 4.7(b,e), shows clearly the separation

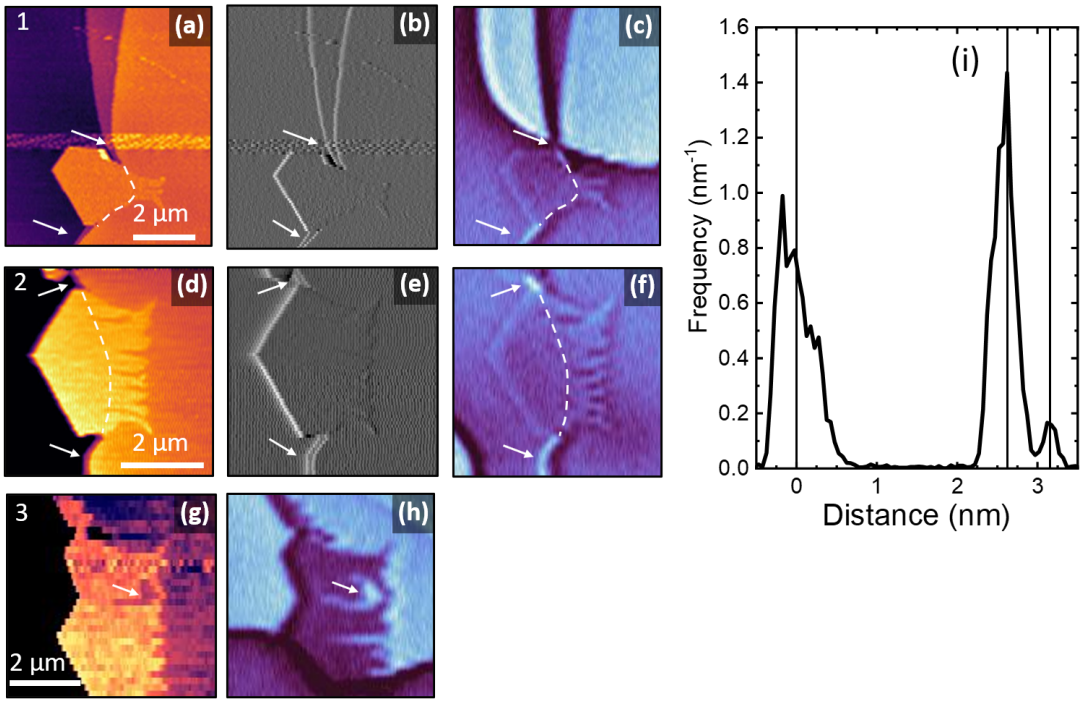

Figure 4.7: (a-h) Enlargements of topographic (a,d,g), differential (b,e) and MFM (c,f,h) images outlined by solid white boxes in Fig. 4.5. White arrows (dashed lines) mark the exposed (covered) single SL steps. The bright domain contrast in region covered by the impurity phase is suppressed, as shown by white arrow in (h). (i) Height distribution of large dotted-square area in Fig. 4.5. The two large peaks show the difference in height between the two SLs. The smaller third peak shows the height of the impurity phase. The average peak values are 2.63 and 3.15 nm, for the two SLs and impurity phase, respectively. The value of 3.15 nm is close to the height of three quintuple layers (QL) of $Bi_{2-x}Mn_xTe_3$, and 2.63 nm is close to the height of two SLs. The theoretical values are 3.06 and 2.72 nm. The color scales for the topographic and MFM images are 6, 3 and 3 nm (0.2 Hz), respectively.

of the SL step edges, but shows no such separation on the impurity edge. Thus, the bright contrast in Figs. 4.7(c,f) comes from a single SL. Figure 4.7(i) shows the height distribution of the large dotted-square area in Fig. 4.5. The two large peaks show the difference in height between the two SLs. The smaller third peak shows the height of the impurity phase. The average peak values are 2.63 and 3.15 nm, for the two SLs and impurity phase, respectively. The value of 3.15 nm is close to the height of three quintuple layers (QL) of $Bi_{2-x}Mn_xTe_3$, and 2.63 nm is close to the height of two SLs. The theoretical values are 3.06 and 2.72 nm, respectively. Thus, we can conclude that the magnetic impurity phase is most likely $Bi_{2-x}Mn_xTe_3$ and it effectively screens all the stray fields from the underlying $MnBi_2Te_4$ surface. Similar results are observed at higher temperature (below T_N). In contrast, AFM DW contrast is not affected by the impurity phase as shown in the small white dotted box in Fig. 4.5(b), because DWs extend into the bulk.

Because the alternating domain and terrace contrast can be easily screened by such a thin layer (0.3–3 nm) of soft magnet ($Bi_{2-x}Mn_xTe_3$), the uniaxial A-type spin order must persist to the top surface layer of $MnBi_2Te_4$. Otherwise, the termination-dependent magnetic contrast would be screened by any relaxation of surface magnetism with substantial magnetic susceptibility, such as paramagnetism, non-A-type spin order, or in-plane A-type order proposed in prior reports[153–156, 159].

4.4 Conclusion

In summary, our MFM results provide microscopic evidence of robust uniaxial A-type order that persists to the top surface layers in the AFM TI $MnBi_2Te_4$. Therefore, we can conclude that our MFM observation excludes some of the proposed surface relaxation models, and that the contradictory reports of gapless surface states and a QAHE remain unresolved.

Chapter 5

First Experimental Observation of Surface Spin-flop Transition on Natural Antiferromagnet

5.1 Introduction to Surface Spin-flop Transition

The observation of robust A-type order on the $MnBi_2Te_4$ surface also provides a rare opportunity to explore the interesting "surface spin-flop" (or inhomogeneous spin-flop) transition, which was first proposed by Mills decades ago using an effective one-dimensional spin-chain model with AFM nearest-neighbor exchange coupling[160]. In this model, the ends have no neighbors, which leads to a weaker exchange coupling at the ends, as shown in Fig. 5.1(a). Thus, the spins on the ends flop at lower magnetic field than the bulk.

Five years later, the model was revisited [162], where analogous to crystal melting, the surface flops first and then the spin-flop state migrates into the bulk. Later studies suggested an intriguing scenario of inhomogeneous spin-flop states due to finite size effect[161, 163, 164]. Additionally, one study suggests that the term "surface spin-flop" is sort of a misnomer since the surface spin-flop state is not pinned onto the surface, it first migrates into the bulk and then expands to initiate the bulk spin-flop state[161], as shown in Fig. 5.1(b). The "surface spin-flop" has been experimentally observed in synthetic AFMs, which are superlattices of antiferromagnetically coupled ferromagnetic layers. Figures 5.2 (a,b) show experimental observations of the surface spin-flop using Kerr, SQUID and MOKE in two different synthetic AFMs[165, 166]. Thus far however, it has yet to be observed in natural AFMs[161, 163].

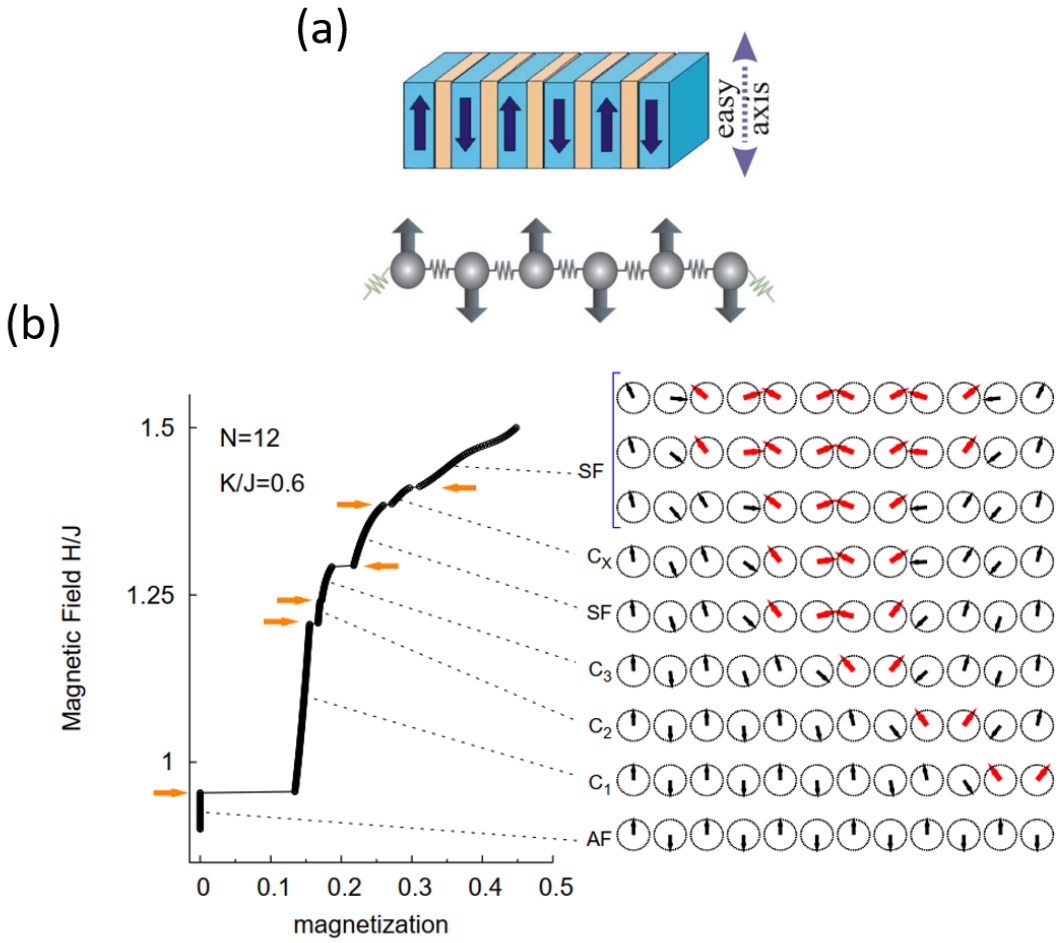

Figure 5.1: (a) Sketch of an antiferromagnetically coupled multilayer corresponding one-dimensional spin chain. The "exchange springs" are cut at the ends of the finite chain. (b) Equilibrium solutions for Mills' model with N=16 and intermediate anisotropy K/J = 0.5. In increasing field a series of transition lead from antiferromagnetic to ferromagnetic phase via several canted and (reentrant) spin-flop states. Left panel: magnetization of the equilibrium states (first-order transitions are marked by arrows). Right panel: spin-configurations in the canted spin-flop states.[161]

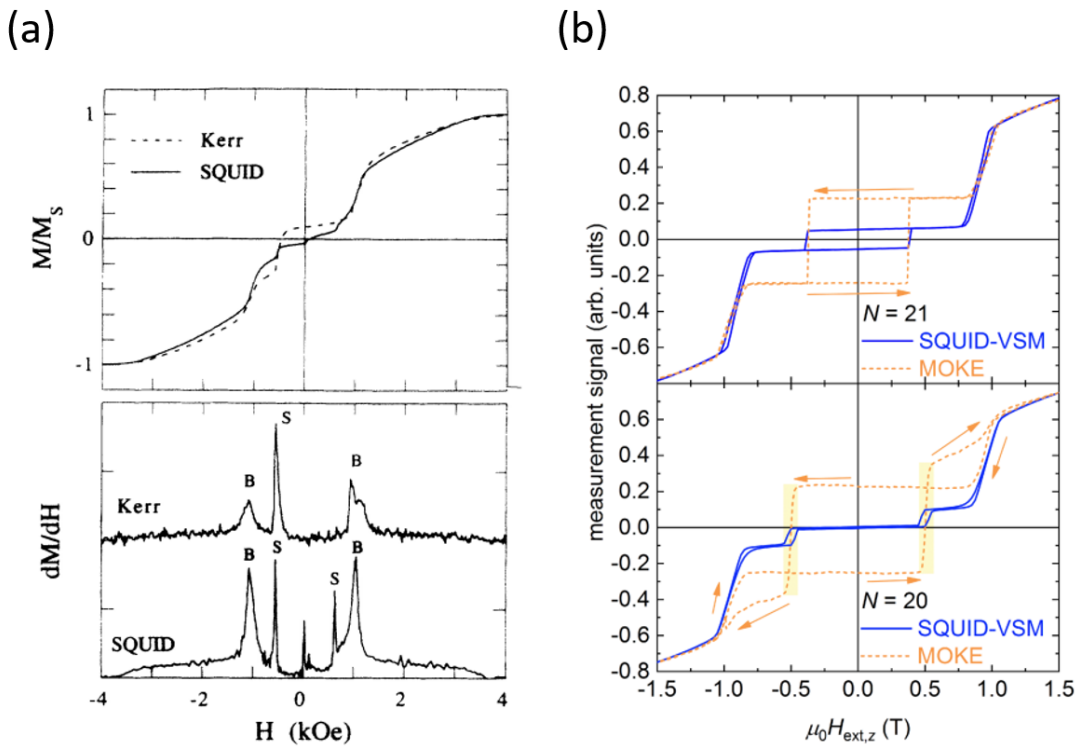

Figure 5.2: (a) (Top) Magnetization curve of a [Fe(40 Å)/Cr(11 Å)]$_{22}$ superlattice from -M, to M, with the applied field parallel to the magnetic easy axis. The solid line is measured by a SQUID magnetometer and the dashed line is measured by longitudinal magneto-optic Kerr effect. (Bottom) The numerical derivative of the measured curves in (top). S and B refer to the surface and bulk spin-flop transitions, respectively[165]. (b) Comparison of out-of-plane hysteresis loops measured by SQUID-VSM and MOKE for (top) number of layers N = 21 and (bottom) N = 20 of $[(\mathrm{Co/Pt})_{x-1}/\mathrm{Co/Ir}]_{N-1}/(\mathrm{Co/Pt})_x$ multilayers. For convenience, the MOKE data are scaled to match the SQUID-VSM data in the high-field range[166].

Because of the existence of domains in natural AFMs, the exploration of surface spin-flop phenomena requires a surface-sensitive magnetic imaging probe with sufficient spatial resolution in high magnetic field. These challenges were overcome by our cryogenic MFM[137, 157]. Our results not only shed new light on the realization of topological states in AFMs, but also open up exciting explorations of surface metamagnetic transitions in functional AFMs.

5.2 Visualization of Surface Spin-Flop Transition

Figures 5.3(a-h) show selected MFM images measured in various magnetic fields from 1.0 to 3.5 T. Clearly, the termination-dependent contrast shows non-monotonic magnetic field dependence. As discussed in connection with Fig. 4.3, in low magnetic field a bright contrast indicates surface termination with antiparallel magnetization denoted as a, while dark contrast indicates surface termination with parallel magnetization denoted as b in Fig. 4.3(a). This domain contrast persists in finite magnetic field up to ∼1.85 T, then fine features start to emerge in termination a during the domain contrast reversal, while the termination b remains featureless. Thus, it is the termination a (antiparallel magnetization) that undergoes surface spin-flop (SSF) transition at $H^1_{\rm SSF} \sim 1.85$ T. Similar behavior was observed at ∼3.1 T except the roles of a and b are switched. Thus, it is the termination b (parallel magnetization) that undergoes surface spin-flop transition at $H^2_{\rm SSF} \sim 3.1$ T. Finally, the domain contrast disappears around the bulk spin-flop (BSF) transition ($H_{\rm BSF} \sim 3.5T$). The detailed field dependence of domain contrast is plotted in Fig. 5.3(w), where the domain contrast is defined as the difference of the average MFM signals in the two regions (domain a and b) marked by red boxes in Fig. 5.3(a). This effect is also observed in negative applied field, shown in Fig. 5.4, and is reproducible in other sample locations after thermal cycling, as shown in Fig. 5.5 and on a cleaved crystal of $MnBi_2Te_4$, shown in Fig. 5.6. No hysteresis was found between up-sweep and down-sweep of the magnetic field. Interestingly,

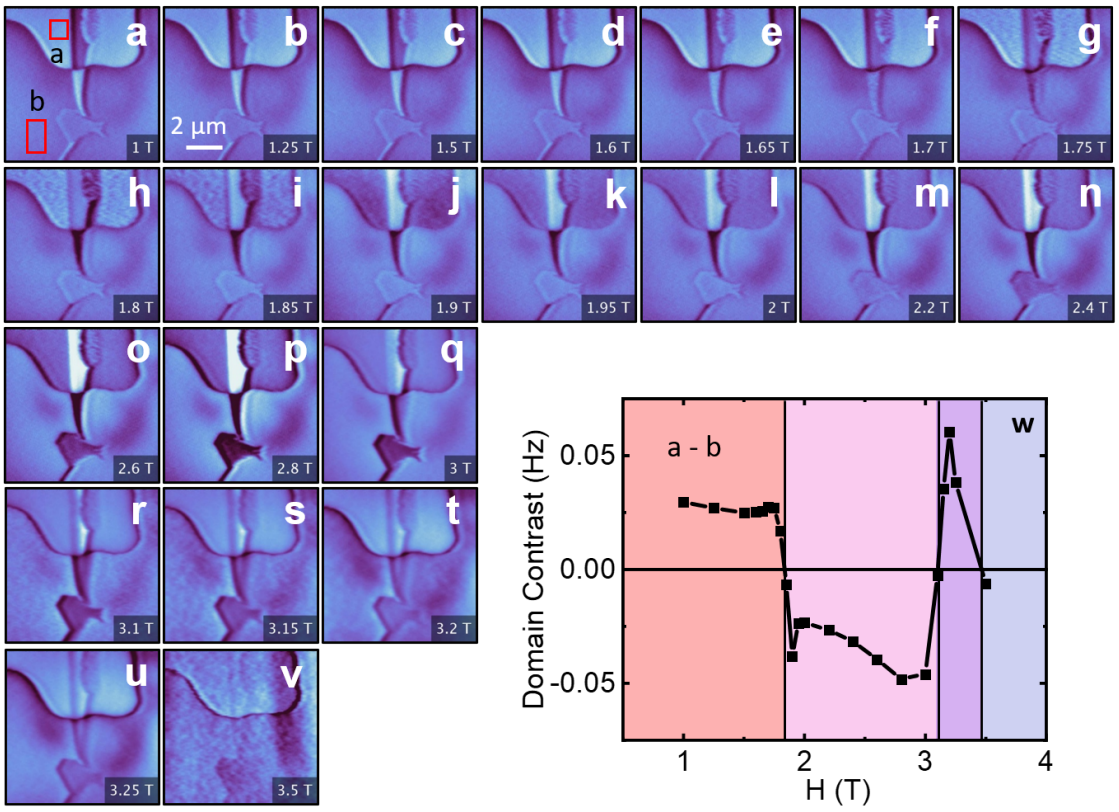

Figure 5.3: (a-v) MFM images taken at 5 K with increasing positive field labelled in lower right corners. (w) Domain contrast between red squares in (a) versus applied field. Below 1.75 T, the domain contrast is constant. As the applied field is increased, the domain contrast quickly reverses around 1.85 and 3.1 T. Above 3.5 T, the system enters the CAFM phase. Near 1.85 T, the bright domain starts to appear rougher and darker, i.e. the antiparallel surface domain spin-flops. At 3.1 T, the next lower SL spin-flops due to its interaction with the spin-flopped surface layer, and thus, the bright domain again begins to appear rougher and darker. The color scale for MFM images is 0.3 (a-q) and 0.8 (r-v) Hz.

the step-edge contrast in box *c* of Fig. 5.5(a) appears to reverse before the domain contrast in box *a*. The red and black vertical lines in Fig. 5.5(n) indicate where the first SSF occurs. The step-edge contrast also appears to have double the contrast of the domain contrast and the increase in contrast above the first transition is also more pronounced. All of these additional effects could be due to the finite size of the step edge, which will be explored in future studies.

The first SSF transition $\left(H^{1}_{\mathrm{SSF}} \approx 0.5 H_{\mathrm{BSF}}\right)$ agrees well with prior observation in synthetic AFMs[166], and is in reasonable agreement with that of Mills' model $\left(H^{\mathrm{th}}_{\mathrm{SSF}} \approx 0.7 H_{\mathrm{BSF}}\right)$ [162, 164]. However, the second surface spin-flop transition $\left(H^{2}_{\mathrm{SSF}} \approx 0.9 H_{\mathrm{BSF}}\right)$ of the surface with parallel magnetization is unexpected in prior studies [161, 164, 165] indicating surface relaxation of the A-type AFM order. To confirm this, we studied the revised Mills' model with additional surface relaxation effects such as reduced magnetization, exchange coupling, and/or anisotropy energy[161] (see Appendix A for details).

5.3 Simulation of a Revised Mills' Model

In Mills' original model, the antiparallel surface nucleates a horizontal DW with a spin-flop state that migrates into the bulk, forming an inhomogeneous state that precedes the bulk spin-flop transition[161, 162, 164]. If the migration indeed occurs, the antiparallel surface would sequentially turn into a parallel surface, resulting in an identical magnetization state on the two domains, *i.e.,* no domain contrast above the SFF transition. Such behavior is inconsistent with our experimental observation of domain contrast reversal. Our simulation reveals that the horizontal DW with spin-flop state can be pinned to surface layers if the magnetization of the surface layer is reduced by more than 10%(see Appendix A). Indeed, the revised Mills' model with surface relaxation effect can reproduce the two successive SSF transitions in a reasonably wide parameter space.

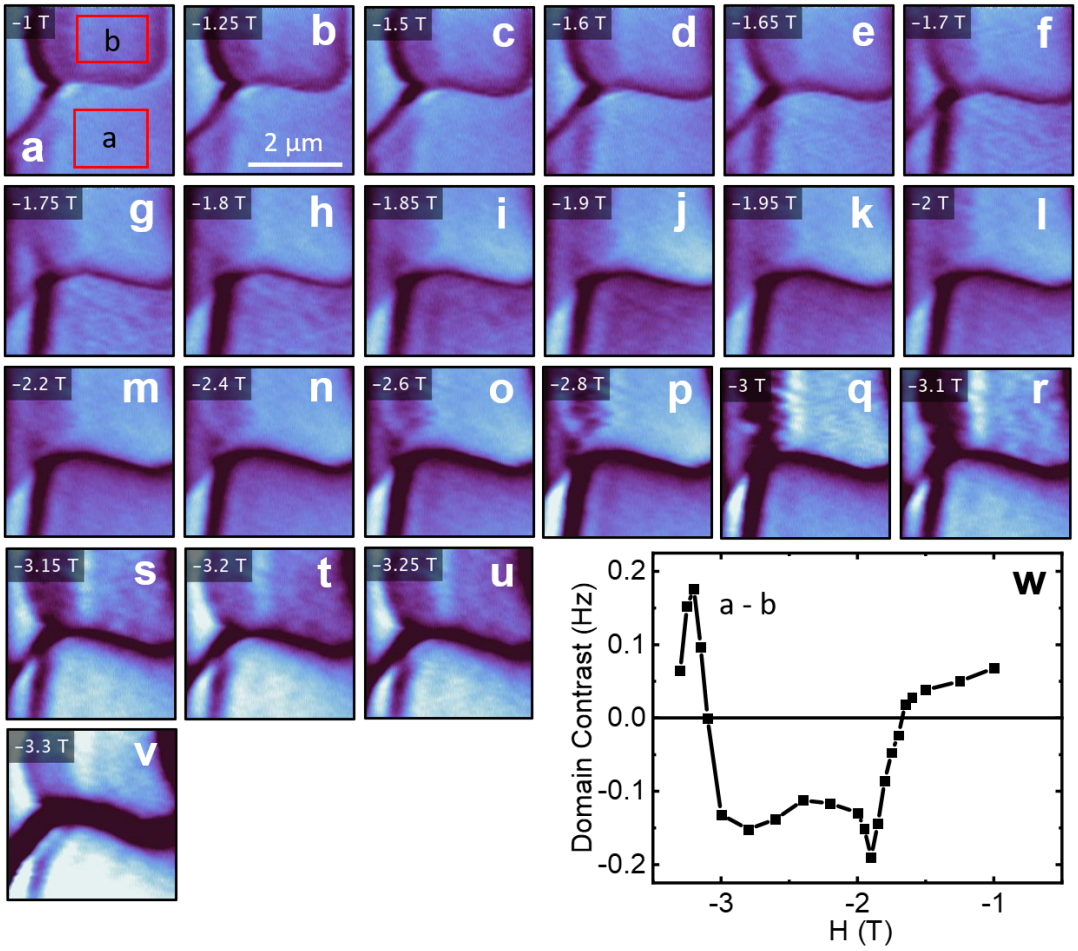

Figure 5.4: (a-v) MFM images of upper right domain in Fig. 5.3 with increasing negative field labelled in lower right corners. (w) Domain contrast between red squares in a versus applied field. Below -1.65 T, the domain contrast is decreases slowly, until around -1.75 T, the domain contrast quickly reverses, and again at -3.1 T. Above -3.5 T, the system enters the CAFM phase. Near -1.7 T (f), the bright domain starts to appear rougher and darker, i.e. the antiparallel surface domain spin-flops. At -3.1 T (r), the next lower SL spin-flops due to its interaction with the spin-flopped surface layer, and thus, the bright domain again begins to appear rougher and darker. The domain contrast shows similar qualitative behavior to the positive field run in Fig. 5.3, thus, the effect is symmetric in positive and negative field. The color scale for MFM images is 0.3 Hz.

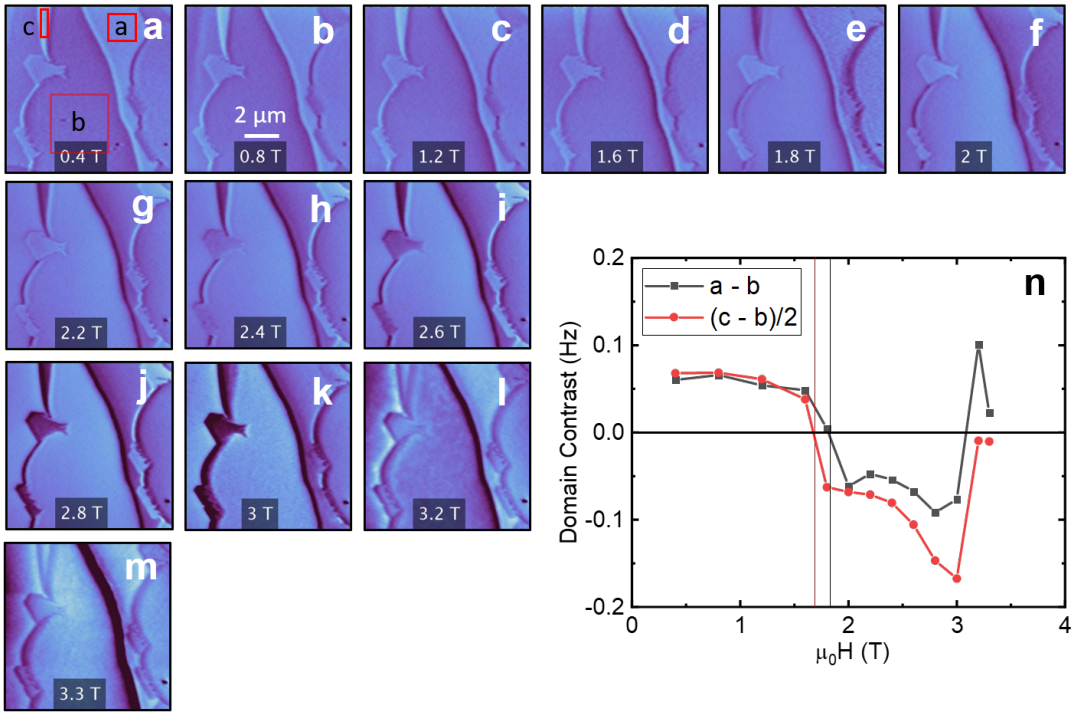

Figure 5.5: (a-m) MFM images taken at 5 K of zoomed out location of Fig. 5.3 after thermal cycling. A new DW was observed running down the middle of (a). (n) Domain and step-edge contrast between red squares in (a) versus applied field. Again, similar qualitative behavior in the domain contrast vs applied field was observed. The bright antiparallel domain in (e) begins to reverse around 1.8 T and then reverses again around 3.1 T (l). Thus, the domain reversal is reproducible even after thermal cycling to a different domain configuration. However, the step-edge contrast in box *c* appears to reverse before the domain contrast in box *a*. The red and black vertical lines in (n) indicate the SSF. The color scale for the MFM images is 0.5 Hz.

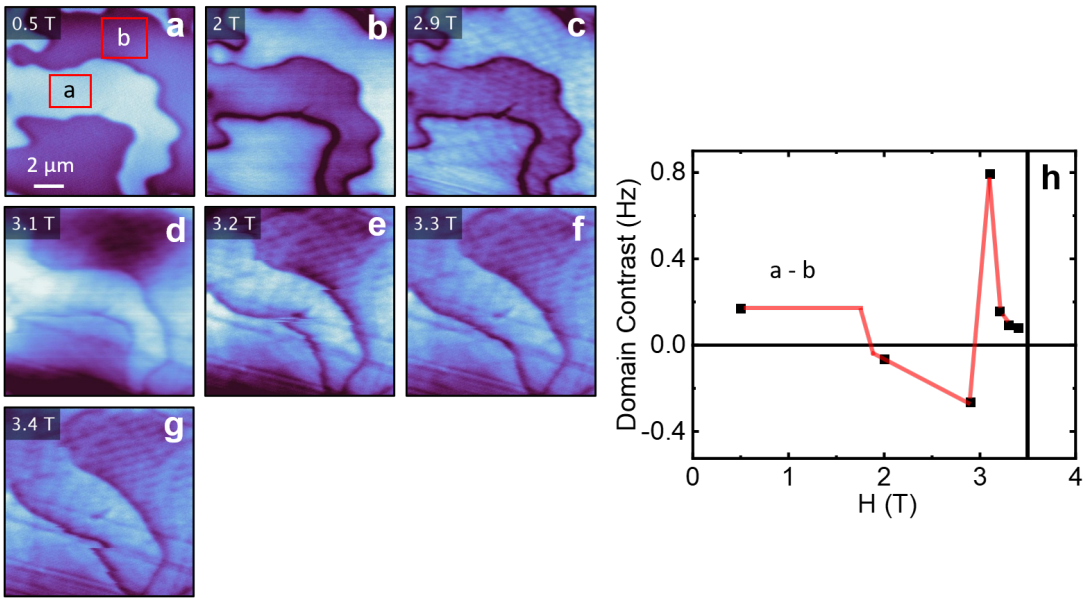

Figure 5.6: (a-g) MFM images taken at 15 K with increasing magnetic field on cleaved $MnBi_2Te_4$. (h) Domain contrast between red squares in a versus applied field. The red line is a guide to show contrast reversals. The domain reversal behavior on the cleaved surface is qualitatively similar to that on the as-grown surface. This shows that the surface flop is independent of a particular type of surface termination. The color scale for the MFM images is 0.5 Hz.

Figure 5.7(a) shows a phase diagram of the simulation using typical parameters exhibiting the emergent sequential SSF transitions on antiparallel (blue) and parallel (red) surfaces, respectively.

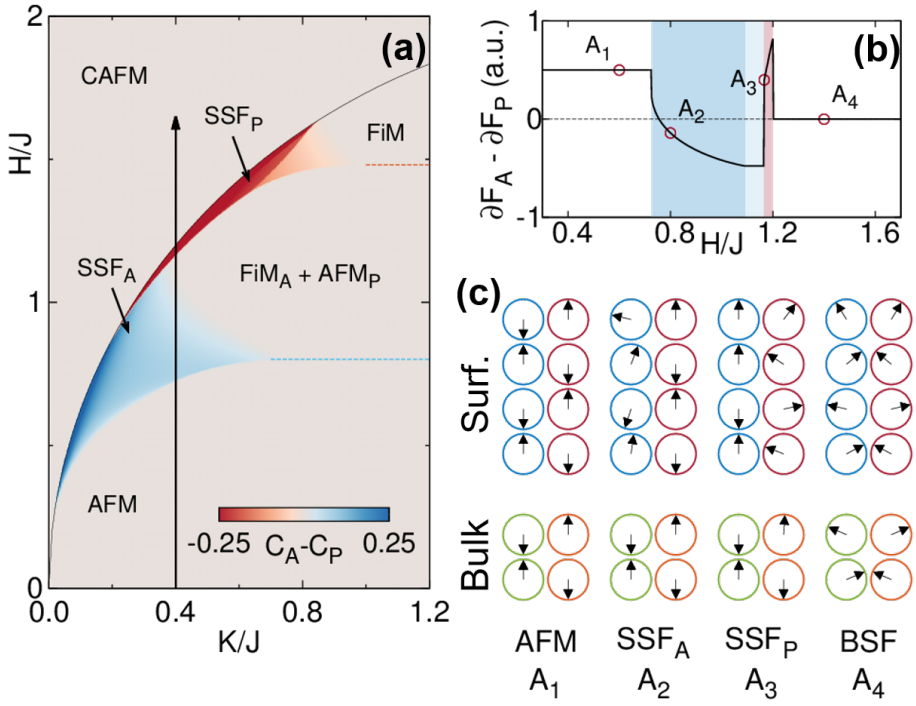

Figure 5.7: (a) Theoretical phase diagram of the spin-flop state in the revised Mills' model. Blue and red colored regimes illustrate surface spin-flop states for antiparallel and parallel surfaces, respectively. Color code denotes the difference of net spin canting between the two types of surfaces (see text). Black solid line is a phase boundary of the bulk spin-flop state; dashed line is a boundary between AFM and surface spin-flip phases for antiparallel (blue) and parallel (red) surfaces. (b) Simulated magnetic force gradient differences between antiparallel and parallel surfaces with respect to the external field. (c) Schematic illustration of the spin-flop process for surface (upper 4 rows) and bulk (lower) domains. Left blue (right red) represents antiparallel (parallel) surface spins, whereas, left green (right yellow) represents antiparallel (parallel) bulk spins.

In addition, the reduction of surface exchange coupling could explain the suppression of the SSF transition. The simulated MFM contrast (force gradient difference) as a function of magnetic field is shown in Fig. 5.7(b), qualitatively agreeing with the experimental observation shown in Fig. 5.3(w) (see Appendix A for details on force gradient simulation).

The successive SSF and BSF transitions are summarized schematically in Fig. 5.7(c). The antiparallel surface layer (blue) undergoes a SSF transition H^1_{SSF} where the MFM contrast reverses. The domain contrast increases even further in this region, likely due to an increasing canted moment of the spin-flop state. At the next critical field H^2_{SSF}, the parallel surface (red) undergoes a SSF transition, resulting in another reversal of the MFM contrast. Finally, the MFM domain contrast disappears above the BSF transition because both domains have the same canted moments.

To explore the impact of thermal fluctuations, we performed MFM studies at higher temperatures below T_N to extract the T dependence of the SSF transitions $\left(H^1_{\mathrm{SSF}} \text{ and } H^2_{\mathrm{SSF}}\right)$. An example of the SSF transitions at higher temperature is shown in Fig. 5.8.

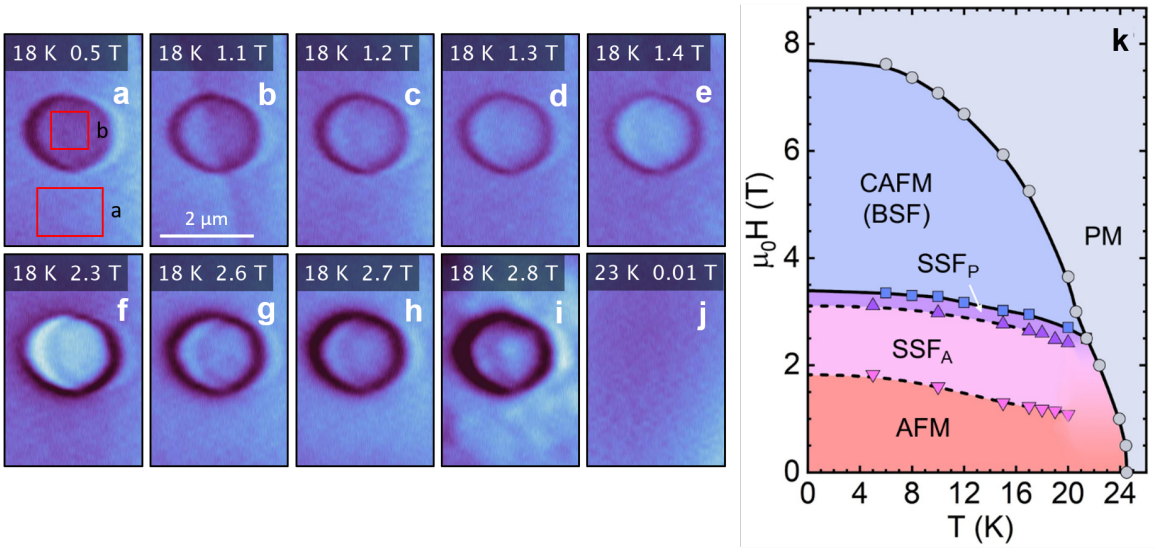

Figure 5.8: (a-j) MFM images taken at 18 K on as-grown MBT with increasing field. The surface flop transitions appear around 1.2 T (c) and 2.6 T (g). Domain contrast between a and b in bubble domain was used to construct phase diagram of surface transitions. (j) MFM image at same location at 23 K and 0.01 T where bubble domain disappeared. The surface flop transition is likely suppressed somewhere in the range of 20-23 K because the spin-flop transition merges with saturation transition above the bicritical point ($\sim$ 22 K, 2.5 T). (k) H-T phase diagram showing A-type AFM phase (red), SSF_A and SSF_P spin-flop phase (pink and light purple), bulk CAFM phase (dark purple), and forced ferromagnetic or paramagnetic (PM) phase (light blue).The color scale for the MFM images is 0.3 Hz.

As shown in Fig. 5.8(k), the temperature dependence of both SSF transitions follow that of the BSF (H_{BSF}), which gradually reduces with increasing temperature until the bicritical point ($\sim$21 K, $\sim$2.5 T), indicating the relative energetics of the SSF transitions do not vary much with temperature. Above 21 K, the AFM domains become unstable in finite magnetic field because of enhanced thermal fluctuations, making it difficult to determine the SSF transitions in this temperature window.

5.4 Conclusion

We observed, for the first time, the long-sought surface spin-flop transition in natural AFMs. More interestingly, we discovered an additional surface spin-flop transition on the parallel magnetization surface, which indicates surface relaxation of the A-type order. The MFM observation of the surface spin-flop transition not only opens a new paradigm for visualizing surface metamagnetic transitions in AFM spintronic devices, but also provides new insights into the realization of the QAH or axion-insulator states in topological AFMs[102, 105].

Chapter 6

Conclusion and Outlook

AFM order in topological materials has recently become incredibly important in the quest for exotic phenomena such as high temperature QAHE, quantized magnetoelectric effect, chiral edge modes, and Weyl and Dirac semimetal states. However, there is a lack of understanding of the AFM domains and DWs in these materials. The control of these DWs or spin textures is not only important for controlling these states, but also crucial for spintronic applications of AFMs. Despite many efforts, it has been challenging to directly visualize AFM domains or DWs with nanoscale resolution, especially in magnetic field.

Our results in chapter 3 demonstrate that DWs of A-type AFM order in $MnSb_2Te_4$, $MnBi_{1.37}Sb_{0.63}Te_4$, and $MnBi_2Te_4$ and the Dirac semimetal $EuMnBi_2$ can be visualized by cryogenic MFM utilizing the susceptibility (magnetization) difference between DWs and domains[147]. This susceptibility contrast mechanism is different from the ferromagnetic core mechanism established in synthetic AFMs[144]. For DWs to be in the flop state, the only requirement is uniaxial anisotropy, which is quite general and is satisfied in many functional AFMs[123]. Recent advances in spintronics and 2D materials reveal exciting properties in uniaxial AFMs, *e.g.* spin Seebeck effect in MnF_2 heterostructures[149], giant tunneling magnetoresistance using CrI_3 flakes[150, 151], and quantum transport in the Dirac semimetal $EuMnBi_2$ and related compounds[83]. The visualization and manipulation of DWs in these materials will help to understand the fundamental mechanisms of these fascinating phenomena and their potential applications. Similarly, imaging and control of DWs in AFM TIs such as $MnBi_{2-x}Sb_xTe_4$ will facilitate the exploration of chiral edge

states at the DWs[106], and the realization of a single domain state, which is necessary for an unambiguous observation of the axion insulator and QAH states[102, 105, 108]. The weakly pinned DWs observed in the $MnBi_2Te_4$ family might be manipulated by electric current via spin-transfer-torque[143, 152], which could lead to low power logic or memory devices[123, 124].

Through this application, we present in chapter 4 microscopic evidence of the persistence of uniaxial A-type AFM order to the surface layers of $MnBi_2Te_4$ single crystals using MFM. Our results reveal termination-dependent magnetic contrast across both surface step edges and DWs, which can be screened by thin layers of soft magnetism. Therefore, we can conclude that our MFM observation excludes some of the proposed surface relaxation models, and that the contradictory reports of gapless surface states and a QAHE remain unresolved.

In chapter 5 we observed, for the first time, the long-sought surface spin-flop transition in a natural AFM. More interestingly, we discovered an additional surface spin-flop transition on the parallel magnetization surface, which indicates surface relaxation of the A-type order, further corroborating our observation of the persistence of A-type AFM order to the surface of $MnBi_2Te_4$.

The direct visualization of these DWs and domain structures in magnetic field not only provides key ingredients for understanding the electronic properties of the AFM TI $MnBi_2Te_4$, but also opens both a new paradigm for exploring intrinsic surface metamagnetic transitions in natural AFMs and a new path toward control and manipulation of DWs or spin textures in functional AFMs.

In future studies, this magnetic susceptibility imaging technique will be extended to many other AFM systems. For example, for studying the spin-flop transition in the AFM Cr_2O_3[132], the higher order members of the $MnBi_{2n}Te_{3n+1}$, $MnBi_4Te_7$ or $MnBi_6Te_10$[167], which could have different ordering than $MnBi_2Te_4$. The magnetism of thin flakes of

$MnBi_2Te_4$[102, 105] requires further study too in order to fully understand the limitations on the current observed QAHE. The spin-flop transition in the Dirac semimetal $EuMnBi_2$ will also continue to be studied[83]. Additionally, this technique will be extended to other types of uniaxial AFM systems such as G-type and C-type, where DW contrast should still be visible.

Bibliography

[1] J. C. Maxwell, *A treatise on electricity and magnetism*volume 03, 1 ed. (Clarendon Press, 1873).

[2] E. H. Hall, "On a new action of the magnet on electric currents," *American Journal of Mathematics* **2**, 287 (1879).

[3] E. H. Hall, "On the "Rotational Coefficient" in nickel and cobalt," *Phil. Mag.* **12**, 157 (1881).

[4] H. Weng *et al.*, "Quantum anomalous Hall effect and related topological electronic states," *Adv. Phys.* **64**, 227 (2015).

[5] A. Kundt, "On the Hall effect in ferromagnetic materials," *Wied. Ann.* **49**, 257 (1893).

[6] E. M. Pugh, "Hall Effect and the Magnetic Properties of Some Ferromagnetic Materials," *Phys. Rev.* **36**, 1503 (1930).

[7] R. Karplus and J. M. Luttinger, "Hall Effect in Ferromagnetics," *Phys. Rev.* **95**, 1154 (1954).

[8] Y. K. Kato, "Observation of the Spin Hall Effect in Semiconductors," *Science* **306**, 1910 (2004).

[9] L. Shubnikov and W. de Haas, *Leiden Communication* **3** (1930).

[10] P. M. v. A. W. J. de Haas, *Proc. Netherlands Roy, Acad. Sci.* **33**, 1106 (1930).

[11] L. Landau, "Diamagnetismus der Metalle," *Zeitschrift fur Physik* **64**, 629 (1930).

[12] L. Onsager, "Interpretation of the de Haas-van Alphen effect," *The London, Edinburgh, and Dublin Philosophical Magazine and Journal of Science* **43**, 1006 (1952).

[13] A. B. Fowler *et al.*, "Magneto-Oscillatory Conductance in Silicon Surfaces," *Phys. Rev. Lett.* **16**, 901 (1966).

[14] K. v. Klitzing, G. Dorda, and M. Pepper, "New Method for High-Accuracy Determination of the Fine-Structure Constant Based on Quantized Hall Resistance," *Phys. Rev. Lett.* **45**, 494 (1980).

[15] A. Bestwick *et al.*, "Precise Quantization of the Anomalous Hall Effect near Zero Magnetic Field," *Phys. Rev. Lett.* **114**, 1 (2015).

[16] R. B. Laughlin, "Quantized Hall conductivity in two dimensions," *Phys. Rev. B* **23**, 5632 (1981).

[17] D. J. Thouless *et al.*, "Quantized Hall Conductance in a Two-Dimensional Periodic Potential," *Phys. Rev. Lett.* **49**, 405 (1982).

[18] J. E. Avron, R. Seiler, and B. Simon, "Homotopy and Quantization in Condensed Matter Physics," *Phys. Rev. Lett.* **51**, 51 (1983).

[19] M. Berry, "Quantal phase factors accompanying adiabatic changes," *Proceedings of the Royal Society of London. A. Mathematical and Physical Sciences* **392**, 45 (1984).

[20] B. Simon, "Holonomy, the Quantum Adiabatic Theorem, and Berry's Phase," *Phys. Rev. Lett.* **51**, 2167 (1983).

[21] S. A. Wolf, "Spintronics: A Spin-Based Electronics Vision for the Future," *Science* **294**, 1488 (2001).

[22] C. L. Kane and E. J. Mele, "Quantum Spin Hall Effect in Graphene," *Phys. Rev. Lett.* **95**, 1 (2005).

[23] B. A. Bernevig, T. L. Hughes, and S.-C. Zhang, "Quantum Spin Hall Effect and Topological Phase Transition in HgTe Quantum Wells," *Science* **314**, 1757 (2006).

[24] S. Murakami, N. Nagaosa, and S.-C. Zhang, "Spin-Hall Insulator," *Phys. Rev. Lett.* **93**, 6 (2004).

[25] J. E. Moore, "The birth of topological insulators," *Nature* **464**, 194 (2010) arXiv:1011.5462v1.

[26] L. Fu and C. L. Kane, "Time reversal polarization and aZ2adiabatic spin pump," *Phys. Rev. B* **74**, 195312 (2006).

[27] M. Z. Hasan and C. L. Kane, "Colloquium: Topological insulators," *Rev. Mod. Phys.* **82**, 3045 (2010) 1002.3895.

[28] H. Min *et al.*, "Intrinsic and Rashba spin-orbit interactions in graphene sheets," *Phys. Rev. B* **74**, 1 (2006).

[29] B. A. Bernevig, T. L. Hughes, and S.-C. Zhang, "Quantum Spin Hall Effect and Topological Phase Transition in HgTe Quantum Wells," *Science* **314**, 1757 (2006).

[30] M. Konig *et al.*, "Quantum Spin Hall Insulator State in HgTe Quantum Wells," *Science* **318**, 766 (2007).

[31] Z. Hasan, "Experiments Provide First Direct Signatures of a Topological Insulator - a New Phase of Quantum Matter," *Stanford Synchrotron Radiation Lightsource Science Review* (2009).

[32] L. Fu and C. L. Kane, "Topological insulators with inversion symmetry," *Phys. Rev. B* **76**, 1 (2007) 0611341.

[33] D. Hsieh *et al.*, "A topological Dirac insulator in a quantum spin Hall phase," *Nature* **452**, 970 (2008).

[34] Y. L. Chen *et al.*, "Experimental Realization of a Three-Dimensional Topological Insulator, Bi2Te3," *Science* **325**, 178 (2009).

[35] H. Zhang *et al.*, "Topological insulators in Bi2Se3, Bi2Te3 and Sb2Te3 with a single Dirac cone on the surface," *Nat. Phys.* **5**, 438 (2009).

[36] Y. Xia *et al.*, "Observation of a large-gap topological-insulator class with a single Dirac cone on the surface," *Nat. Phys.* **5**, 398 (2009).

[37] D. Hsieh *et al.*, "Observation of Time-Reversal-Protected Single-Dirac-Cone Topological-Insulator States in Bi2Te3 and Sb2Te3," *Phys. Rev. Lett.* **103**, 6401 (2009).

[38] R. Yu *et al.*, "Quantized Anomalous Hall Effect in Magnetic Topological Insulators," *Science* **329**, 61 (2010).

[39] A. M. Essin, J. E. Moore, and D. Vanderbilt, "Magnetoelectric Polarizability and Axion Electrodynamics in Crystalline Insulators," *Phys. Rev. Lett.* **102**, 259902 (2009).

[40] X.-L. Qi *et al.*, "Inducing a Magnetic Monopole with Topological Surface States," *Science* **323**, 1184 (2009).

[41] C.-X. Liu *et al.*, "Quantum Anomalous Hall Effect inHg1-yMnyTeQuantum Wells," *Phys. Rev. Lett.* **101**, 6802 (2008) 0802.2711.

[42] I. Knez, R.-R. Du, and G. Sullivan, "Evidence for Helical Edge Modes in InvertedInAs/GaSbQuantum Wells," *Phys. Rev. Lett.* **107**, 136603 (2011).

[43] R. R. Galazka, S. Nagata, and P. H. Keesom, "Paramagnetic—spin-glass—antiferromagnetic phase transitions inCd1-xMnxTefrom specific heat and magnetic susceptibility measurements," *Phys. Rev. B* **22**, 3344 (1980).

[44] K.-Y. Yang, Y.-M. Lu, and Y. Ran, "Quantum Hall effects in a Weyl semimetal: Possible application in pyrochlore iridates," *Phys. Rev. B* **84**, 075129 (2011).

[45] Z. Qiao *et al.*, "Quantum Anomalous Hall Effect in Graphene Proximity Coupled to an Antiferromagnetic Insulator," *Phys. Rev. Lett.* **112**, 1 (2014) arXiv:1501.04828v1.

[46] H. Zhang *et al.*, "Electrically Tunable Quantum Anomalous Hall Effect in Graphene Decorated by5dTransition-Metal Adatoms," *Phys. Rev. Lett.* **108**, 1 (2012) 1108.5915.

[47] Y. Wang *et al.*, "Interaction-induced quantum anomalous Hall phase in (111) bilayer ofLaCoO3," *Phys. Rev. B* **91**, 125139 (2015) arXiv:1409.6797v2.

[48] K. F. Garrity and D. Vanderbilt, "Chern Insulators from Heavy Atoms on Magnetic Substrates," *Phys. Rev. Lett.* **110**, 1 (2013) arXiv:1212.2942v1.

[49] K. F. Garrity and D. Vanderbilt, "Chern insulator at a magnetic rocksalt interface," *Phys. Rev. B* **90**, 5 (2014) 1404.0973.

[50] H. Zhang *et al.*, "Topological States in Ferromagnetic CdO/EuO Superlattices and Quantum Wells," *Phys. Rev. Lett.* **112**, 1 (2014) 1308.0349.

[51] X.-L. Qi, T. L. Hughes, and S.-C. Zhang, "Topological field theory of time-reversal invariant insulators," *Phys. Rev. B* **78**, 1 (2008) 0802.3537.

[52] P. Wei *et al.*, "Exchange-Coupling-Induced Symmetry Breaking in Topological Insulators," *Phys. Rev. Lett.* **110**, 186807 (2013).

[53] C.-Z. Chang, P. Wei, and J. S. Moodera, "Breaking time reversal symmetry in topological insulators," *MRS Bulletin* **39**, 867 (2014).

[54] C. Niu *et al.*, "Quantum anomalous Hall effect in doped ternary chalcogenide topological insulators TlBiTe2 and TlBiSe2," *Appl. Phys. Lett.* **99**, 142502 (2011).

[55] C.-Z. Chang *et al.*, "Experimental Observation of the Quantum Anomalous Hall Effect in a Magnetic Topological Insulator," *Science* **340**, 167 (2013) arXiv:1212.4783.

[56] J. G. Checkelsky *et al.*, "Trajectory of the anomalous Hall effect towards the quantized state in a ferromagnetic topological insulator," *Nat. Phys.* **10**, 731 (2014) 1406.7450.

[57] C.-Z. Chang *et al.*, "High-precision realization of robust quantum anomalous Hall state in a hard ferromagnetic topological insulator," *Nat. Mater.* **14**, 473 (2015).

[58] X. Kou *et al.*, "Scale-Invariant Quantum Anomalous Hall Effect in Magnetic Topological Insulators beyond the Two-Dimensional Limit," *Phys. Rev. Lett.* **113**, 1 (2014).

[59] Y. Feng *et al.*, "Observation of the Zero Hall Plateau in a Quantum Anomalous Hall Insulator," *Phys. Rev. Lett.* **115**, 126801 (2015).

[60] X. Kou *et al.*, "Metal-to-insulator switching in quantum anomalous Hall states," *Nat. Commun.* **6**, 8474 (2015).

[61] E. O. Lachman *et al.*, "Visualization of superparamagnetic dynamics in magnetic topological insulators," *Sci. Adv.* **1**, e1500740 (2015).

[62] C.-Z. Chang *et al.*, "Zero-Field Dissipationless Chiral Edge Transport and the Nature of Dissipation in the Quantum Anomalous Hall State," *Phys. Rev. Lett.* **115**, 057206 (2015) 1505.01896.

[63] M. Mogi *et al.*, "Magnetic modulation doping in topological insulators toward higher-temperature quantum anomalous Hall effect," *Appl. Phys. Lett.* **107**, 182401 (2015).

[64] Y. Ou *et al.*, "Enhancing the Quantum Anomalous Hall Effect by Magnetic Codoping in a Topological Insulator," *Adv. Mater.* **30**, 1703062 (2017).

[65] W. Wang *et al.*, "Direct evidence of ferromagnetism in a quantum anomalous Hall system," *Nat. Phys.* **14**, 791 (2018).

[66] S. M. Young *et al.*, "Dirac Semimetal in Three Dimensions," *Phys. Rev. Lett.* **108**, 140405 (2012).

[67] Z. K. Liu *et al.*, "Discovery of a Three-Dimensional Topological Dirac Semimetal, Na3Bi," *Science* **343**, 864 (2014).

[68] S.-Y. Xu *et al.*, "Observation of Fermi arc surface states in a topological metal," *Science* **347**, 294 (2014).

[69] M. Neupane *et al.*, "Observation of a three-dimensional topological Dirac semimetal phase in high-mobility Cd3As2," *Nat. Commun.* **5**, 3786 (2014).

[70] S. Borisenko *et al.*, "Experimental Realization of a Three-Dimensional Dirac Semimetal," *Phys. Rev. Lett.* **113**, 27603 (2014).

[71] H. Weyl, "Elektron und Gravitation. I," *Zeitschrift fur Physik* **56**, 330 (1929).

[72] O. Vafek and A. Vishwanath, "Dirac Fermions in Solids: From High-TcCuprates and Graphene to Topological Insulators and Weyl Semimetals," *Annual Review of Condensed Matter Physics* **5**, 83 (2014).

[73] X. Wan *et al.*, "Topological semimetal and Fermi-arc surface states in the electronic structure of pyrochlore iridates," *Phys. Rev. B* **83**, 205101 (2011).

[74] G. Xu *et al.*, "Chern Semimetal and the Quantized Anomalous Hall Effect in-HgCr2Se4," *Phys. Rev. Lett.* **107**, 186806 (2011).

[75] H. Nielsen and M. Ninomiya, "The Adler-Bell-Jackiw anomaly and Weyl fermions in a crystal," *Phys. Lett. B* **130**, 389 (1983).

[76] B. Z. Spivak and A. V. Andreev, "Magnetotransport phenomena related to the chiral anomaly in Weyl semimetals," *Phys. Rev. B* **93**, 85107 (2016).

[77] H. Weng *et al.*, "Weyl Semimetal Phase in Noncentrosymmetric Transition-Metal Monophosphides," *Phys. Rev. X* **5**, 11029 (2015).

[78] S.-Y. Xu *et al.*, "Discovery of a Weyl fermion semimetal and topological Fermi arcs," *Science* **349**, 613 (2015).

[79] B. Lv *et al.*, "Experimental Discovery of Weyl Semimetal TaAs," *Phys. Rev. X* **5**, 31013 (2015).

[80] B. Q. Lv *et al.*, "Observation of Weyl nodes in TaAs," *Nat. Phys.* **11**, 724 (2015).

[81] J. Park *et al.*, "Anisotropic Dirac Fermions in a Bi Square Net ofSrMnBi2," *Phys. Rev. Lett.* **107**, 126402 (2011).

[82] K. Wang *et al.*, "Quantum transport of two-dimensional Dirac fermions in SrMnBi2," *Phys. Rev. B* **84**, 220401 (2011).

[83] H. Masuda *et al.*, "Quantum Hall effect in a bulk antiferromagnet EuMnBi2 with magnetically confined two-dimensional Dirac fermions," *Sci. Adv.* **2**, e1501117 (2016).

[84] C. Felser and B. Yan, "Weyl Semimetals: Magnetically induced," *Nat. Mater.* **15**, 1149 (2016).

[85] M. Hirschberger *et al.*, "The chiral anomaly and thermopower of Weyl fermions in the half-Heusler GdPtBi," *Nat. Mater.* **15**, 1161 (2016).

[86] L. Šmejkal *et al.*, "Topological antiferromagnetic spintronics," *Nat. Phys.* **14**, 242 (2018).

[87] S. Nakatsuji, N. Kiyohara, and T. Higo, "Large anomalous Hall effect in a non-collinear antiferromagnet at room temperature," *Nature* **527**, 212 (2015).

[88] N. Kiyohara, T. Tomita, and S. Nakatsuji, "Giant Anomalous Hall Effect in the Chiral Antiferromagnet Mn3Ge," *Phys. Rev. Appl* **5**, 64009 (2016).

[89] A. K. Nayak *et al.*, "Large anomalous Hall effect driven by a nonvanishing Berry curvature in the noncolinear antiferromagnet Mn3Ge," *Sci. Adv.* **2**, e1501870 (2016).

[90] B. Göbel *et al.*, "Antiferromagnetic skyrmion crystals: Generation, topological Hall, and topological spin Hall effect," *Phys. Rev. B* **96**, 60406 (2017).

[91] P. M. Buhl *et al.*, "Topological spin Hall effect in antiferromagnetic skyrmions," *physica status solidi (RRL) - Rapid Research Letters* **11**, 1700007 (2017).

[92] A. K. Nayak *et al.*, "Magnetic antiskyrmions above room temperature in tetragonal Heusler materials," *Nature* **548**, 561 (2017).

[93] J. Jena *et al.*, "Observation of Magnetic Antiskyrmions in the Low Magnetization Ferrimagnet Mn2Rh0.95Ir0.05Sn," *Nano Lett.* **20**, 59 (2019).

[94] X.-L. Qi and S.-C. Zhang, "The quantum spin Hall effect and topological insulators," *Phys. Today* **63**, 33 (2010).

[95] Q. L. He *et al.*, "Chiral Majorana fermion modes in a quantum anomalous Hall insulator–superconductor structure," *Science* **357**, 294 (2017).

[96] I. Lee *et al.*, "Imaging Dirac-mass disorder from magnetic dopant atoms in the ferromagnetic topological insulator Crx(Bi0.1Sb0.9)2-xTe3," *Proceedings of the National Academy of Sciences* **112**, 1316 (2015).

[97] S. Grauer *et al.*, "Coincidence of superparamagnetism and perfect quantization in the quantum anomalous Hall state," *Phys. Rev. B* **92**, 201304 (2015).

[98] R. S. K. Mong, A. M. Essin, and J. E. Moore, "Antiferromagnetic topological insulators," *Phys. Rev. B* **81**, 245209 (2010).

[99] C. L. Kane and E. J. Mele, "Z2 Topological Order and the Quantum Spin Hall Effect," *Phys. Rev. Lett.* **95** (2005).

[100] T. Morimoto, A. Furusaki, and N. Nagaosa, "Topological magnetoelectric effects in thin films of topological insulators," *Phys. Rev. B* **92**, 85113 (2015).

[101] J. Wang *et al.*, "Quantized topological magnetoelectric effect of the zero-plateau quantum anomalous Hall state," *Phys. Rev. B* **92**, 81107 (2015).

[102] Y. Deng *et al.*, "Quantum anomalous Hall effect in intrinsic magnetic topological insulator MnBi2Te4," *Science* **367**, 895 (2020).

[103] J. Ge *et al.*, "High-Chern-Number and High-Temperature Quantum Hall Effect without Landau Levels," *Natl. Sci. Rev.* , 89 (2020).

[104] F. Wilczek, "Two applications of axion electrodynamics," *Phys. Rev. Lett.* **58**, 1799 (1987).

[105] C. Liu *et al.*, "Robust axion insulator and Chern insulator phases in a two-dimensional antiferromagnetic topological insulator," *Nat. Mater.* **19**, 522 (2020).

[106] N. Varnava and D. Vanderbilt, "Surfaces of axion insulators," *Phys. Rev. B* **98**, 245117. (2018).

[107] M. Gu *et al.*, "Half-quantized anomalous Hall effect in magnetic axion insulator $MnBi_2Te_4/(Bi_2Te_3)_n$," *arXiv* (2020) arXiv:2005.13943.

[108] J. Zhang, Z. Liu, and J. Wang, "In-plane magnetic-field-induced quantum anomalous Hall plateau transition," *Phys. Rev. B* **100** (2019).

[109] S.-W. Cheong and M. Mostovoy, "Multiferroics: a magnetic twist for ferroelectricity," *Nat. Mater.* **6**, 13 (2007).

[110] Y. Geng *et al.*, "Direct visualization of magnetoelectric domains," *Nat. Mater.* **13**, 163 (2014).

[111] D. Xiao *et al.*, "Realization of the Axion Insulator State in Quantum Anomalous Hall Sandwich Heterostructures," *Phys. Rev. Lett.* **120** (2018).

[112] U. Hartmann, "Magnetic Force Microscopy," *Annu. Rev. Mater. Sci.* **29**, 53 (1999).

[113] D. Vasyukov *et al.*, "A scanning superconducting quantum interference device with single electron spin sensitivity," *Nat. Nanotechnol.* **8**, 639 (2013).

[114] F. Casola, T. van der Sar, and A. Yacoby, "Probing condensed matter physics with magnetometry based on nitrogen-vacancy centres in diamond," *Nature Reviews Materials* **3** (2018).

[115] M. Yamanouchi *et al.*, "Velocity of Domain-Wall Motion Induced by Electrical Current in the Ferromagnetic Semiconductor (Ga,Mn)As," *Phys. Rev. Lett.* **96** (2006).

[116] S. Woo *et al.*, "Observation of room-temperature magnetic skyrmions and their current-driven dynamics in ultrathin metallic ferromagnets," *Nat. Mater.* **15**, 501 (2016).

[117] F. J. Giessibl, "Advances in atomic force microscopy," *Rev. Mod. Phys.* **75**, 949 (2003).

[118] G. Binnig, C. F. Quate, and C. Gerber, "Atomic Force Microscope," *Phys. Rev. Lett.* **56**, 930 (1986).

[119] G. Binnig *et al.*, "Surface Studies by Scanning Tunneling Microscopy," *Phys. Rev. Lett.* **49**, 57 (1982).

[120] D. Rugar *et al.*, "Magnetic force microscopy: General principles and application to longitudinal recording media," *J. Appl. Phys.* **68**, 1169 (1990).

[121] H. Takahashi, K. Ando, and Y. Shirakawabe, "Self-sensing piezoresistive cantilever and its magnetic force microscopy applications," *Ultramicroscopy* **91**, 63 (2002).

[122] A. Volodin *et al.*, "Low temperature magnetic force microscopy with enhanced sensitivity based on piezoresistive detection," *Rev. Sci. Instrum.* **71**, 4468 (2000).

[123] V. Baltz *et al.*, "Antiferromagnetic spintronics," *Rev. Mod. Phys.* **90**, 15005. (2018).

[124] T. Jungwirth *et al.*, "Antiferromagnetic spintronics," *Nat. Nanotechnol.* **11**, 231 (2016).

[125] R. A. Duine *et al.*, "Synthetic antiferromagnetic spintronics," *Nat. Phys.* **14**, 217 (2018).

[126] F. D. M. Haldane, "Model for a Quantum Hall Effect without Landau Levels: Condensed-Matter Realization of the "Parity Anomaly"," *Phys. Rev. Lett.* **61**, 2015 (1988).

[127] Y. Gong *et al.*, "Experimental realization of an intrinsic magnetic topological insulator," *Chin. Phys. Lett.* **36**, 076801 (2019).

[128] M. M. Otrokov *et al.*, "Prediction and observation of an antiferromagnetic topological insulator," *Nature* **576**, 416 (2019).

[129] M. Otrokov *et al.*, "Unique Thickness-Dependent Properties of the van der Waals Interlayer Antiferromagnet MnBi2Te4 Films," *Phys. Rev. Lett.* **122**, 107202. (2019).

[130] T. Jungwirth *et al.*, "The multiple directions of antiferromagnetic spintronics," *Nat. Phys.* **14**, 200 (2018).

[131] S.-W. Cheong *et al.*, "Seeing is believing: visualization of antiferromagnetic domains," *npj Quantum Materials* **5**, 3 (2020).

[132] M. Fiebig *et al.*, "Domain topography of antiferromagnetic Cr2O3 by second-harmonic generation," *Appl. Phys. Lett.* **66**, 2906 (1995).

[133] M. Bode *et al.*, "Atomic spin structure of antiferromagnetic domain walls," *Nat. Mater.* **5**, 477 (2006).

[134] R. D. Johnson *et al.*, "X-Ray Imaging and Multiferroic Coupling of Cycloidal Magnetic Domains in Ferroelectric MonodomainBiFeO3," *Phys. Rev. Lett.* **110**, 217206 (2013).

[135] F. P. Chmiel *et al.*, "Observation of magnetic vortex pairs at room temperature in a planar α-Fe2O3/Co heterostructure," *Nat. Mater.* **17**, 581 (2018).

[136] P. G. Evans, "X-ray Microdiffraction Images of Antiferromagnetic Domain Evolution in Chromium," *Science* **295**, 1042 (2002).

[137] P. M. Sass *et al.*, "Magnetic Imaging of Domain Walls in the Antiferromagnetic Topological Insulator MnBi2Te4," *Nano Lett.* **20**, 2609 (2020).

[138] M. G. Kim *et al.*, "Imaging antiferromagnetic antiphase domain boundaries using magnetic Bragg diffraction phase contrast," *Nat. Commun.* **9** (2018).

[139] J.-Q. Yan *et al.*, "Evolution of structural, magnetic, and transport properties in MnBi2-xSbxTe4," *Phys. Rev. B* **100**, 104409 (2019).

[140] J.-Q. Yan *et al.*, "Crystal growth and magnetic structure of MnBi2Te4," *Phys. Rev. Materials* **3**, 064202 (2019).

[141] S. Hamada *et al.*, "MFM observation of perpendicular magnetization and antiferromagnetically coupled domains in Co/Ru superlattices," *J. Magn. Magn. Mater.* **240**, 539 (2002).

[142] O. Hellwig *et al.*, "A new phase diagram for layered antiferromagnetic films," *Nat. Mater.* **2**, 112 (2003).

[143] S.-H. Yang, K.-S. Ryu, and S. Parkin, "Domain-wall velocities of up to 750 m s-1 driven by exchange-coupling torque in synthetic antiferromagnets," *Nat. Nanotechnol.* **10**, 221 (2015).

[144] O. Hellwig, A. Berger, and E. E. Fullerton, "Domain Walls in Antiferromagnetically Coupled Multilayer Films," *Phys. Rev. Lett.* **91**, 197203 (2003).

[145] Y. Geng *et al.*, "Collective Magnetism at Multiferroic Vortex Domain Walls," *Nano Lett.* **12**, 6055 (2012).

[146] S. Artyukhin *et al.*, "Landau theory of topological defects in multiferroic hexagonal manganites," *Nat. Mater.* **13**, 42 (2013).

[147] C. Israel, W. Wu, and A. de Lozanne, "High-field magnetic force microscopy as susceptibility imaging," *Appl. Phys. Lett.* **89**, 032502 (2006).

[148] M. Fiebig, D. Fröhlich, and H. J. Thiele, "Determination of spin direction in the spin-flop phase ofCr2O3," *Phys. Rev. B* **54**, R12681 (1996).

[149] S. M. Wu *et al.*, "Antiferromagnetic Spin Seebeck Effect," *Phys. Rev. Lett.* **116**, 097204. (2016).

[150] T. Song *et al.*, "Giant tunneling magnetoresistance in spin-filter van der Waals heterostructures," *Science* **360**, 1214 (2018).

[151] D. R. Klein *et al.*, "Probing magnetism in 2D van der Waals crystalline insulators via electron tunneling," *Science* **360**, 1218 (2018).

[152] L. Caretta *et al.*, "Fast current-driven domain walls and small skyrmions in a compensated ferrimagnet," *Nat. Nanotechnol.* **13**, 1154 (2018).

[153] H. Li *et al.*, "Dirac Surface States in Intrinsic Magnetic Topological Insulators EuSn2As2 and MnBi2nTe3n+1," *Phys. Rev. X* **9**, 041039 (2019).

[154] Y.-J. Hao *et al.*, "Gapless Surface Dirac Cone in Antiferromagnetic Topological Insulator MnBi2Te4," *Phys. Rev. X* **9**, 041038 (2019).

[155] Y. Chen *et al.*, "Topological Electronic Structure and Its Temperature Evolution in Antiferromagnetic Topological Insulator MnBi2Te4," *Phys. Rev. X* **9**, 041040 (2019).

[156] P. Swatek *et al.*, "Gapless Dirac surface states in the antiferromagnetic topological insulator MnBi2Te4," *Phys. Rev. B* **101**, 1 (2020).

[157] P. Sass *et al.*, "Robust A -Type Order and Spin-Flop Transition on the Surface of the Antiferromagnetic Topological Insulator MnBi2Te4," *Phys. Rev. Lett.* **125** (2020).

[158] Y. S. Hor *et al.*, "Development of ferromagnetism in the doped topological insulatorBi2-xMnxTe3," *Phys. Rev. B* **81**, 195203 (2010).

[159] X.-m. Ma *et al.*, "Hybridization-Induced Gapped and Gapless States on the Surfaces of Magnetic Topological Insulators," *arXiv:1912.13237* (2019).

[160] D. L. Mills, "Surface Spin-Flop State in a Simple Antiferromagnet," *Phys. Rev. Lett.* **20**, 18 (1968).

[161] U. K. Rößler and A. N. Bogdanov, "Reorientation in antiferromagnetic multilayers: Spin-flop transition and surface effects," *physica status solidi (c)* **1**, 3297 (2004).

[162] F. Keffer and H. Chow, "Dynamics of the Antiferromagnetic Spin-Flop Transition," *Phys. Rev. Lett.* **31**, 1061 (1973).

[163] M. G. Pini *et al.*, "Surface spin–flop transition in a uniaxial antiferromagnetic Fe/Cr superlattice induced by a magnetic field of arbitrary direction," *J. Phys.: Condens. Matter* **19**, 136001 (2007).

[164] A. I. Morosov and A. S. Sigov, "Surface spin-flop transition in an antiferromagnet," *Phys. Usp.* **53**, 677 (2010).

[165] R. W. Wang *et al.*, "Surface spin-flop transition in Fe/Cr(211) superlattices: Experiment and theory," *Phys. Rev. Lett.* **72**, 920 (1994).

[166] B. Böhm *et al.*, "Antiferromagnetic domain wall control via surface spin flop in fully tunable synthetic antiferromagnets with perpendicular magnetic anisotropy," *Phys. Rev. B* **100**, 140411 (2019).

[167] J.-Q. Yan *et al.*, "A-type antiferromagnetic order in MnBi4Te7 and MnBi6Te10 single crystals," *Phys. Rev. Materials* **4** (2020).

Appendix A

Surface Spin-Flop Simulation

The numerical simulations were performed with the revised Mills model,

$$\begin{aligned} E = \sum_{i=1}^{N-1} J_i \mathbf{s}_i \cdot \mathbf{s}_{i+1} \quad &+ \quad \mathbf{H} \cdot \sum_{i=1}^{N} \mathbf{s}_i + \sum_{i=1}^{N} \tfrac{K_i}{2} (\mathbf{s}_i \cdot \hat{\mathbf{z}})^2, \\ \mathbf{s}_i \quad &\rightarrow \quad \mathbf{s}_i + \delta_{i=1,N}(\lambda_s - 1)\mathbf{s}_i, \\ J_i \quad &= \quad J + \delta_{i=1,N-1}(\lambda_J - 1)J, \\ K_i \quad &= \quad K + \delta_{i=1,N}(\lambda_K - 1)K, \end{aligned}$$

where $\lambda_A, (A = s, J, K)$ represents the reduction of surface magnetization, exchange coupling, and anisotropy energy, respectively. The reduced surface magnetization causes a pinning of the spin-flop state at the surface. One end of the system described by a "clamped boundary condition" in which the spin constrained to that of the bulk,

$$\theta_{i=N} = \theta_{\text{Bulk}} = \begin{cases} 0, \wedge H_{\text{FM}} < H \\ \pm \cos^{-1} \frac{H}{H_{\text{FM}}}, \wedge H_{\text{BSF}} < H \leq H_{\text{FM}} \\ (\pm 1 - 1)\, \frac{\pi}{2}, \wedge H \leq H_{\text{BSF}} \end{cases},$$

where $H_{\text{FM}} = 4J - K$ and $H_{\text{BSF}} = \sqrt{K\,(4J - K)}$ are threshold fields for the bulk forced ferromagnetic and bulk spin-flop transitions respectively, the anisotropy $K < 2J$ is assumed to be small, and the sign indicates two types of surfaces: + for parallel and – for antiparallel.

The phase diagram of a semi-infinite system is obtained by using of revised Mills model with the one-side-clamped boundary condition for $N = 16$ layers with a parameter set of ($\frac{K}{J} = 0.4, \lambda_s = 0.6,\ \lambda_J = 0.8$, and $\lambda_K = 0.6$). The ground state at each sampling point is searched by comparing total energies of spin configurations relaxed from 200 initial random

configurations. Two SSF states in the phase diagram are illustrated by comparing the net spin canting of two surfaces, which is defined as $C_{A,P} \equiv \frac{1}{N}\sum_{i=1}^{N} \sin^2\left(\theta_i^{A,P}\right)$ for antiparallel (A) and parallel (P) surfaces. The difference $C_A - C_P$ vanishes if both surfaces are in the bulk spin-flop (BSF) state or collinear states, and remains finite only when one surface is in the SSF state.

A.1 Simulation of MFM Contrast

In order to compare the simulation result of spin structure with experiment, the spatial gradient of magnetic force acting on the MFM tip is calculated with the simulated spin configurations with respect to the applied field for a given set of parameters. For simplicity, we approximate the magnetization of septuple layers with series of point magnetic dipole moments which are vertically aligned below the tip. Thus, the force gradient is calculated as $\partial F = \sum_{i=1}^{1000} \frac{cos(\theta_i)}{(d+t(i-1))^5}$, where $d = 150$ nm is the tip-surface distance, $t = 13.6$ Å is the thickness of one septuple layer, and θ_i is a zenith angle of the i-th layer. For $i \geq N$, the angles are constrained or assumed to be that of bulk. The point dipoles approximation of septuple layers provides a qualitative description of the magnetic field dependence of MFM signal of domain contrast, though the oversimplified assumption prevents a quantitative account.

A.2 Pinning of Spin-flop State via Surface Magnetization Reduction

In the original Mills' model, the spin-flop state first nucleates on the antiparallel surface and migrates into the bulk with increasing external field as reproduced in Fig. A.1 (a) and (b). Figure A.1(a) shows the canting position $\langle d \rangle$ with respect to the external field, which is calculated as,

$$\langle d \rangle = \frac{1}{N} \frac{\sum_{i=1}^{N} \mathrm{i}\ \sin^2(\theta_i)}{\sum_{i=1}^{N} \sin^2(\theta_i)}.$$

The migration occurs as a consequence of first order transitions that are clearly seen in the stepwise increase of the canting position. Two surfaces eventually become indistinguishable (at B_6) due to the migration. In the revised Mills' model, however, the flop state is found to be pinned on the surface if the surface magnetization is reduced more than 10% ($\lambda_s < 0.9$). Instead of the stepwise change, the flop state smoothly expands from the surface as shown in Fig. A.1(c). The more the surface magnetization is reduced, the more the flop state is localized on surface. An intermediate step appears for $\lambda_s = 0.4$ due to the spin-flop transition of the parallel surface as shown in Fig. A.1(d).

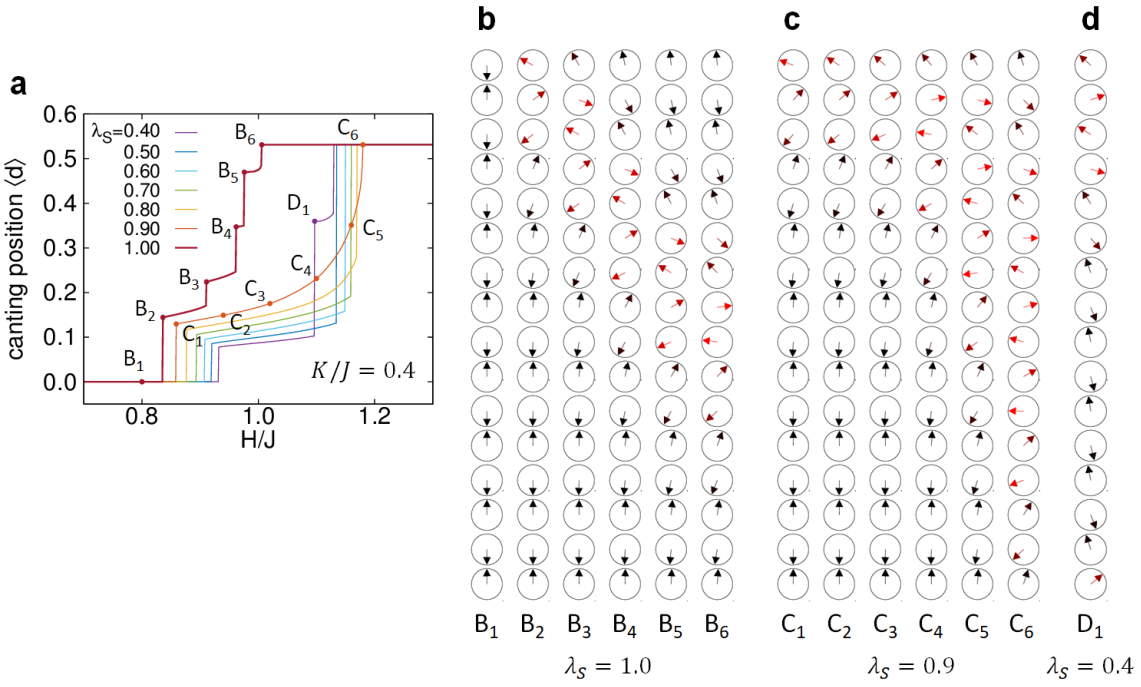

Figure A.1: (a) Normalized depth of spin-flop state with respect to external field. Color of lines indicates surface magnetization. (b-d) Spin configurations of original and revised Mills' model ($\lambda_S = 1.0,\ 0.9,\ 0.4$) at each point in (a). Color of arrows represents the amount of canting from layer normal.

A.3 Universality of MFM Contrast Reversal

The reduction of surface magnetization induces SSF on the parallel surface as seen in Fig. A.1(d). In order to understand the individual effect of surface parameters (λ_s, λ_J, λ_K) on the SSF transition, the parameter space is swept at $K/J = 0.4$. Figure A.2(a) shows the parameter window where the relative threshold field, $r_{A,P} \equiv (H_{\mathrm{BSF}} - H_{\mathrm{SSF}}^{A,P})/H_{\mathrm{BSF}}$ exhibits the values found in experiment ($r_A \approx 0.5$, $r_P \approx 0.1$) with 10% (dark shadow) and 20% (pale shadow) errors. The colored solid lines are contour plots satisfying $r_A = 0.5$ (blue) and $r_P = 0.1$ (red) as shown in Fig. A.2(b). It clearly shows that SSF transition occurs on both surfaces in a broad parameter window and the MFM contrast is reproduced in good agreement with experiment (Fig. A.2(c)).

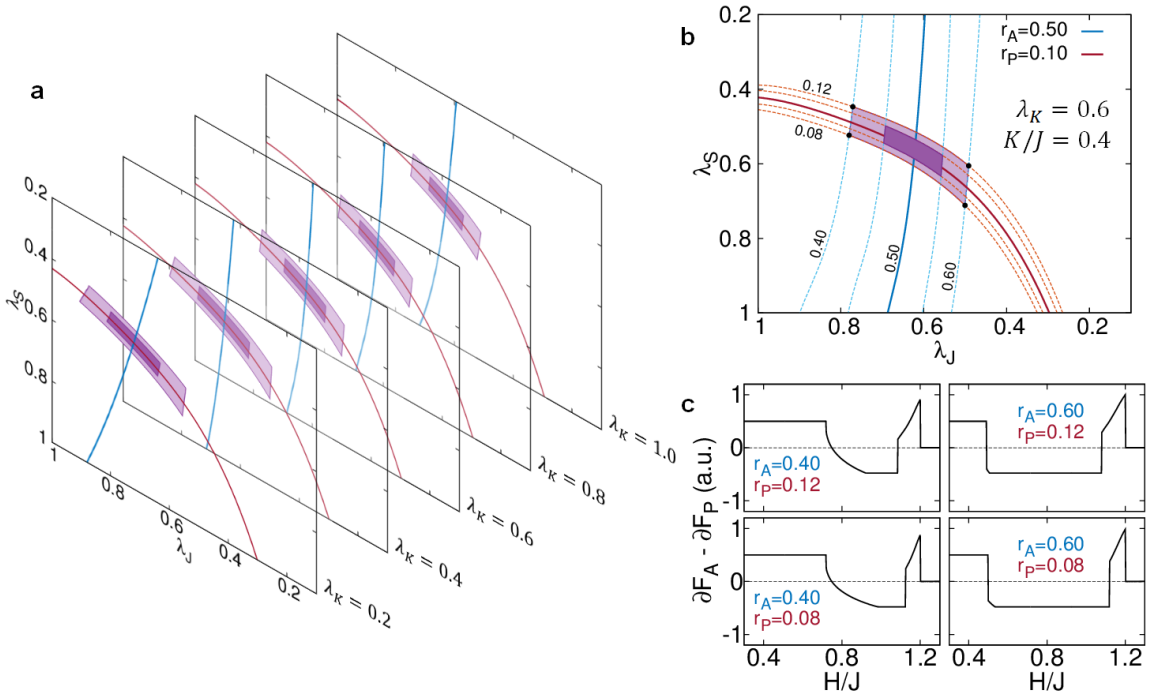

Figure A.2: (a) Contour lines satisfying $r_A = 0.5$ (blue) and $r_P = 0.1$ (red) in the parameter space of (λ_J, λ_s). (b) Contour lines for a specific case of $\lambda_K = 0.6$. Dark and pale colored area indicates 20% and 10% window from the crossing points, respectively. (c) Simulated MFM contrast at the corners of 20% window in (b), which qualitatively agree with the experimental results in Fig. 5.3(w) of main text.